Femtosecond Mid-Infrared Spectroscopy of Elementary Photoinduced Reactions

D I S S E R T A T I O N

zur Erlangung des akademischen Grades
doctor rerum naturalium
(dr. rer. nat.)
im Fach Physik

eingereicht an der
Mathematisch-Naturwissenschaftlichen Fakultät I
Humboldt-Universität zu Berlin

von
Herr Dipl.-Ing. Matteo Rini

Präsident der Humboldt-Universität zu Berlin:
Prof. Dr. J. Mlynek

Dekan der Mathematisch-Naturwissenschaftlichen Fakultät I:
Prof. Dr. M. Linscheid

Gutachter:

1. Prof. Dr. Thomas Elsaesser
2. Prof. Dr. Nikolaus Schwentner
3. Prof. Dr. Jürgen P. Rabe

eingereicht am:	17. Juli 2003
Tag der mündlichen Prüfung:	12. Dezember 2003

Hiermit erkläre ich, die Dissertation selbstständig und ohne unerlaubte Hilfe angefertigt zu haben.
Ich habe mich anderwärts nicht um einen Doktorgrad beworben und besitze einen entsprechenden Doktorgrad nicht.
Ich erkläre die Kenntnisnahme der dem Verfahren zugrunde liegenden Promotionsordnung der Mathematisch-Naturwissenschaftlichen Fakultät I der Humboldt-Universität zu Berlin.

Berlin, den 15. Juli 2003 Matteo Rini

Veröffentlichungen im Zusammenhang mit dieser Arbeit
Publications in conjunction with this thesis

[1] M. Rini, B. Z. Magnes, E. Pines, and E. T. J. Nibbering, "Real-time observation of bimodal proton transfer in acid-base pairs in water," Science (2003), in press.

[2] A. K. Holm, M. Rini, E. T. J. Nibbering, and H. Fidder, "Femtosecond UV/mid-IR study of photochromism of the spiropyran 1',3'-dihydro-1',3',3'-trimethyl-6-nitrospiro[2H-1-benzopyran-2,2'-(2H)-indole] in solution," Chem. Phys. Lett. **376,** 214–219 (2003).

[3] M. Rini, J. Dreyer, E. T. J. Nibbering, and T. Elsaesser, "Ultrafast vibrational relaxation processes induced by intramolecular excited state hydrogen transfer," Chem. Phys. Lett. **374,** 13–19 (2003).

[4] M. Rini, A. K. Holm, E. T. J. Nibbering, and H. Fidder, "Ultrafast UV-mid-IR investigation of the ring opening reaction of a photochromic spiropyran," J. Am. Chem. Soc. **125,** 3028–3034 (2003).

[5] M. Rini, A. Kummrow, J. Dreyer, E. T. J. Nibbering, and T. Elsaesser, "Ultrafast site-specific mid-infrared spectroscopy of excited-state intramolecular proton transfer," In *Ultrafast Phenomena XIII*, R. D. Miller, M. M. Murnane, N. F. Scherer, and A. M. Weiner, eds., Springer Ser. Chem. Phys. **71,** 465–467 (Springer, Berlin, 2003).

[6] M. Rini, A. Kummrow, J. Dreyer, E. T. J. Nibbering, and T. Elsaesser, "Femtosecond mid-infrared spectroscopy of condensed phase hydrogen-bonded systems as a probe of structural dynamics," Faraday Discuss. **122,** 27–40 (2002).

Andere Veröffentlichungen/*Other publications:*

[1] R. Grunwald, V. Kebbel, U. Griebner, U. Neumann, A. Kummrow, M. Rini, E. T. J. Nibbering, M. Piché, G. Rousseau, and M. Fortin, "Generation and characterization of spatially and temporally localized few-cycle optical wave packets," Phys. Rev. A **67,** 063820 (2003).

[2] R. Grunwald *et al.*, "Generation of ultrashort-pulse nondiffracting beams and X-waves with thin-film axicons," In *Ultrafast Phenomena XIII*, R. D. Miller, M. M. Murnane, N. F. Scherer, and A. M. Weiner, eds., Springer Ser. Chem. Phys. **71,** 247–249 (Springer, Berlin, 2003).

[3] R. Grunwald *et al.*, "Femtosecond laser beam shaping with structured thin-film elements," In *Applications of Photonic Tchnology 5*, R. A. Lessard, G. A. Lampropoulos, and G. W. Schinn, eds., Proceedings of SPIE **4833,** 354–361 (2002).

[4] V. Kozic, W.Wernke, J. Dreyer, K. W. Brzezinka, M. Rini, A. Kummrow, and T. Elsaesser, "Vibrational excitation and energy redistribution after ultrafast internal conversion in 4-nitroaniline," J. Chem. Phys. **117,** 719–726 (2002).

[5] M. Krikunova, A. Kummrow, B. Voigt, M. Rini, H. Lokstein, A. Moskalenko, H. Scheer, A. Razjivin, and D. Leupold, "Fluorescence of native and carotenoid-depleted LH2 from *Chromatium minutissimum*, originating from simultaneous two-photon absorption in the spectral range of the presumed (optically dark) S_1 state of carotenoids," FEBS Lett. **528,** 227–229 (2002).

[6] R. Grunwald, U. Griebner, E. T. J. Nibbering, A. Kummrow, M. Rini, T. Elsaesser, V. Kebbel, H. J. Hartmann, and W. Jüptner, "Spatially resolved small-angle noncollinear interferometric autocorrelation of ultrashort pulses with microaxicon arrays," J. Opt. Soc. Am. A **18,** 2923–2931 (2001).

Contents

Chapter 1

Introduction

The invention of flash photolysis, the advent of pulsed laser technology, the transition into the femtosecond time domain, the major recent developments of laser technology in terms of available tunability, stability, energy, pulse duration have made it possible to study chemical reactions with continuously improving time resolution, following the reaction dynamics in real time, and to perform detailed studies of fundamental physical and chemical processes such as energy and charge transfer, dephasing and relaxation phenomena [1,2]. When dealing with ultrafast chemical reaction dynamics in the condensed phase, the object of research is not only to decipher the underlying molecular parameters determining femtosecond chemical events of bond breaking and formation (a subject known as *femtochemistry* [3,4]), but also to analyze the role that nearby solvent molecules have on the chemical reaction dynamics. Solvent motions occur with a broad range of time scales, with ultrafast components at femtosecond and picosecond time scales having a major influence on the outcome of these reactions due to processes such as molecular conformation (de-)stabilization, electronic and vibrational energy exchange, electronic and vibrational coherence decay and cage effect in molecular dissociation [2].

The ideal method for - time-resolved - studies of chemical reaction dynamics would be a technique where the spatial parameters of the structural dynamics are resolved for the molecular probe under study as well as for the nearby solvent molecules. In the future, femtosecond x-ray spectroscopy [5–12] may eventually permit to combine both atomic spatial resolution and adequate time resolution to directly observe the evolution of atomic configurations in time, i.e., to obtain a dynamic structural picture of matter. Clearly, the application of ultrashort x-ray pulses is still at a development stage at the present time and one has to rely on different approaches.

Electronic spectroscopy is the most commonly used method for investigations in the condensed phase, whereby transmission or emission changes of reactants, intermediates and reaction products are monitored. However, these techniques typically probe electronic transitions occurring between delocalized orbitals and

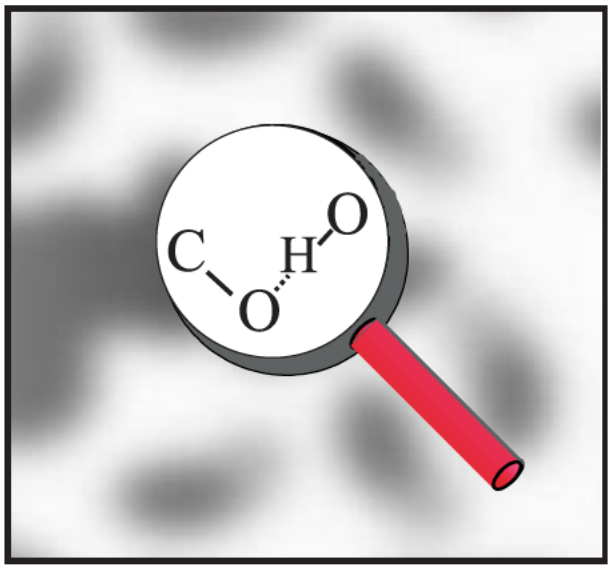

Figure 1.1: Infrared spectroscopy has the potential of revealing site-specific information if local vibrational modes are probed.

- thus - site-specific information about structural changes of the solute or local intermolecular interactions between the solute and its surroundings are difficult to obtain. Besides, the fast dephasing times of electronic transitions in solutions result in broad absorption lines. Absorption bands of different species may significantly overlap, complicating the interpretation of the experimental results, especially when the complexity of the reaction increases, due e.g. to the presence of different isomers or to the involvement of numerous electronic states.

Decades of stationary vibrational spectroscopy have shown that often vibrational transitions are much more localized and thus provide microscopic information about specific functional groups, both in the solute and in the environment. Femtosecond infrared spectroscopy can be used as an alternative to probe ultrafast structural dynamics. It is well known that with time-resolved vibrational spectroscopy one can grasp the dynamics of specific chemical bonds in the case the probed vibrations can be regarded as local modes (Fig. 1). In contrast, by probing electronic states with optical frequencies additional arguments are necessary to determine whether certain chemical bonds are involved in the reaction pathways. Furthermore, vibrational dephasing times are typically relatively long, resulting in very narrow vibrational IR absorption lines. With some important exceptions (e. g. the OH stretching band in presence of hydrogen bonding, which can exhibit line widths on the order of a few hundred wavenumbers), vibrational line widths are rarely larger than 50 cm^{-1} and values in the range 5-20 cm^{-1} are common. This increases the chances of finding spectral regions where different lines do not overlap. Several major advantages, enabling to derive detailed struc-

tural information on molecular geometries and interactions, are well-known:

(i) Site-specific information from inspection of vibrational bands.
In the case that a molecular vibration is coupled to the reaction coordinate, leading to marked frequency shifts and intensity changes, this mode can be used as a spectator for the state of the chemically reactive bond. An important example is given by O-H stretching and O-H bending modes and C=O stretching modes of hydrogen-donor and -acceptor molecules capable of hydrogen bonding [13]. The fact that these modes change their characteristics upon hydrogen bonding make it possible to regard them as *spectators* of the hydrogen bond. For instance, the potential of probing site-specific hydrogen bond cleavage and rearrangements has been demonstrated in the case of hydrogen-bonded complexes of coumarin 102, a standard probe in solvation dynamics studies [14–19].

(ii) Geometric information from vibrational band patterns.
Vibrational marker modes can appear, shift or disappear, indicating the occurrence of a rearrangement of nuclear coordinates when crossing occurs from the reactant state towards the product state. The combined approach of ultrafast infrared spectroscopy and high-level ab initio quantum chemical calculations allows to gain new insight into microscopic reaction mechanisms. This has been for instance demonstrated in the studies of the photoinduced intramolecular charge transfer (ICT) in 4-(dimethylamino)-benzonitrile (DMABN), providing the determination of geometric structures of transient states [20–26].

(iii) Structural information from anharmonic coupling between vibrational modes.
Direct geometric information can be obtained from mid-IR pump/mid-IR probe experiments on vibrational bands that exhibit features of anharmonic coupling between vibrational modes. By inspection of one specific mode not only the dynamics of this mode can be followed, but also the dynamics of a second mode are monitored due to anharmonic coupling between these modes. In principle, due to the implicit geometrical dependencies of the anharmonic couplings between vibrational normal modes the potential of the method lies in resolving information on the molecular structure. In addition, due to the inherent time-resolution structural dynamics of evolving molecular species can be grasped. An illustration of the potential of IR spectroscopy of probing anharmonic coupling is represented by results obtained on intramolecular hydrogen bonds of organic molecules in the electronic ground state. A modulation of the IR pump-probe signal in phthalic acid monomethylester (PMME) with a period of 330 fs has been observed, indicating a coherent motion of the hydrogen bond [27]. The coherent motions have been ascribed to anharmonic coupling between the O-D stretching mode and a low-frequency out-of-plane motion of the two sub-groups that are connected to each other through the hydrogen bond. Similar features have been

obtained for 2-(2'-hydroxyphenyl)benzothiazole (HBT), where the hydrogen bond distance is modulated by a 120 cm^{-1} in-plane deformation mode [28]. In hydrogen bonded dimers it has been demonstrated that impulsive excitation of the O-D stretching mode induces via the anharmonic coupling coherent motions along several intermolecular low-frequency modes [29]. Important information for the understanding of such hydrogen-bonded structures, representing a key structural feature of biomolecules, has been thus derived from the underlying microscopic elongations, the vibrational frequencies and the anharmonic coupling. Determination of molecular structure is also pursued by investigation of excitonic coupling between vibrational modes with comparable transition frequencies by use of two-dimensional IR spectroscopy [30]. Examples on which structural information has been obtained include small peptides [31–34], N-methylacetamide [35] and $Rh(CO)_2(C_5H_7O_2)$ [36]. Two-dimensional IR spectroscopy can in principle be extended towards resolution of transient structures by means of an additional optical trigger pulse.

In this work, time resolved vibrational spectroscopy has been applied to address from a new experimental perspective some of the most thoroughly studied photoinduced reactions: the excited state hydrogen/proton transfer, both in an *intramolecular* and in an *intermolecular* case, and the isomerization of photochromic compounds have been investigated in important molecular systems.

Chapter 2 describes some details of the experimental approach followed in this thesis: time-resolved, ultraviolet pump/mid-infrared probe spectroscopy with frequency resolved detection. In this technique a photoinduced reaction is initiated by femtosecond UV pump pulses, and the molecular dynamics are followed by probing the induced changes of transmission of a sample with femtosecond mid-IR pulses. This chapter briefly discusses three aspects which have been of relevance in the interpretation of the experimental data: (i) Perturbed free-induction decay (PFID) is a coherence effect which is observable because the accessible time resolution is significantly shorter than the dephasing times of the vibrational transitions involved. It must be fully understood in order to be able to separate PFID effects from *real* kinetic components caused, e.g, by an ultrafast chemical reaction or an energy relaxation process. (ii) Including the effects of anharmonicity is essential in order to understand the IR spectrum of a vibrationally excited molecule. The formalism of anharmonicity is briefly reviewed. It has been useful in order to discuss the selective flow of energy into a given vibrational mode after a photoinduced reaction and to explain the shifting of a vibrational line in terms of the anharmonic coupling to highly populated vibrations. (iii) Rotational relaxation affects ultraviolet pump/mid-infrared probe measurements employing polarized light. Whenever the molecular dynamics are characterized by comparable time scales, it is important to be able to separate experimentally the true dynamics from the contributions to the signals due to rotational relaxation.

Chapter 3 gives a brief description of the experimental setup for ultraviolet

pump/mid-infrared probe measurements as well as of the schemes for the generation of femtosecond, microjoule pulses in the UV and in the mid-IR, at 1 KHz repetition rate.

The molecular structure of many important systems (e. g. protic solvents like water, biomolecular polymers such as proteins and DNA) are largely determined by the special properties of hydrogen bonds. In such systems, the molecular function often involves the transfer of hydrogen atoms or protons, typically along pre-existing hydrogen bonds. The study of proton/hydrogen transfer processes occurring after photoexcitation to a higher electronic state is the subject of Chapters 4 and 5.

Chapter 4 is dedicated to the excited-state *intramolecular* hydrogen transfer (ESIHT) reaction, an interesting model for studying basic microscopic reaction mechanisms. The ESIHT reaction was studied in an important model system, 2-(2'-hydroxyphenyl) benzothiazole (HBT), where the hydrogen transfer reaction takes the typical form of an enol-keto tautomerization reaction:

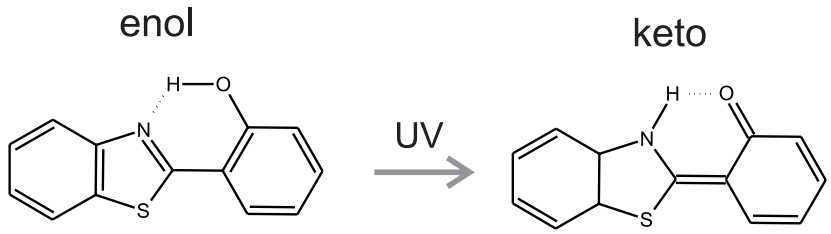

Figure 1.2: Excited state *intramolecular* hydrogen transfer (ESIHT) in HBT.

The dynamics of the formation of the keto species were directly observed by probing the delayed appearance of the C=O carbonyl stretching mode formed by hydrogen transfer. A detailed study of the carbonyl band and of other vibrations in the fingerprint region (1000 to 1700 cm^{-1}) shows that such vibrational modes, and in particular the C=O stretch, do not serve as channels accepting the excess energy released in the ESHIT reaction, which is initially mainly stored in several low frequency Raman active modes. The analysis of the measured vibrational bands has allowed to elucidate the process of energy redistribution following the reaction. Effects of coherence were also evident in the oscillatory features of the C=O band, reflecting coherent wavepacket motions along low frequency, anharmonically-coupled modes.

The work reported in Chapter 5 deals with the paradigm reaction of solution chemistry: the acid-base neutralization reaction, which involves an *intermolecular* proton transfer. Photoacids are molecular systems that exhibit a dramatic

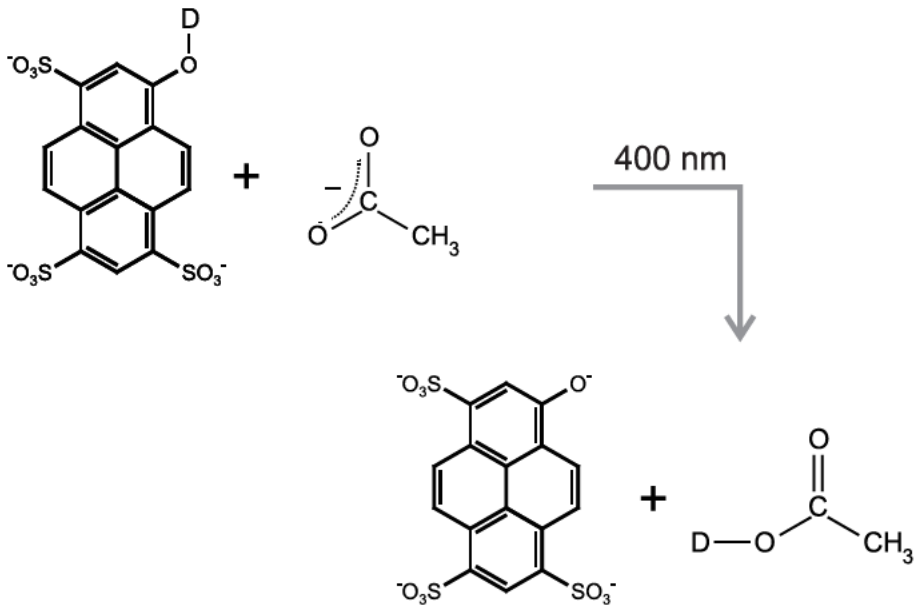

Figure 1.3: Acid-base neutralization reaction: excited state *intermolecular* proton transfer from HPTS to acetate.

increase of the acidity constant after photoexcitation and can be used as molecular triggers of acid-base reactions. Here, the proton transfer from the photoacid 8-hydroxypyrene-1,3,6-dimethylsulfamide (HPTS) (see Fig. 1.3) to the solvent or to a base in solution is initiated by photoexcitation of the HPTS molecule and followed through inspection of specific IR-active vibrational marker modes of the Brønsted acid or its conjugate anion, and of the protonated base that is generated in the reaction. The measurements are done with a fixed amount of the acid in water and varying the concentration of the base, in order to separate the effects of diffusion on the bimolecular reaction. The data reveal very clearly two aspects. First, the kinetics shows a very fast component, which is ascribed to pre-existing hydrogen-bonded photoacid-base pairs. The proton transfer for such complexes proceeds at an ultrafast pace, within the experimental resolution of 150 fs. It was thus possible to study bimolecular reactions under ambient conditions where the reactants (or a significant fraction of them) do not have to diffusionally encounter and to observe an unexpectedly ultrafast (non diffusion-limited) proton transfer. Second, in encounter pairs formed by diffusion of uncomplexed photoacid and base molecules, the reaction appears to be diffusion-limited and can by analyzed by extended rate equations which include diffusive processes. At low concentrations, the proton appears to be first transferred to the solvent and then shuttled to the base.

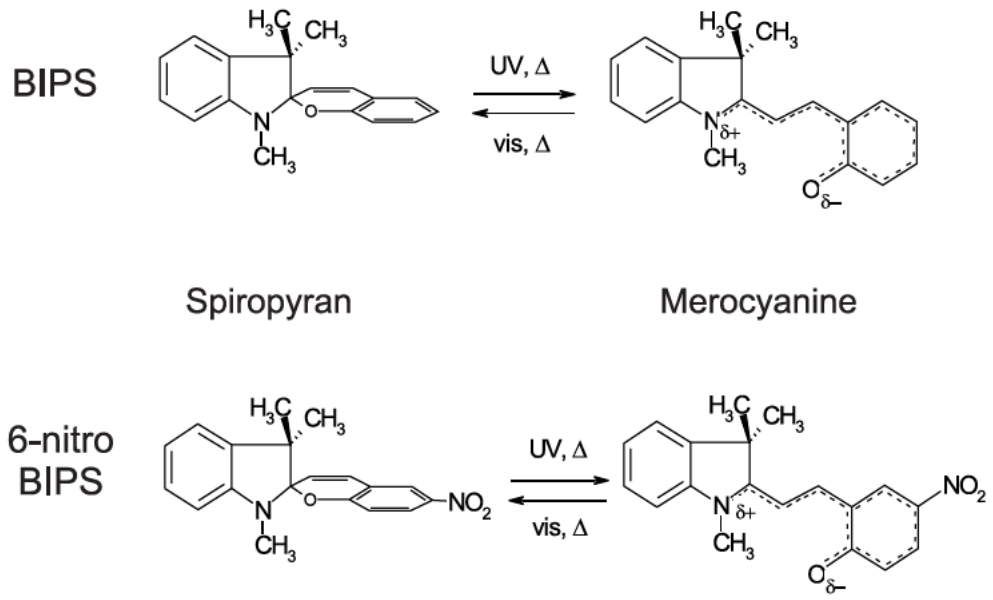

Figure 1.4: Photochromic ring-opening reaction of BIPS (top) and 6-nitro-BIPS (bottom).

In Chapter 6 photochromic compounds are studied. Photochromism is defined as the reversible photo-induced transformation of a chemical species between two states having distinguishable absorption spectra and is of potential interest for a variety of applications, including optical data storage, displays and optically controlled molecular switching. The investigation of one of the most studied photochromic reactions is reported: the spiropyran-merocyanine chemical ring opening/closure reaction of two spiropyrans (see Fig. 1.4), 1',3',3',- trimethyl-spiro -[-2H-1- benzopyran -2,2'- indoline] (commonly referred to as BIPS), and a derivative of BIPS, 1',3'- Dihydro -1',3',3'- trimethyl -6- nitrospiro [2H-1- benzopyran -2,2'-(2H)- indole] (6-nitro-BIPS). By monitoring the mid-IR spectra of the reacting species, the relevant time scales for the formation of the reaction products have been determined and the existence of different merocyanine isomers has been discussed. A specially important result of these investigations is the observation that the main decay channel for the spiropyran S_1 excited state is internal conversion to the spiropyran S_0 ground state, with a quantum yield of 90% or more in the case of BIPS. Previous studies never mentioned this a rather influential decay channel, which may well be the key factor in determining the overall photochemistry quantum yield for this class of molecules. Thinking in terms of potential applications to actual devices, usable photochromic systems should of course be characterized in the first instance by a high reaction yield.

Chapter 2

Ultrafast vibrational spectroscopy of photoinduced reactions

2.1 Introduction

The work described in this thesis is based essentially on time-resolved ultraviolet pump/mid-infrared probe experiments, where a photoinduced reaction is initiated by femtosecond UV pump pulses, and the dynamics of the system are followed by probing the induced changes of transmission of a sample with femtosecond mid-IR pulses. This chapter gives a brief theoretical introduction to this experimental technique and introduces the most relevant effects that have to be taken into account in order to interpret the experimental features: the perturbed free induction decay (a coherence effect), the effects of anharmonicity on the vibrational spectra, the effects of rotational relaxation on measurements with polarized light.

The technology of femtosecond IR spectroscopy has progressed to the point where the accessible time resolution is significantly shorter than the dephasing times of the vibrational transitions involved. Under these experimental conditions, the coherence of the interaction between the electric field of the probing pulse and the vibrational transition has to be taken into account. This situation leads to *coherence* phenomena, which must be fully understood in order to be able to separate those effects from kinetic components caused, e.g., by an ultrafast chemical reaction or an energy relaxation process. Section 2.3 deals with the perturbed free induction decay effect, a consequence of coherence and dephasing: in a pump/probe experiment, it manifests itself through changes of absorbance measured at negative delay times (i.e. pump coming after the probe), whereas changes of absorbance due to real kinetic components are expected only at positive delay times.

The simplest description of the vibrational spectrum of molecules follows from the harmonic approximation, where any motion of the system can be represented

as a superposition of normal modes and each mode can be described as an harmonic oscillator. Introducing corrections due to anharmonicity is essential to understand the IR spectrum of a vibrationally excited molecule. Section 2.4 briefly reviews the formalism of anharmonicity and its effects on the vibrational spectrum of a molecule. In a realistic situation, the energy spectrum of a vibrational mode does not consist in an equispaced ladder (if the potential energy consisted of only quadratic terms, it would require infinite energy to break a valence bond). A deeper description considers also corrections to the normal mode picture, introducing the anharmonic coupling between distinct vibrational modes. The concept of anharmonicity has been useful in this work to discuss the selective flow of energy into a given vibrational mode after a photoinduced reaction and to explain the observed shifting of a vibrational line in terms of the anharmonic coupling to highly populated, anharmonically coupled vibrations (see Chapter 4 and 6).

The use of linearly polarized light makes the ultraviolet pump/mid-infrared probe experiments sensitive to rotational relaxation effects: the photoselection process by UV excitation defines an initial preferential geometry which then evolves with time towards an isotropic distribution. Section 2.5 discusses how to separate, in the measured transients, the molecular dynamics from the contributions to the signals due to effects of rotational relaxation.

The material described in this chapter is based to a large extent on references [37–42].

2.2 UV-pump IR-probe spectroscopy with frequency selective detection

Ultrafast vibrational spectroscopy of photoinduced reactions is based on the same time resolving methods as the more conventional studies where electronic transitions are used to probe the molecular dynamics. In particular, pump-probe techniques have widely been applied. Here, an intense UV pump pulse triggers a photochemical reaction by exciting the molecule to a higher electronic state. The resulting changes of absorption in the infrared are probed by monitoring the transmission of the sample with weak infrared pulses as a function of the delay time between pump and probe. The most common pump-probe methods are: conventional pump-probe, pump-probe with frequency selective detection and gated IR detection [37]. In gated IR detection the sample, excited by a pulsed field, is probed by a CW IR field, which acquires a time dependence due to the sample response. Time resolution is then achieved by using a gate pulse which up-converts the frequency of the probing pulse in a nonlinear crystal. In conventional pump-probe the sample, pumped by a short UV pulse, is probed by a short IR pulse. The IR pulse generates an IR signal field that interferes

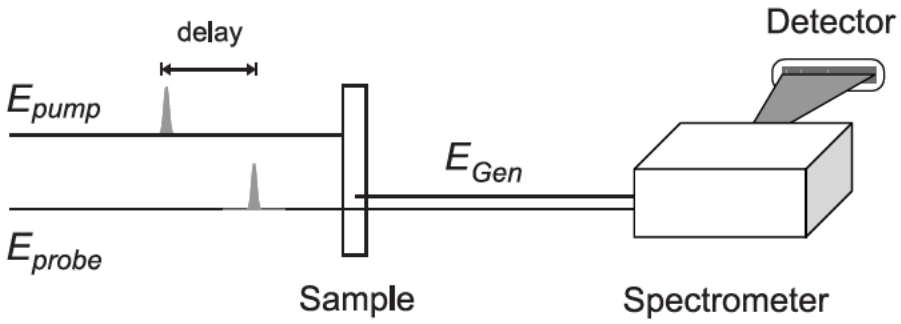

Figure 2.1: Ultraviolet pump/mid-infrared probe spectroscopy with frequency selective detection. The square law, time-integrating detector is an array of 32 elements, which record simultaneously the complete pulse spectrum.

with the original probe-pulse on a time integrating detector measuring intensity, i.e. squared electric fields. All the pump-probe experiments described in this thesis have been performed with frequency selective detection: the probe and generated field pass through a monochromator before impinging on the detector, as illustrated in Fig. 2.1. The square law detector is an array of 32 elements, which record simultaneously the complete pulse spectrum. Spectral detection is necessary because the bandwidth of the short femtosecond pulses is much larger than the typical line widths of vibrational transitions.

The theory of ultraviolet pump/mid-infrared probe spectroscopy is a special case of the theory of light-matter interaction. In the dipole approximation, the interaction Hamiltonian is given by: $H_1 = -\hat{\mu} \cdot \mathbf{E}$ where $\hat{\mu} = -e\mathbf{r}$. The dipole moment averaged over the electronic coordinates in the i-th electronic state is

$$\mu_i(\mathbf{q}) = \mu_{\mathrm{i}}(0) + \left(\frac{\partial \mu_i}{\partial \mathbf{q}}\right)_0 \cdot \mathbf{q} + \ldots \tag{2.1}$$

Transitions in the IR have dipole moments μ_{mn} given by:

$$\mu_{mn} = \langle m|\mu_i(\mathbf{q})|n\rangle \cong \left(\frac{\partial \mu_i}{\partial \mathbf{q}}\right) \langle m|\mathbf{q}|n\rangle \tag{2.2}$$

which determines the selection rules for vibrational transitions.

Pump-probe spectroscopy is a third-order nonlinear technique, where a third order polarization $P^{(3)}(t)$ is generated in the sample by two interactions with the

pump and one interaction with the probe field. The polarization acts as a source term in the Maxwell equations which can be solved in the slowly varying envelope approximation and the small signal limit [43]. In this approximation the wave equation connecting polarization and electric field is given by:

$$\frac{\partial E(t)}{\partial z} = \frac{i\omega_{pr}}{\varepsilon_0 c} P(t) \tag{2.3}$$

which in the small signal limit gives the solution:

$$E_{pr,Tot}(t) = E_{pr}(t) + E_{Gen}(t), \quad E_{Gen}(t) = \frac{i\omega_{pr} L}{\varepsilon_0 c} P(t) \tag{2.4}$$

where L is the optical path length of the sample. Hence, the polarization P of the sample generates a new pulsed field, $E_{Gen}(t)$, which interferes with the original probing field $E_{pr}(t)$ on the detector. Transient gain or absorption correspond to a generated field which is in-phase or out-of-phase with the probe field. In general, the detector will be slow compared to the duration of the femtosecond pulses. Thus, the total signal detected is proportional to the time integral of the light intensity, resulting in:

$$\int_{-\infty}^{+\infty} \mathrm{d}t \, |E_{pr,Tot}(t)|^2 = \int_{-\infty}^{+\infty} \mathrm{d}t \left[|E_{pr}(t)|^2 + |E_{Gen}(t)|^2 + 2\mathrm{Re} E_{pr}(t) E_{Gen}(t) \right] \tag{2.5}$$

where the first term is constant and can be subtracted off in an experiment through proper normalization, the second term will be negligibly small (in the small signal limit) and the third term contains the relevant information on the nonlinear polarization generated in the sample.

In the case of spectrally resolved detection, the measured signal (spectrally resolved relative transmission change $\Delta T(\omega)/T_0(\omega) = (T(\omega) - T_0(\omega))/T_0(\omega)$ is then given by [44]:

$$\frac{\Delta T(\omega)}{T_0(\omega)} \propto \omega \mathrm{Im} \left[\frac{P^{(3)}(\omega)}{E^*_{pr}(\omega)} \right] \tag{2.6}$$

where $T(\omega)$ and $T_0(\omega)$ are the transmission of the sample with and without excitation and $E_{pr}(\omega)$ is the Fourier transform of the time dependent probe field. It follows from this expression that not only population changes contribute to the pump-probe signals, but also coherent polarizations. The impulsive excitation process creates coherent, non-stationary superpositions of states (wavepackets) in the system. Only after the decay of coherence is completed, a description in terms of population dynamics is appropriate. Coherence is destroyed by dephasing processes which in the condensed phase occur on time scales of tens of femtoseconds for vibronic transitions and in the femto- to picosecond time domain for vibrational excitations.

In the density matrix formalism, the polarization is given by the expectation value of the dipole moment μ:

$$P(t) = \mathrm{Tr}[\mu\rho(t)] \equiv \langle\mu\rho(t)\rangle \tag{2.7}$$

where $\langle\ldots\rangle$ denotes averaging over the ensemble described by the density matrix. For a given level system, it is usually calculated using perturbation theory. Diagrammatic methods, especially double-sided Feynman diagrams, have been used [44] to keep track of the various terms of perturbation theory, exploiting methods that simplify the calculation, such as time ordering, rotating wave approximation (to neglect nonresonant contributions), phase-matching (the geometry of the experimental setup allows to reduce the number of terms in the nonlinear response function). A detailed theory describing ultraviolet pump/mid-infrared probe experiments for several examples (destruction of a molecule by a UV laser pulse, transients in a system with two electronic states, transients in a system with three electronic states undergoing a reaction ...) can be found in Ref. [37].

2.3 Effects of coherence: the perturbed free-induction decay

Laser technology makes it now possible to generate stable femtosecond pulses shorter than 100 fs, tunable in a wide infrared spectral range covering the region between 1000 cm^{-1} and 10000 cm^{-1}. Several femtosecond UV pump/mid-IR probe experiments have given new insights into ultrafast structural changes of molecules during photochemical reactions. The technology of femtosecond IR spectroscopy has progressed to the point where the accessible time resolution is significantly shorter than the typical dephasing times of vibrational transitions. Under these experimental conditions, the coherence of the interaction between the probing pulse and vibrational transitions has to be taken into account. This situation leads to new phenomena, not normally encountered in condensed phase pump-probe spectroscopy with visible light pulses [45].

The interaction of the visible field with an electronic transition and the IR field with a vibrational transition is quite different in condensed phase as compared with gas phase systems:

(i) The line widths of electronic transitions of molecules in solution typically range from a few hundred wavenumbers to thousands of wavenumbers. In the case of homogeneous broadening, the full width half maximum ($\Delta\nu_{FWHM}$) of the absorption line is related to the dephasing time, T_2, by $T_2 = 1/(\pi\Delta\nu_{FWHM})$. Although electronic transitions may have a significant inhomogeneous broadening component, it can still be deduced that the characteristic time for dephasing

of electronic transitions is on the order of 10 to 100 fs. Femtosecond photon echo experiments on organic dye molecules in solution have given insight into the line broadening mechanisms and the time scales of dephasing processes in these systems [46–48]. At room temperature, these works show that typical electronic dephasing of a dye molecule such as the ones used in this work are in the 10 fs regime. Hence, the coherence of interaction between the UV pump pulse and the electronic transition can be left out of the theoretical consideration.

(ii) Vibrational line widths on the other hand are rarely larger than 50 cm^{-1} and values in the range 5-20 cm^{-1} are common. Exceptions are for instance the far-IR absorption spectra of some proteins [49], the OH stretching band in presence of hydrogen bonding [50] and the fundamentals of neat liquids that are associated [51], where strong inhomogeneous broadening and anharmonic coupling of different modes can cause line widths on the order of a few hundred wavenumbers. More frequently, vibrational transitions are homogeneously broadened [52–54]. Thus, commonly occurring vibrational transitions in non-associating solvents are expected to dephase exponentially with a phase relaxation time on the order of 500-1000 fs, a time scale that is definitely longer than the achievable pulse duration of the IR probing pulses.

Coherence results in an “artifact" known as perturbed free induction decay, which may be misinterpreted as an intrinsic incoherent temporal evolution of the sample. These coherence dynamics will frequently occur on the same time scale as the kinetic processes of interest and therefore must be fully understood, not only because of their intrinsic interest but also in order to extract from the experiments reliable information on population flow. In this section, a simplified physical model is introduced, which is capable to describe the perturbed free induction decay, distinguishing its effects it from “real" kinetic components caused by an ultra- fast initial chemical reaction or energy relaxation.

The appearance of the perturbed free induction decay effect in time resolved pump and probe spectroscopy can be explained qualitatively as follows (see Fig. 2.2): in a ultraviolet pump/mid-infrared probe experiment, an intense pump pulse is used to trigger a photoreaction by electronic excitation. The response of the sample is probed by monitoring, as a function of the delay time τ between pump and probe, the absorbance change of the sample with a weaker probing pulse. An absorbance change due to real kinetic components is expected only at positive delay times (positive delayed is defined as probing pulse reaching the sample after the pump pulse). However, due to the long dephasing time of a ground-state vibrational transition, the IR-probing pulse may resonantly excite a coherent polarization, that decays with its intrinsic dephasing time T_2. This coherent polarization radiates light (the so-called free induction decay) and the IR-detector will record both the probing pulse and the radiated polarization. If an excitation pulse reaches the sample after the probing pulse (at negative delay times), it can

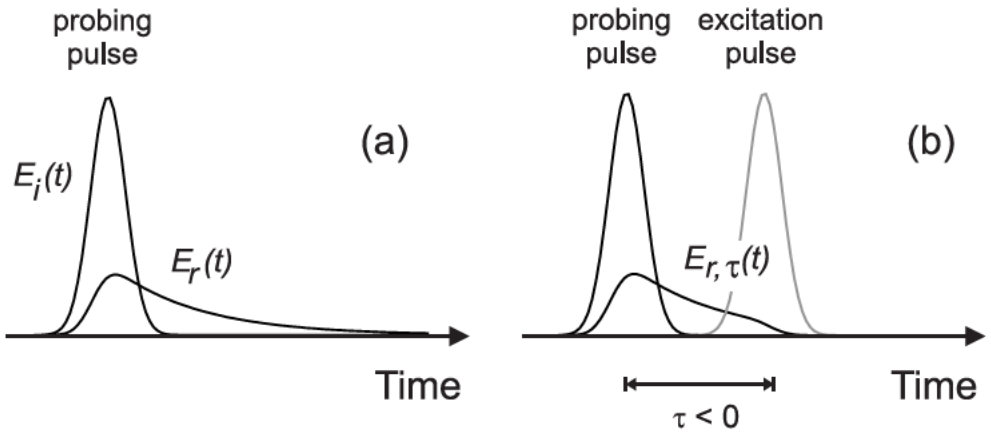

Figure 2.2: (a) The envelopes of the light fields of the incoming IR probing pulse $E_i(t)$ and of the free induction decay field radiated by the coherent polarization created in the sample $E_r(t)$. (b) The envelopes of the light fields of the incoming IR probing pulse $E_i(t)$, of the UV excitation pulse (gray line) and of the perturbed free induction decay field $E_{r,\tau}(t)$, where τ is the delay time between the probing pulse and the excitation pulse. The pump pulse perturbs the free induction decay field, which disappears after electronic excitation, resulting in measured change of absorbance in the case of pump probe experiments with frequency selective detection. The effects of perturbed free induction decay are observed only at negative time delays and during pulse overlap.

not influence the intensity of the probing pulse itself. However, it may influence the temporal or spectral properties of the probe-induced free induction decay signal of the sample, whenever the electronic excitation process modifies the strength or position of the ground-state absorption line. As a consequence, in the case of frequency resolved detection, the IR-detector will record a difference signal which decays toward negative delay times with an intrinsic time constant T_2.

The perturbed free induction decay signal is a consequence of dephasing and essentially reflects the spectral properties of the sample in the ground state and in the excited state. It does not reflect any temporal evolution of the sample related to a chemical reaction or an energy relaxation process. The evidence of absorbance changes at negative time delays is by no means a violation of the causality principle: it is rather the consequence of the fact that pump and probe spectroscopy is a third order nonlinear experiment, where both transient polarizations and population dynamics (in other words: real and imaginary part of the third order nonlinear susceptibility) contribute to the measured signals. Therefore, a realistic description of the molecular dynamics requires to distinguish between contributions of the difference signal caused by these coherent effects (often interpreted as “artifacts") and “real" kinetic components, reflecting population dynamics.

The description of the perturbed free induction decay can be done in the following way [55]. Let us consider the interaction between a single homogeneously broadened IR-absorption line and a resonant femtosecond IR-probing pulse. The probing IR pulse $E_i(t)$ generates a coherent polarization in the sample which subsequently decays with its intrinsic dephasing time T_2. The field radiated by this coherent polarization propagates in the same direction as the probing pulse and therefore is measured by the detector. Solving the Bloch equations in the low excitation limit (first order in $E_i(t)$), leads to writing the radiated field $E_r(t)$ (the so-called free induction decay, see also Fig. 2.2) as:

$$E_r(t) = \int_{-\infty}^{+\infty} M(t-t')E_i(t')\mathrm{d}t' \tag{2.8}$$

where $M(t)$ is the medium response to impulsive excitation (i.e. to a δ-shaped pulse). Eq. 2.8 can be expressed in the frequency domain as:

$$E_r(\omega) = M(\omega)E_i(\omega) \tag{2.9}$$

In a pump probe experiment with frequency resolved detection, the collected intensity is given by:

$$I(\omega) = |E_i(\omega) + E_r(\omega)|^2 = |E_i(\omega)|^2 + |E_r(\omega)|^2 + 2\ \mathrm{Re}\ E_i(\omega) \cdot E_r(\omega) \tag{2.10}$$

Assuming weak absorption, $|E_r(\omega)|^2$ is negligible with respect to the other terms. In a following step, the interaction between the free induction decay signal and a visible excitation pulse is introduced. An interaction between an excitation pulse and an incoming IR-probing pulse $E_i(t)$ is impossible when the excitation pulse reaches the sample after the IR-probing pulse (i.e. at negative delay times). However the excitation pulse may interact with the free induction decay light field $E_r(t)$. In what follows $E_r(\omega)$ and $I(\omega)$ denote the field and intensity of the unperturbed sample (in absence of the excitation pulse), and $E_{r,\omega}(t)$ and $I_\tau(\omega)$ the light field and intensity radiated by a polarization that has been perturbed by a pump pulse delayed by τ with respect to the probe pulse. In this case the difference in the transmitted intensities with and without pump is given by:

$$\Delta I_\tau(\omega) = I_\tau(\omega) - I(\omega) = 2\ \mathrm{Re}\ E_i^*(\omega)[E_{r,\tau}(\omega) - E_r(\omega)] \tag{2.11}$$

The equations 2.8, 2.9, and 2.11 do not depend on specific assumption for the broadening mechanism (homogeneous or inhomogeneous). Since the free induction decay is a linear effect, they are valid for both cases and even in the case of overlapping absorption bands, provided that a suitable response function $M(t)$ is used, related to the shape of the absorption spectrum. For a Lorentzian shaped absorption line (homogeneously broadened with a dephasing time T_2), $M(t)$ can be written as:

$$M(t) = \Theta(t)\exp(-t/T_2)\exp(-i\omega_a t) \tag{2.12}$$

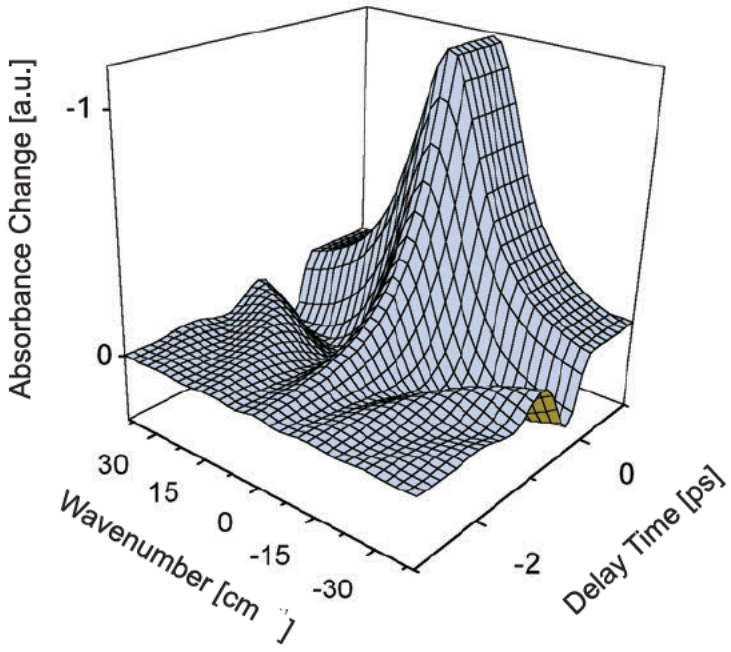

Figure 2.3: Calculated change of absorbance as a function of delay time and wavenumber. The model assumes infinite time resolution (δ-pulses) and a dephasing time of 600 fs, corresponding to a typical bandwidth of 18 cm^{-1}. The frequency coordinate is the difference frequency $\omega - \omega_a$ between the detection frequency and the peak position of the absorption line.

where $\Theta(t)$ is the Heaviside function and ω_a is the center frequency of the absorption line. In this case $M(\omega)$ is a Lorentzian function with center frequency ω_a.

It is convenient to introduce the function $G_\tau(t)$, which describes the relative variation of the pump-induced polarization (i.e. the change of oscillator strength of the IR absorption line upon electronic excitation):

$$G(t) = [E_r(t) - E_{r,\tau}(t)]/E_r(t) \tag{2.13}$$

With this notation, the difference signal has the following general expression:

$$\begin{aligned} \Delta T(\omega,\tau) &= \frac{\Delta I_\tau(\omega)}{I_i(\omega)} = \\ &- \frac{2\mathrm{Re}E_i^*(\omega)\int_{-\infty}^{+\infty} G_\tau(\omega')M(\omega-\omega')E_i(\omega-\omega')\mathrm{d}\omega'}{E_i^*(\omega)E_i(\omega)} \end{aligned} \tag{2.14}$$

Let us consider the situation where the excitation pulse leads to a bleaching of the IR absorption line: the radiated field $E_r(t)$ disappears when the excitation pulse reaches the sample. In the simplified case of δ-shaped excitation and probing pulses, one finds $G_\tau(t) = \Theta(t+\tau)$ and $E_i(\omega) = 1$ and, assuming homogeneous broadening, one can solve Eq. 2.14 analytically:

$$\Delta T(\omega,\tau) \quad \propto$$

$$\begin{cases} -\, e^{t/T_2}\dfrac{\cos[(\omega-\omega_a)\tau] + (\omega-\omega_a)\sin[(\omega-\omega_a)\tau]}{(\omega-\omega_a)^2 + (1/T_2)^2} & \tau < 0 \\ -\,\dfrac{1}{(\omega-\omega_a)^2 + (1/T_2)^2} & \tau > 0 \end{cases} \tag{2.15}$$

Fig. 2.3 shows a 3D-plot of the absorbance change as function of the pulse delay and of the frequency, calculated for a dephasing time of 600 fs, corresponding to a bandwidth of 18 cm^{-1}. For positive delay times the signal does not evolve with time and shows a Lorentzian band shape. At negative delay times, the typical features of the perturbed free induction decay appear: at the center of the absorption line, the signal rises exponentially with a time constant equal to T_2; off-resonance, the signal shows oscillations as a function of time, with a frequency equal to the detuning between line center and detection frequency $(\omega - \omega_a)$.

It is important to realize that the features of perturbed free-induction decay manifest themselves only in spectrally resolved experiments. As a matter of fact, integrating the function 2.15 over frequency yields:

$$\int_{-\infty}^{+\infty} \Delta T(\omega,\tau)\mathrm{d}\omega \quad \propto \quad \Theta(\tau) \tag{2.16}$$

The signal is zero at negative delay times, and grows instantaneously at delay zero. This fact has been interpreted as a manifestation of the uncertainty principle [55], whereby the introduction of spectral resolution, providing information on the spectral properties of the sample, limits the actual temporal resolution to the response time of the sample (inverse of the bandwidth of the absorption line). To recover the true bleaching kinetics, one has to monitor the differential spectra *integrated* over a spectral bandwidth at least of the order of the inverse temporal accuracy.

For a more realistic model calculation, a finite pulse duration of the laser pulses can be easily implemented in this model. To model the experiments performed in this work it is enough to assume a Gaussian shape for probing pulses ($E_i(t) \propto \exp[-t^2\Delta\omega^2/2]$, $E_i(\omega) \propto \sqrt{2\pi}/\Delta\omega \exp[-\omega^2(2\Delta\omega^2)]$), whereas the excitation pulses can still be modeled by δ-shaped pulses (see Chapter 3: in the experiments UV pulses are typically four times shorter than the infrared pulses).

In this case, Eq. 2.14 can be efficiently evaluated numerically [38]. The result are qualitatively similar to the case of δ-shaped probing pulses shown in Fig. 2.3, with a smoothing of the signal changes at delay zero and more pronounced oscillations at the frequency positions corresponding to the spectral wings of the probing pulses. In the case of infinite time resolution, perturbed free induction decay is observed strictly at negative delay times, and all processes are separated in time, as a consequence of the temporal asymmetry of the light field originating from the free induction decay: perturbed free induction decay ($\tau < 0$), excitation ($\tau = 0$) and subsequent reaction or relaxation dynamics ($\tau > 0$). In an experiment with realistic time resolution, a mixture of the all processes takes place within the cross correlation time.

Up to now a complete bleaching of an isolated absorption line following electronic excitation has been considered. More general situations can be derived from this formalism [38]. In the case where, for instance, the oscillator strength of an absorption band increases or decreases upon the excitation, it is sufficient to introduce a scaling factor for the perturbed free induction decay signal, depending linearly on the change of oscillator strength. Also a spectral shift of an absorption band can be treated to a good approximation, provided that the shift is small compared to the bandwidth of the line, as the linear superposition of an oscillator strength decrease at ground state position and an increase at excited state position.

If an absorption line is generated after the optical excitation process the IR transition does not interact with the probing pulse in the ground state and no perturbed free induction decay will be observed. This is for example the case of a vibrational line created after a photoinduced reaction, or shifted after excitation from a frequency position outside the spectral range of the probing pulse. Hence, as consequence of the temporal asymmetry of the pump-probe experiment, there is also an asymmetry (bleaching/rise of an absorption line) in the perturbed free induction decay response.

2.4 Effects of anharmonicity

To describe the motion of a polyatomic molecule with N atom one needs $3N$ coordinates, in other words: there are $3N$ degrees of freedom, of which $3N-6$ ($3N-5$ for linear molecules) are *vibrational degrees of freedom*. In the harmonic approximation, where only quadratic terms are included in the function describing the potential energy, any motion of the system can be represented as a superposition of normal modes of vibration. Under this approximation, the total vibrational eigenfunction is simply a product of oscillator eigenfunctions corresponding to the different normal coordinates. Each normal mode is an ideal harmonic oscillator, whose energy spectrum is an equidistant ladder. From a theoretical point of view, the normal modes of vibration can unambiguously be determined by

solving a secular equation if the force constants defining the harmonic potential energies are known. However, there are many evidences of the breakdown of the harmonic approximation and of the separation into normal coordinates. If the potential energy consisted of only quadratic terms, it would require infinite energy to break a valence bond. From a theoretical point of view, it is necessary to introduce cubic, quartic and possibly higher order terms into the expression for the potential energy to achieve a better description: the Schroedinger equation no longer resolves into a number of independent equations for each normal mode, the energy is no longer a sum of independent terms corresponding to the different normal vibrations but contains also cross terms involving the quantum number of two or more normal vibrations [40].

Two aspects of anharmonicity are particularly relevant in this thesis in order to extract information from the measurement of transient vibrational spectra:

(i) *Diagonal anharmonicity:* in a harmonic oscillator the energy spectrum is equidistant, i. e., the frequency of the ground state transition $v = 0 \rightarrow v = 1$ and that of a higher transition $v = n \rightarrow v = n + 1$ are identical, whereas the absorption cross section $A(v = n \rightarrow v = n + 1)$ scales linearly with $(n + 1)$ and the stimulated emission cross section $-A(v = n + 1 \rightarrow v = n)$ with n. This makes it impossible to distinguish between the case where a given vibrational mode is in its ground state and the case where the mode is in an excited state. As soon as the harmonic approximation breaks down, the anharmonicity gives rise to frequency shifts, producing measurable difference bands. Anharmonicity is thus essential to understand the spectrum of a vibrationally excited molecule. This aspect will be used in order to judge whether a given vibrational mode, observed in a transient vibrational spectrum, appears to be selectively excited (see Chapter 4, Section 4.4 and Chapter 6).

(ii) *Off-diagonal anharmonicity:* the anharmonic coupling to other vibrational modes affects the spectral position and width of a vibrational line. By monitoring the shape and position of one vibration, one sees, albeit in an indirect way, the effect of processes (i. e. intramolecular vibrational redistribution, cooling) which change the population of the anharmonically coupled vibrations, deducing information about the relevant time scales (see Chapter 4, Section 4.4.3). Coherence phenomena due to wavepacket motions along anharmonically coupled vibrational modes have also been observed (see Chapter 4, Section 4.4.2).

In the following, the formalism of the anharmonic constants is reviewed. It can be derived using perturbation theory [40, 56], using an espression for the potential energy which includes cubic and quartic force constants in a normal coordinate basis: the system is described in the harmonic approximation (in the formalism of eigenfrequencies and eigenmodes), while anharmonicity is treated by perturbation theory. Including the anharmonic corrections, the total vibrational

energy of a molecule can assume only the values [40, 41]:

$$\frac{E(v_1, v_2, v_3, ...)}{\hbar} = \sum_i \omega_i \left(v_i + 1/2\right) + \sum_{i \leq j} x_{ij} \left(v_i + 1/2\right) \left(v_j + 1/2\right) \tag{2.17}$$

where ω_i is the *harmonic* frequency of the $i-th$ vibrational mode, $v_i = 0, 1, 2...$ is the vibrational quantum number of the $i-th$ mode, and $x_{i,j}$ are the anharmonicity constants, which can be related to the cubic and quartic force constants in a normal coordinate basis. A given vibrational mode k is coupled to the bath of the remaining modes $i \neq k$ and its transition frequency is given by:

$$\omega(v_k \rightarrow v_k + 1) = \omega_k + 2x_{kk}v_k + \sum_{i \neq k} x_{ik}v_i \tag{2.18}$$

where the first term is the anharmonic correction of the $v_k = 0 \rightarrow v_k = 1$ transition in the vibrational ground state:

$$\omega_k = \omega_k^0 + 2x_{kk} + \sum_{i \neq k} x_{ik}/2 \tag{2.19}$$

The second term of Eq. 2.18 describes the "diagonal" anharmonic shifts of an excited vibrational mode k, while the last term describe the frequency shifts due to the "off-diagonal" anharmonicity between the selected mode k and the remaining modes.

Using the Eq. 2.18, the shape of the absorption line $A_k(\omega)$ of a given vibrational mode k can then be derived, modeling the cross section for absorption and stimulated emission in the harmonic approximation and applying the "Golden Rule" [39]:

$$\begin{aligned} A_k(\omega) \propto \sum_{v_k} \Bigg\{ & (\alpha(v_k) - \alpha(v_k + 1))(v_k + 1) \\ & \times \sum_{v_1..n_m} \left[\prod_{j \neq k} \alpha(v_i) \cdot \delta(\omega - \omega_k - 2x_{kk}v_k) - \sum_{j \neq k} x_{ik}v_i \right] \Bigg\} \end{aligned} \tag{2.20}$$

m is the total number of vibrational modes, δ is the delta function (it can be easily replaced by a line shape function with finite bandwidth), $\alpha(v_k)$ is a given population distribution of the mode k, normalized in such a way that $\Sigma_{n_k}\alpha(v_k) = 1$, $\alpha(v_i)$ is the population distribution functions for all modes $i \neq k$, with the same normalization. The term $\alpha(v_k)$ describes the absorption $v_k \rightarrow v_k + 1$, the term $-\alpha(v_k + 1)$ takes into account the stimulated emission $v_k + 1 \rightarrow v_k$.

It must be noted that this formalism describes the shape of a vibrational band in a static picture, in terms of populations, whereas a complete dynamic

picture should also consider the polarization of the vibrational transitions [37,38]. However, for time scales beyond a few picoseconds, this should be a reasonable approximation.

Already in the case of relatively small molecules, determination of the anharmonic constants is a challenging task. From an experimental point of view it requires the knowledge of a complete set of overtones and combination bands. From a theoretical point of view, the calculation of the Taylor expansion of the ground state potential surface to fourth order with sufficient precision is required [41]. For dye molecules such as the ones studied in this work it is at the present time an impossible task; by means of *ab initio* calculations of the third and fourth derivatives of the energy, anharmonic effects in the infrared and Raman spectra of benzene have been examined. Anharmonic corrections for the vibrational modes and for the Raman scattering factors, intensities for the infrared spectrum as well as a complete set of anharmonic constants have been determined for the case of benzene [57, 58]. For such a molecule (with 12 atoms and 30 vibrational degrees of freedom), despite the simplification due to the symmetry of the problem, this is already considered a challenging task [57, 58].

(i) Selective excitation of a vibrational mode

Anharmonicity permits to address experimentally the selective flow of energy into one vibrational mode, i.e. to verify if the population of a given vibrational mode deviates significantly from a thermal distribution. As long as the harmonic approximation holds, no absorption changes are expected in a transient vibrational spectrum when exciting a vibrational mode from the ground state to a vibrationally excited state. This is a consequence of the quantum mechanical properties of the harmonic oscillator: (i) The energy spectrum is equidistant, i.e., the frequency of the ground state transition $v = 0 \rightarrow v = 1$ and that of a higher transition $v = n \rightarrow v = n + 1$ are identical. (ii) The absorption cross section $A(v = n \rightarrow v = n + 1)$ of a vibrationally excited mode increases linearly with $(n + 1)$ [59]. However, stimulated emission gives rise to a negative contribution $-A(v = n + 1 \rightarrow v = n)$ which increases linearly with n, i.e., the sum of both contributions is independent on n and does not change with the level of excitation. Anharmonicity gives rise to anharmonic frequency shifts and consequently is responsible for detectable difference bands. This is illustrated in Fig. 2.4 and Fig. 2.5, where the shape of the absorption bands for a C=O vibration at 1530 cm^{-1} in the $v = 0$ and in the $v = 1$ state is schematically shown for an harmonic and Morse potential respectively. Fig. 2.4 shows the results obtained assuming an harmonic potential for the oscillator ($\nu_{10} = \nu_{21} = 1530$ cm^{-1}, linewidth of 12.5 cm^{-1} (FWHM)). On the other hand, assuming a Morse potential for the oscillator ($\nu_{10} = 1530$ cm^{-1}, $\nu_{21} = 1520$ cm^{-1}; $\nu_{10} - \nu_{21} = 10$ cm^{-1}, same linewidth) one gets the picture of Fig. 2.5. For a harmonic oscillator one would not expect to observe any changes in absorbance between the two situations, since the excited-state $v = 1 \rightarrow v = 2$ absorption has a cross section which represents

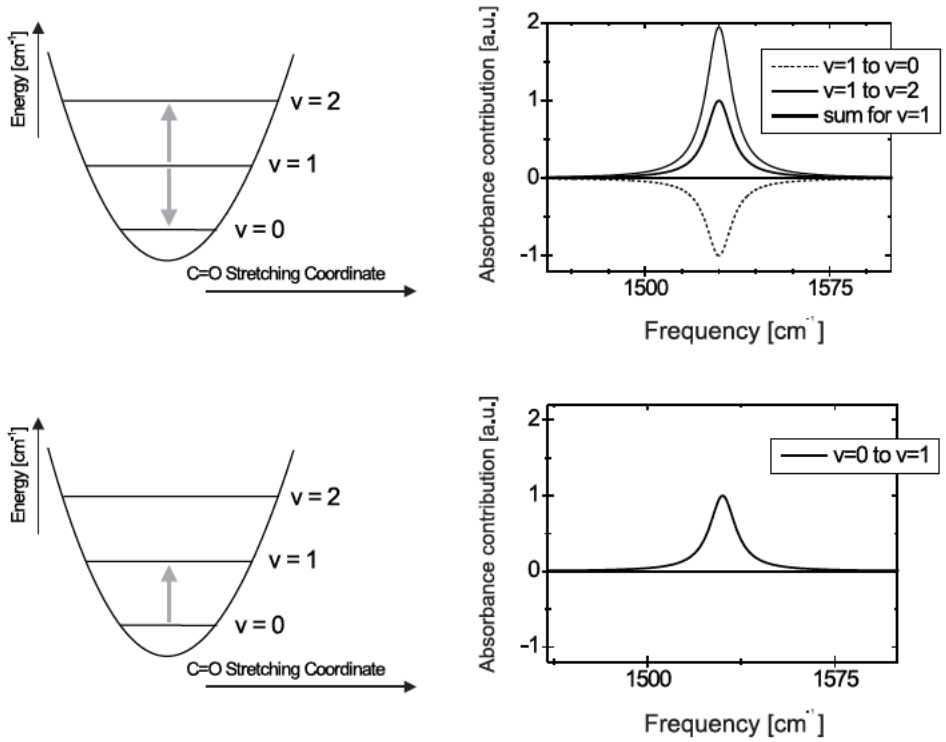

Figure 2.4: Calculated shape of the absorption bands for a C=O vibration at 1530 cm^{-1} in the $v = 0$ (upper panels) and in the $v = 1$ state (lower panels). An harmonic potential for the oscillator was assumed ($\nu_{10} = \nu_{21} = 1530$ cm^{-1}) and a linewidth of 12.5 cm^{-1} (FWHM). Under the harmonic approximation the two cases are undistinguishable.

twice that of stimulated emission from the $v = 1 \rightarrow v = 0$ transition. For an anharmonic oscillator similar ratios in transition moments occur for moderate anharmonicities [60]. However the anharmonic shift between the $v = 0 \rightarrow v = 1$ and the $v = 1 \rightarrow v = 2$ leads to spectrally displaced excited-state absorption and stimulated emission bands. For the C =O stretching mode with an estimated anharmonic shift of 15 cm^{-1} the two cases should be easily distinguishable. In a time resolved experiment, if a vibrational mode is transiently created in its excited state, the measured spectra should carry the evidence of the spectral reshaping of the band due to the relaxation $v = 1 \rightarrow v = 0$, provided that the time resolution is shorter than the relaxation time T_1.

(ii) Anharmonic coupling to low frequency modes

The following elementary example [39] illustrates how the anharmonic coupling to highly populated modes can modify the shape and position of a given vibration. Using the formalism presented in this section, a temperature dependent shape of an absorption line of the benzene molecule can be calculated. The ν_{19} vibrational

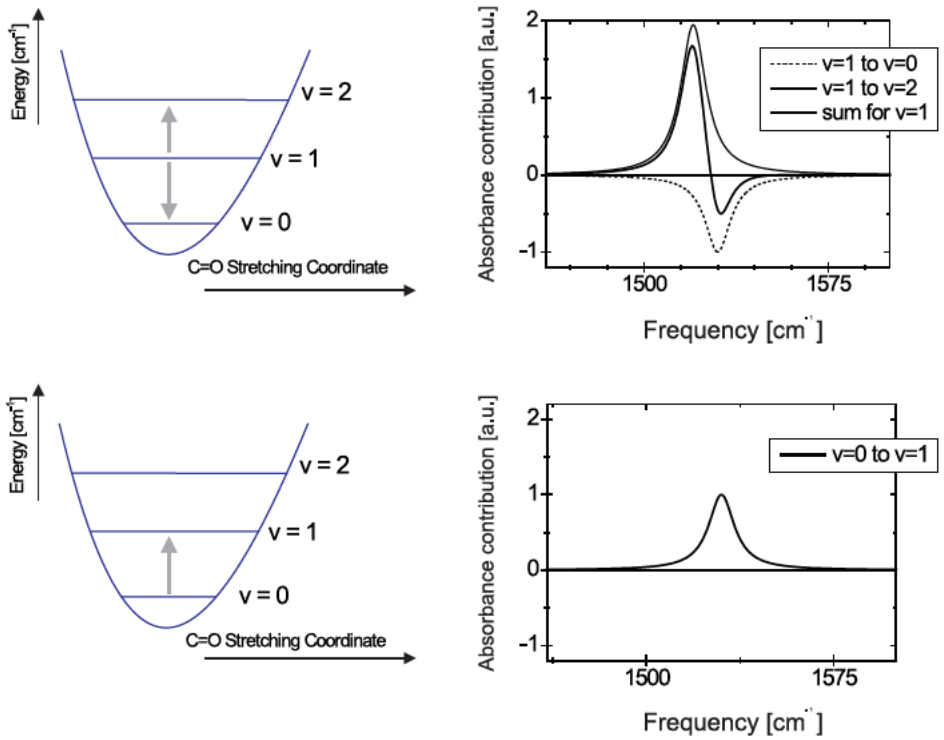

Figure 2.5: Calculated shape of the absorption bands for a C=O vibration at 1530 cm^{-1} in the $v = 0$ (upper panels) and in the $v = 1$ state (lower panels). A Morse potential for the oscillator was assumed (ν_{10} = 1530 cm^{-1}, ν_{21} = 1520 cm^{-1}, $\nu_{10} - \nu_{21}$ = 10 cm^{-1}) and a linewidth of 12.5 cm^{-1} (FWHM). Anharmonicity makes the two cases distinguishable through the anharmonic frequency shift.

mode of benzene (at 1484 cm^{-1}) was selected and its absorption line was calculated using Eq. 2.20, with the harmonic frequencies and anharmonic constants reported in Ref. [57]. The broadening (homogeneous or inhomogeneous) of the transition was taken into account by convoluting the calculated curves with a Gaussian line shape function with a FWHM of 2 cm^{-1}. For different temperatures, a thermal Boltzmann distribution for the population distribution functions $\alpha(n_i)$ for the intramolecular modes was assumed.

The results are shown in Fig. 2.6, starting at room temperature (300 K) and continuing with several higher temperatures up to 1100 K. At room temperature, only a minor frequency shift of -0.05 cm^{-1} with respect to the zero-temperature position is observed. Increasing the temperature has two effects: a frequency shift increasing considerably at higher temperatures (from -0.15 cm^{-1} at 400 K up to -5 cm^{-1} at 1150 K) and a strong asymmetric broadening of the band. The red-shift as a function of temperature is a consequence of the fact that almost all of the anharmonic constants $x_{i,19}$ are negative. The main contribution to

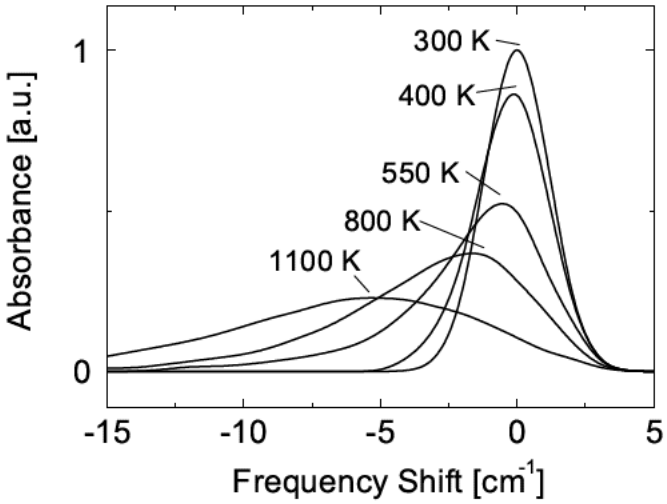

Figure 2.6: Calculated shape of the ν_{19} of benzene at different temperatures. Changing the temperature modifies the population distribution in the bath of the intramolecular vibrational modes. This in turn affects the shape of the ν_{19} mode through the *non diagonal* anharmonic coupling. The measurements of the absorption spectra can be used as a "molecular thermometer" for the intrinsic temperature of the solute molecule.

the anharmonic effects is here due to the off-diagonal anharmonic constants x_{ik}, $i \neq k$, and not due to the diagonal term $2x_{kk}$: even at the highest temperature used in this simulation, the excitation probability of the ν_{19} mode is only 15% and the diagonal harmonic constant ($2x_{19,19} = -1.8$ cm^{-1}) is small as compared to the sum of the off-diagonal elements of all low-frequency modes ($\sum x_{i,19} = -21$ cm^{-1}), which are excited considerably at this temperature. Therefore, these modes are responsible for the anharmonic effect determining the reshaping of the ν_{19} absorption band. In the previous discussion, a Boltzmann (i.e. thermalized) distribution of population has been assumed. However, shifting of vibrational lines can be also due to the selective, non-thermal excitation of a limited number of vibrational modes. Typically red-shifts are observed also in this case, since usually anharmonic constants have negative values [39].

2.5 Effects of rotational relaxation

In the liquid phase, due to the very short times between collisions with the surrounding molecules, one can expect short timescales for all processes involving energy and phase loss through interaction with the environment [42]. In particular, in some of the experiments described in this thesis (see Chapter 5), it is

important to take into account the effect of rotational relaxation on the outcome of the measurements, since the molecular dynamics under observation are characterized by comparable time scales. The study of molecular motion in liquids has traditionally been carried out using time-resolved absorption or emission spectroscopy, or exploiting the optical Kerr effect [61,62], and a general formalism has been developed with which one can describe time-resolved experiments sensitive to orientational motion [42]. This formalism, which will be briefly reviewed in this section, has here been applied in order to separate the molecular dynamics from the effects of rotational relaxation.

In the ultraviolet pump/mid-infrared probe time-resolved experiments discussed in this thesis, linearly polarized light is used, both for the UV pump and the mid-infrared pulses, as a consequence of the schemes for pulse generation. The photo-selection process, performed with vertically polarized light, defines a specific geometry for the system, exciting preferentially (with a cos^2 law) those molecules for which the dipole moment of the electronic transition is parallel to the polarization of the incoming field. The mid-infrared probing pulses interact with the various vibrational transitions showing, in general, an initial anisotropy, which decays to zero as soon as the molecules reach an isotropic orientational distribution. The experimentally measured light intensities can then be related to two aspects: the kinetics describing the time-dependent population of the levels involved and the correlation functions that describe the molecular motion.

Following the treatment of Ref. [42], one can define a molecular axis system coinciding with the principal axis of the diffusion tensor and a normalized probability distribution $f^{(i)}(\mathbf{\Omega}, t)$ of finding a molecule in an electronic state (i) with orientation between $\mathbf{\Omega}$ and $\mathbf{\Omega} + d\mathbf{\Omega}$, such that the density of molecules $K^{(i)}(t)$ in a level (i) is given by:

$$K^{(i)}(t) = \int \mathrm{d}\mathbf{\Omega} f^{(i)}(\mathbf{\Omega}, t) \tag{2.21}$$

In order to relate $f^{(i)}$ to measurable quantities one can introduce an orientation dependent operator which extracts the contribution made to the observable by molecules with a given orientation, and then integrate over all possible orientations. It is then possible to define effective parallel and perpendicular concentrations of molecules giving rise to IR absorption from a given level:

$$\begin{aligned} N_{\parallel}^{(i)}(t, \gamma) &= \int \mathrm{d}\mathbf{\Omega} \widehat{P}_{\parallel}(\mathbf{\Omega}, t) f^{(i)}(\mathbf{\Omega}, t) \\ N_{\perp}^{(i)}(t, \gamma) &= \int \mathrm{d}\mathbf{\Omega} \widehat{P}_{\perp}(\mathbf{\Omega}, t) f^{(i)}(\mathbf{\Omega}, t) \end{aligned} \tag{2.22}$$

where $\widehat{P}_{\parallel}(\mathbf{\Omega}, t)$ and $\widehat{P}_{\perp}(\mathbf{\Omega}, t)$ are proportional to the probabilities of a molecule with orientation $\mathbf{\Omega}$, and a transition dipole with direction cosines in the molecular axis system γ, interacting with a light field polarized in the laboratory parallel

or perpendicular direction, respectively. In order to measure $K^{(i)}(t)$, not affected by orientational information, it is necessary to measure at two orthogonal polarizations, so that:

$$K^{(i)}(t) = N_{\parallel}^{(i)}(t,\gamma) + 2N_{\perp}^{(i)}(t,\gamma) \tag{2.23}$$

regardless of the orientation specified by gamma.

One can define an effective anisotropy associated with the transition dipole γ:

$$r^{(i)}(t,\gamma) = \frac{N_{\parallel}^{(i)}(t,\gamma) - N_{\perp}^{(i)}(t,\gamma)}{N_{\parallel}^{(i)}(t,\gamma) + 2N_{\perp}^{(i)}(t,\gamma)} \tag{2.24}$$

so that the signals measured at parallel and perpendicular polarization can be written in the following form:

$$\begin{aligned} N_{\parallel}^{(i)}(t,\gamma) &= \frac{1}{3}K^{(i)}(t)[1 + 2r^{(i)}(t,\gamma)] \\ N_{\perp}^{(i)}(t,\gamma) &= \frac{1}{3}K^{(i)}(t)[1 - r^{(i)}(t,\gamma)] \end{aligned} \tag{2.25}$$

The effective anisotropy contains information about the orientational distribution of the transition dipoles γ for molecules in state (i). The description of an experiment is reduced to writing explicit expressions for the time-dependent r and K functions. In the case where only one electronic state is prepared, $r(t)$ is given by an expression involving the second Legendre polynomial (P_2) of the correlation of the transition moment direction at time zero with that at time t:

$$r(t,\gamma) = \frac{2}{5}\langle P_2(\mu(0)) \cdot \gamma(t)\rangle \tag{2.26}$$

where μ is the transition dipole associated with the preparation of the excited state (UV electronic absorption) and γ is the transition dipole associated with the probing event (IR vibrational absorption). The anisotropy function contains information about the relative orientation between the electronic and the infrared dipole moments. In the case where the electronic and the vibrational transitions are polarized along specific directions in the molecular frame, this fact can be used to deduce information about the molecular structure. For instance, by using time resolved infrared polarization spectroscopy, it has been possible to determine the relative orientation of carbon monoxide (CO) bound to and dissociated from myoglobin in solution [63].

The expression 2.26 does not depend on any particular model for the molecular motion. The rotational diffusion model [64] describes reorientation as occurring by small steps: collisions are so frequent that a molecule can only rotate through a very small angle before suffering another reorienting collision. This model leads

to an expression for the molecular anisotropy $r(t)$ which, in the most general case of an asymmetric rotor, contains five exponentials:

$$\begin{aligned} r(t) = \frac{6}{5}\sum_{i=1}^{3} c_i \exp(-t/\tau_i) \quad &+ \quad [(F+G)/4]\exp(-[6D-2\Delta]t) \\ &+ \quad [(F-G)/4]\exp(-[6D+2\Delta]t) \end{aligned} \tag{2.27}$$

$$\begin{aligned} \Delta &= (D_1^2 + D_2^2 + D_3^2 - D_1D_2 - D_1D_3 - D_2D_3)^{\frac{1}{2}} \\ c_i &= \alpha_j\alpha_k\varepsilon_j\varepsilon_k; \qquad (ijk) \in \{(123),(231),(312)\} \\ \tau_i &= 1/(3D + 3D_i) \\ F &= \sum_{i=1}^{3} \alpha_i^2\varepsilon_i^2 - \frac{1}{3} \\ G\Delta &= \sum_{i=1}^{3} D_i(\alpha_i^2\varepsilon_i^2 + \alpha_j^2\varepsilon_k^2 + \alpha_k^2\varepsilon_j^2) - D \qquad i \neq j \neq k \end{aligned}$$

where α_1, α_2, α_3 are the cosines of the dipole moment of the electronic transition with respect to the principal axes of rotation, ε_1, ε_2, ε_3 are the cosines of the dipole moment for the vibrational transition, D_α (α=1,2,3) are the diagonal elements of the diffusion tensor in the molecular-coordinate system, $D = (D_1 + D_2 + D_3)/3$ is the mean diffusion coefficient. This complicated expression can be simplified in the case of certain classes of molecular symmetry. In order to describe the experimental data presented in this thesis, it is sufficient to model the molecules as fully symmetrical, spherical rotors. In this case $D_1 = D_2 = D_3 = D_s$ and $r(t)$ is then simply given by:

$$r(t) = \frac{2}{5}P_2(\cos\lambda)\exp(-6D_st) \tag{2.28}$$

where λ is the angle between the electronic absorption and the vibrational absorption dipole moments. The motion is isotropic with a rotational-correlation time $\tau_{rot} = 1/6D_s$. In the case where the electronic and the infrared dipole moment have a relative orientation forming an angle of $\theta = 54.74°$ ("magic angle") one gets $r(t) = 0$ and $N_\parallel = N_\perp$: measuring at either parallel or perpendicular polarization gives the same signal, which is not affected by orientational information.

A more complete discussion, addressing different types of symmetries can be found in Ref. [42].

Chapter 3

Experimental

3.1 Introduction

Because of the small cross sections of vibrational transitions (as compared, e.g., to those of electronic transitions), ultrafast IR experiments are still challenging and the progress in this field had to wait for sufficiently robust and reliable sources. Only recently, mid-infrared femtosecond sources were developed which satisfy the technical prerequisites for broad application of ultrafast vibrational spectroscopy.

Generation of tunable femtosecond mid-infrared pulses is usually based on techniques of nonlinear optical frequency mixing in second order nonlinear materials. Optical parametric oscillators have been shown to generate mid-IR pulses with nanojoule energies as short as 50 fs [65, 66]. At kHz repetition rates, intense near-infrared pulses, originating from regenerative Ti:sapphire amplifiers, have been used routinely to generate femtosecond (50-150 fs) microjoule mid-infrared pulses in the wavelength range from 2.5 to 20 μm with a variety of conversion schemes [67–69]. Besides, techniques for generating phase-shaped mid-infrared pulses have been proposed and demonstrated [70, 71]. Free-electron lasers (FELs) [72] also cover the mid-infrared spectral region with (sub)picosecond time-resolution, wide tunability and microjoule energies per pulse, but the synchronization with an external laser source remains problematic. Synchronization of a FEL with a mode-locked Ti:sapphire laser with a jitter of about 400 fs has been demonstrated recently [73]. Up to now, infrared radiation from FELs has been applied to vibrational spectroscopy to much lesser extent.

In this chapter, the experimental setup used for the ultraviolet pump/mid-infrared probe experiments is described. In Figure 3.1 an overview of the experimental setup is shown. The system is based on a home-built 1-kHz Ti:sapphire laser with chirped pulse amplification, generating intense light pulses at 800 nm with an energy of about 1 mJ per pulse at a repetition rate of 1 kHz. The pulses are then split by a beam splitter to pump simultaneously two stages for frequency conversion. The near-UV pump pulses for electronic excitation were

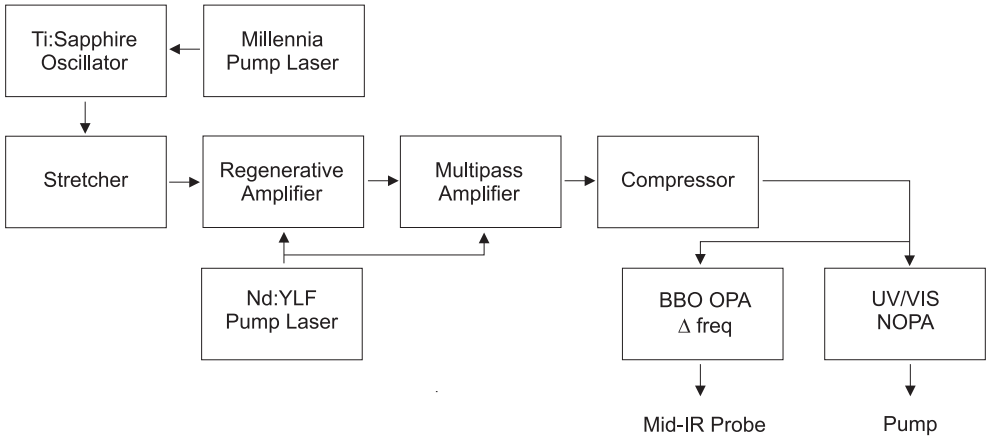

Figure 3.1: Overview of the experimental set-up for ultraviolet pump/mid-infrared probe experiments. The output of the multipass amplifier, after compression, pumps two stages for frequency conversion, which produce, by means of parametric processes, pump pulses tunable in the ultraviolet and probe pulses tunable in the mid-infrared spectral range.

obtained by sum frequency mixing of the fundamental and visible pulses generated by a noncollinear optical parametric amplifier. The mid-infrared probe pulses were generated using double-pass collinear optical parametric amplification, followed by difference frequency mixing of signal and idler. Ultraviolet and mid-infrared pulses were then combined in a standard pump and probe scheme.

3.2 The laser system

The system is based on a home-built femtosecond kHz laser with chirped-pulse amplification [74]. It is seeded by 15-femtosecond laser pulses, coming from a Kerr-lens mode-locked Ti:sapphire oscillator, with chirped-mirror dispersion compensation [75]. Titanium doped sapphire (Ti:Al_2O_3) is the standard material for short-pulse generation [76, 77], offering the necessary broad bandwidth and a well separated absorption spectrum. Exploitation of the enormous bandwidth of Ti:sapphire (≈100 THz) has become possible with the discovery of self-mode-locking (Kerr-lens mode locking), a method where a passive amplitude modulation with virtually instantaneous response is introduced without the need for inserting any additional dispersive element in the cavity [78]. The insertion in the cavity of chirped multilayered dielectric mirrors allows an optimal control of the dispersion, leading to almost bandwidth-limited pulses [75].

The seed pulses are then stretched by a factor of 10000 by use of an all-reflective-optics stretcher capable of controlling higher order dispersion [79]. A flash-lamp pumped Q-switched intracavity-frequency-doubled Nd:YLF laser de-

livering an average output power of 15 W at 532 nm pumps a 10-round-trip regenerative Ti:sapphire amplifier, followed by a two-pass Ti:sapphire power amplifier, at a repetition rate of 1 kHz. The 2 mJ amplified pulses, are finally recompressed with a reflective grating pair. After compression intense (1 mJ), short (40 fs) pulses at 1kHz, with a spectrum peaking at 795 nm, are available for pumping the following optical parametric processes.

3.3 Nonlinear parametric conversion

In order to convert the amplifier output into the desired mid-IR and UV frequency range, various nonlinear processes have been applied, such as parametric amplification, sum frequency mixing and difference frequency mixing. They are three-wave mixing effects and require solid state materials with a nonvanishing second order nonlinearity $\chi^{(2)}$. In a $\chi^{(2)}$ medium, pulses at frequencies ω_p (pump), ω_s (signal) and ω_i (idler) (conventionally $\omega_p > \omega_s > \omega_i$) can interact with each other through the induced second-order polarization [43]. The conservation of energy requires:

$$\omega_p \quad = \quad \omega_s + \omega_i \tag{3.1}$$

In parametric generation and amplification, an intense input pulse at ω_p generates and amplifies pulses at ω_s and ω_i. In difference frequency mixing, pulses at $\omega_i = \omega_p - \omega_s$ are generated from two input pulses at ω_p and ω_s. In sum frequency mixing, pulses at $\omega_p = \omega_s + \omega_i$ are generated from two input pulses at ω_s and ω_i.

In order to maximize the coupling between the three interacting fields, the wavevectors must satisfy the phase matching condition [43]:

$$\mathbf{k_p} \quad = \quad \mathbf{k_s} + \mathbf{k_i} \tag{3.2}$$

where $|\mathbf{k_i}| = n_{p,s,i} \cdot (\omega_{p,s,i}/c)$. This condition can be fulfilled in nonlinear birefringent materials, by adjusting the refractive indices $n_{p,s,i}$ (c: vacuum light velocity). By rotating the angle between the direction of propagation and the optical axis of the crystal, one can change the wavelength for which phase matching is fulfilled and hence tune the parametric interaction.

In the femtosecond regime, another important issue is the unavoidable mismatch of the group velocities of the three interacting pulses. This poses limitations on the effective interaction length in the nonlinear medium as well as on the minimum pulse duration achieved [80].

3.3.1 Femtosecond infrared pulses

The setup described in the following was built in order to generate intense and widely tunable mid-infrared light pulses, with the high shot-to-shot stability that

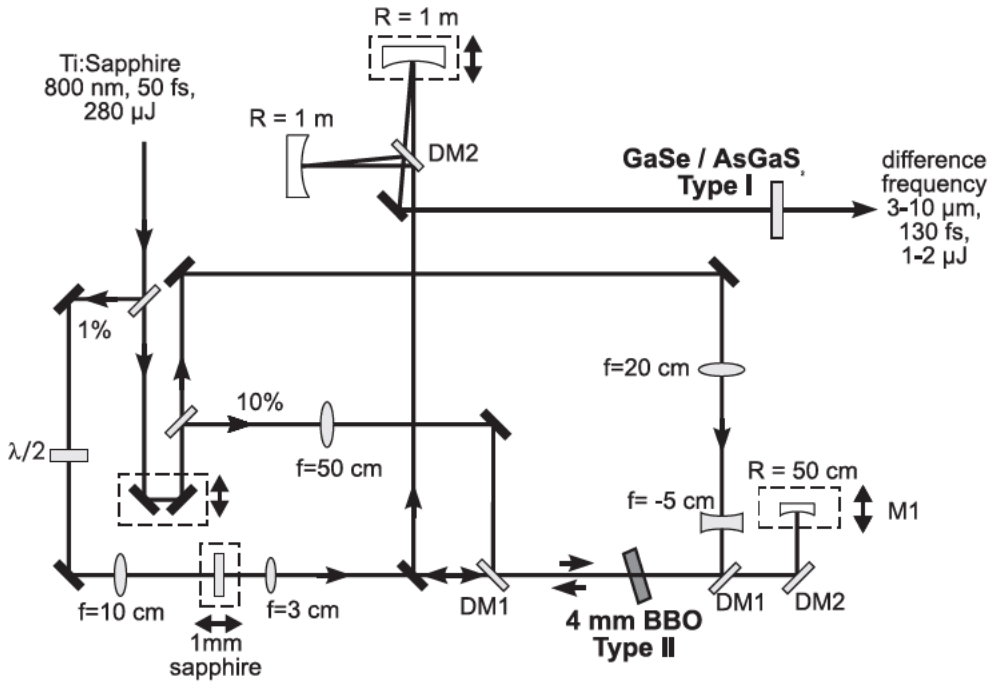

Figure 3.2: Experimental setup for the generation of tunable femtosecond mid-infrared pulses. The two-stage optical parametric amplifier based on BBO is followed by difference frequency mixing in a nonlinear crystal ($GaSe/AgGaS_2$). In the actual setup, the beams for the first and second step of amplification in the BBO crystal are displaced in height. $\lambda/2$: half-wave plate.

is needed in order to perform experiments of vibrational spectroscopy. It consists of two steps of frequency conversion: first, near-infrared signal and idler pulses ($\lambda = 1.2 - 2.4\ \mu m$) are obtained in an optical parametric amplifier (OPA) based on β-barium borate crystal(BBO). Finally, difference frequency mixing (DFM) in a second-order nonlinear crystal generates the desired mid-infrared (MIR) pulses tunable in an extremely broad spectral range (3-20μm). The configuration is shown in Figure 3.2. The design is similar to that described in References [68, 69, 81].

Seed pulses for pumping the OPA are generated by focusing a small portion ($\sim$1%) of the amplified 800-nm pulses in a 1 mm-thick sapphire window, thus producing a single-filament white-light continuum. The seed pulses and a fraction (10%) of the temporally delayed pump pulses are then overlapped, spatially and temporally, in a 4 mm type II BBO crystal. The 800 nm pump pulse (3.5 μJ) is tightly focused into the crystal, acting as a spatial filter for the focused seed light which has a larger beam waist and a poor quality mode. Tilting the crystal for optimal phase matching angles produces $\sim$900 nJ of signal and idler after this first stage of amplification. For the second amplification stage the generated

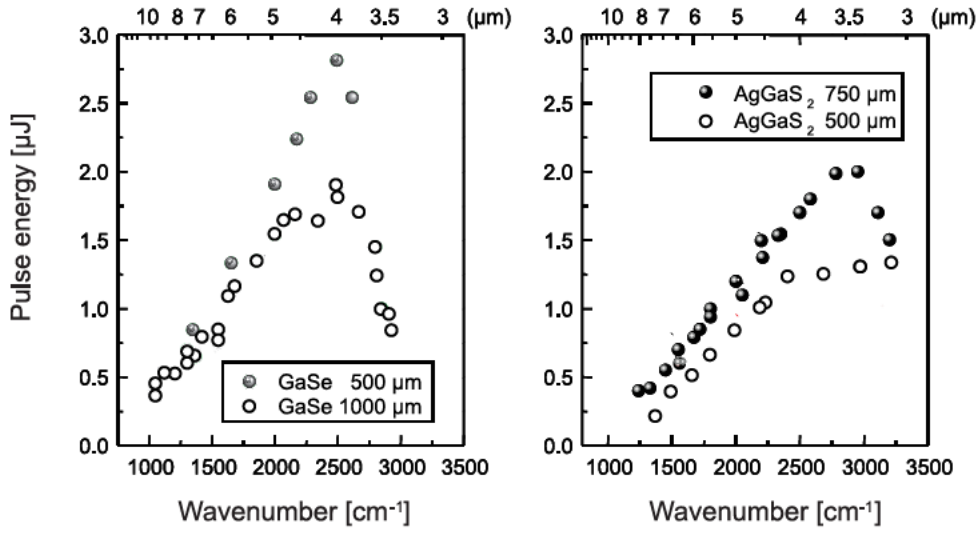

Figure 3.3: Output characteristic of the setup for MIR generation: pulse energy obtained with $AgGaS_2$ and GaSe for different crystal length.

idler pulse is removed by a suitable dichroic mirror (DM2) while the signal light is collimated by a concave mirror (M1, radius $R = 50$ cm) which also serves as a temporal delay for the second pass. The signal pulses are steered back into the same BBO crystal at slightly different height. This simplifies the tuning procedure. The diameter of the major fraction (250 μJ) of the pump light is adjusted to 2-mm by a 1:4 telescope to match the size of the seed and avoid white light generation in the BBO crystal. Pump and signal pulses are overlapped (spatially and temporally) and propagate unfocused through the crystal, generating intense signal and idler pulses, with an energy of $\sim 60 - 70$ μJ across the whole tuning range, corresponding to an energy conversion efficiency of ~25%. The use of type II phase-matching in the OPA entails significant advantages: first, signal and idler polarization are perpendicular and thus correctly aligned for the subsequent difference-frequency process. Second, the OPA can be tuned close to its degeneracy point of 1.6 μm, permitting the generation of small difference frequencies. The signal and idler pulses are continuously tunable from 1.2 to 2.4 μm, with negligible adjustments. Across the entire tuning range, pulse duration of about 80-90 fs (for the signal) were determined by noncollinear autocorrelation in a 100 μm BBO crystal.

The final frequency conversion step takes place in a type I oriented $AgGaS_2$ or GaSe crystal, by DFM. Signal and idler pulses are separated by a broadband dichroic mirror (DM2) and the idler is passed over a variable delay line to adjust the temporal overlap.

Signal and idler are focused by spherical gold mirrors ($R = 1$ m) to a diameter

of about 500 μm into the 1 mm $AgGaS_2$ (or GaSe) crystal where the DFM process takes place. The choice of the nonlinear crystal for the DFM conversion step was made taking into account the following criteria: large transparency at both pump and output wavelengths, high nonlinearity, suitable birefringence for phase-matching, high damage threshold, low two-photon absorption at all interacting wavelengths. The performances obtained with the two crystals were comparable, both in terms of pulse energy and pulse duration. GaSe offers extended tunability towards longer wavelengths (up to 20 μm). As it cannot be polished to appreciable quality, it is currently available only with the surface cleaved along the [001] direction. In GaSe, due to the large incidence angle required to phase-match shorter wavelengths, generation in the 3 μm region resulted in decreased efficiency due to very high Fresnel losses.

Fig. 3.3 shows the pulse energy obtained with $AgGaS_2$ and GaSe for different crystal length as a function of frequency in a range relevant for our experiments. The mid-IR pulses are tunable between 3 and 10 μm with a typical energy of 1-2 μJ per pulse, depending on wavelength. This corresponds to an overall quantum efficiency of about 4%. The temporal duration is of the order of 100 fs over the whole tuning range (FWHM) (see Section 3.4). The set-up described above is used to generate MIR probing pulses for the pump/probe experiments described in this thesis. A detailed analysis of the noise properties of this source can be found in Ref. [69]. It is shown in this work that, under special configuration of the experimental parameters, an unusual low energy fluctuation can be achieved through a *noise suppression mechanism*, stemming from a complicated interplay between saturation and dispersion effects.

3.3.2 Femtosecond ultraviolet pulses

Electronic excitation has been performed using femtosecond pulses in the near-UV generated by sum frequency mixing (SFM) of the Ti:sapphire fundamental and visible pulses generated by a noncollinear optical parametric amplifier [82]. Extending the tuning range to the near ultraviolet is essential for studying the photochemistry of molecules without large conjugated π-electron systems (such as the HBT molecule, see Chapter 4, and the spiropyrans studied in Chapter 6). The design of the set-up is shown in Fig. 3.4.

In this scheme, a fraction (90%) of the fundamental at 795 nm is frequency doubled in a 0.5-mm BBO crystal ($\Theta = 30°$) and then used to pump the visible single-pass noncollinear OPA (NOPA) [83], also based on a BBO crystal (1 mm, $\Theta = 30°$). A smaller part of the fundamental generates a white-light continuum in a 2-mm sapphire crystal. A combination of half-wave plate and a polarizer is used to attenuate the pump pulses to just above the continuum threshold. From the NOPA, broad-bandwidth visible pulses are generated, tunable between 480 and 680 nm. They can be compressed to below 35 fs by means of a pair of prisms.

To generate the tunable near-UV pulses, a third fraction (9%) of the 795 nm

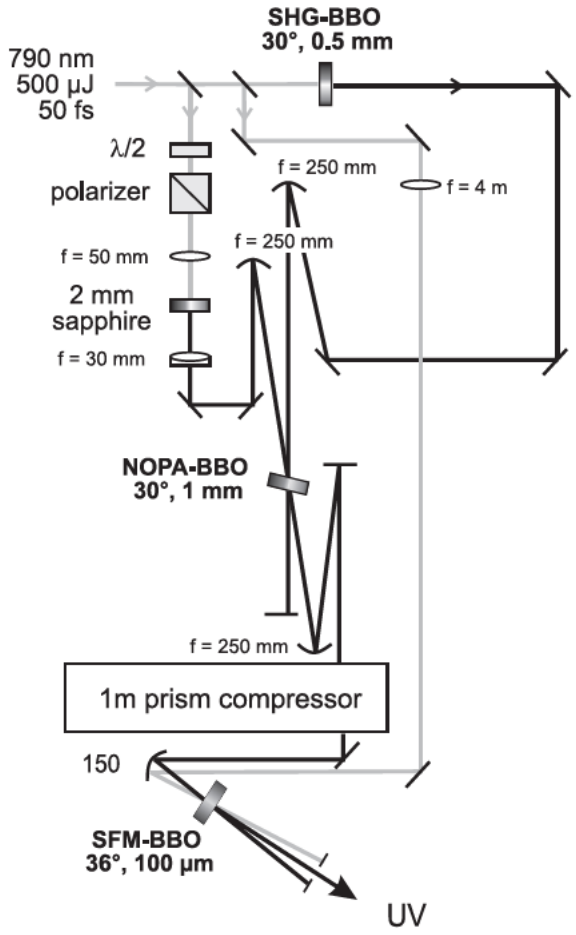

Figure 3.4: Experimental setup for the generation of tunable femtosecond ultraviolet pulses, based on BBO crystals. The non-collinear optical parametric amplifier is followed by sum frequency mixing. (pol: polarizer, $\lambda/2$: half-wave plate). All beam splitters have 10% reflection.

pulses is focused together with the NOPA pulses into a 100-μm-thick BBO crystal ($\Theta = 36°$) for type I noncollinear sum-frequency mixing, with an intersection angle of 1.3°. The tuning range for the pulses generated by sum frequency mixing is shown in Fig. 3.5. Pulse energies above 1 μJ are obtained between 315 and 350 nm, with a shot-to-shot stability of 2.6% (as standard deviation of the average energy). The pulse temporal shape was characterized with self diffraction autocorrelation in a 100-μm-thick BBO crystal. Within the entire tuning range, pulse duration below 40 fs were measured, with a minimum value of 32 fs at 320 nm, at the wavelength corresponding to maximum pulse energy. The pulses at this wavelength are essentially transform limited. Pulse duration is increased in the wings of the tuning range. However, due to the longer pulse duration of the mid-infrared pulses, the UV pulse duration was never the limiting factor in the

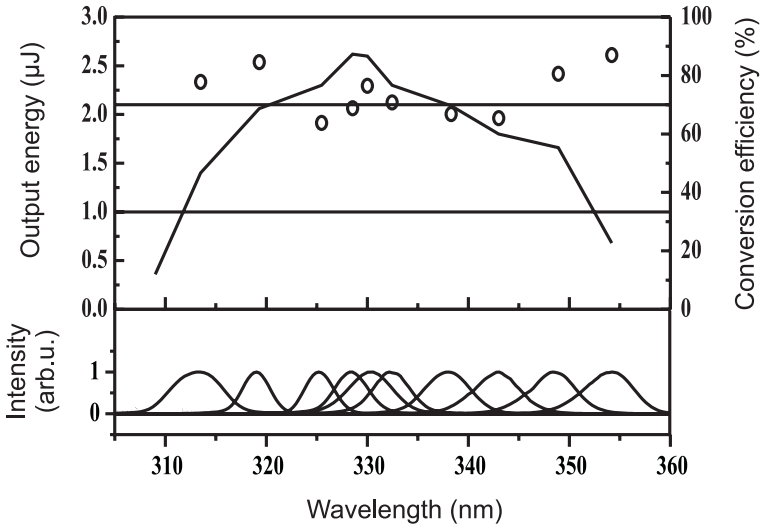

Figure 3.5: Output characteristic of the setup for near-UV generation: (a) output energy (solid line) and conversion efficiency (symbols), defined as the ratio between UV pulse energy and visible pulse energy. (b) UV pulse spectra in the tuning range from 315 nm to 350 nm.

time resolution of the pump-probe experiments.

When excitation at 400 nm was required (see Chapter 5), the second harmonic of the Ti:sapphire fundamental was generated in a 100 μm BBO crystal.

3.4 Pump-probe experiments

Figure 3.6 shows the experimental setup used in the ultraviolet pump/mid-infrared probe experiments. The intense UV pulses trigger the molecular system under study, typically by excitation to the first excited singlet electronic state. The molecular dynamics are then followed by monitoring the evolution of the vibrational spectrum, recording the changes in the intensity of the weak mid-infrared probe pulses as a function of the delay time between pump and probe. To be more precise, the sample generates a third order nonlinear polarization by two interactions with the pump and one with the probe field, radiating a field in the propagation direction of the probe. On the detector, radiated field and probe fields interfere, giving rise to the pump-probe signal.

The output of the BBO OPA with subsequent difference frequency mixing is filtered by a long wave pass filter (LWP) to block residual near-infrared light, ensuring that only mid-infrared light interacts with the sample. The mid-infrared light is re-collimated, and a BaF_2 wedge splits off two weak reflections which are then used as a probe and reference beam. In order to enlarge the beam diameter,

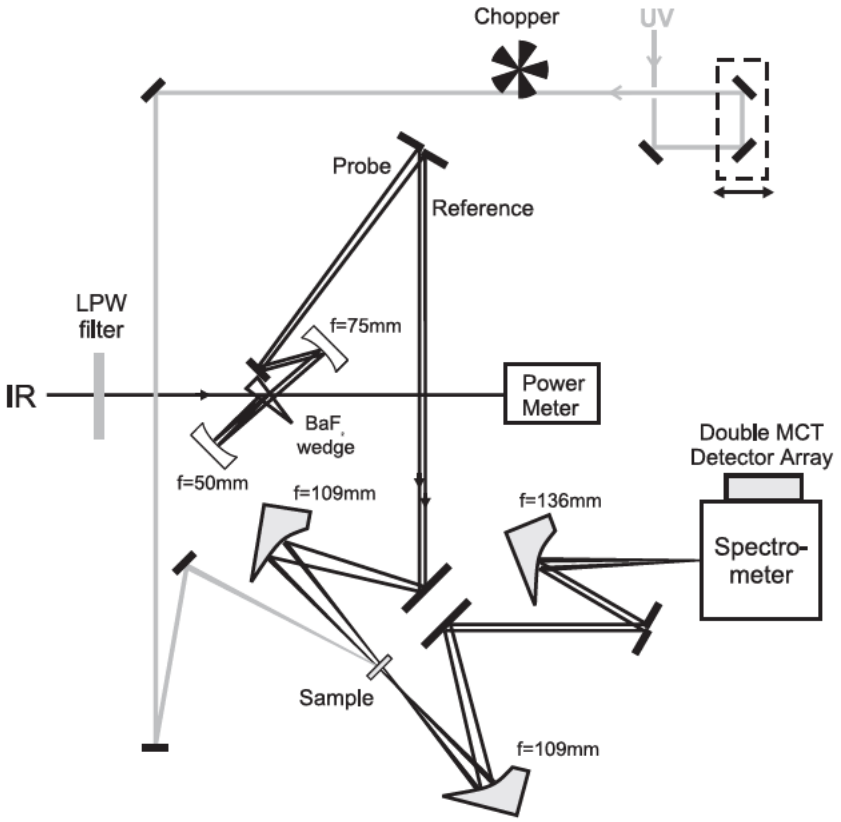

Figure 3.6: Experimental setup for the ultraviolet pump/mid-infrared probe probe experiments. Weak probe and reference pulses are derived as reflections from the front and back side of a thin BaF_2 wedge. The reference pulses pass through a region of the sample which is not excited. Pump and probe overlap in the sample. The spectrally resolved change of absorbance is recorded at the exit of the spectrometer by a double array of MCT detectors as a function of pulse delay between pump and probe .

probe and reference pass through a telescope (2:3). This results ultimately in a reduction of the focal spot size at the sample position (focal diameter: 180 μm). The major part of the mid-infrared light is not actually used in the experiments, since low energies are needed for probing. It is transmitted through the wedge and used to check the infrared pulse energy during the experiments, by means of a power meter. The signal and reference beams are focused by a 30° off-axis parabolic mirror into the sample where pump and probe overlap spatially, whereas the reference passes through a region which is not excited by the pump pulse. The 30° parabolic mirrors (instead of 90°mirrors) are used because of the less critical effect of astigmatism on the focal spot size. The sample is pumped through a free streaming jet of nominal thickness 100 μm. After the sample the light is collimated and the UV pump beam is blocked. Finally, the probe and reference pulses are spectrally dispersed in a grating spectrometer and complete

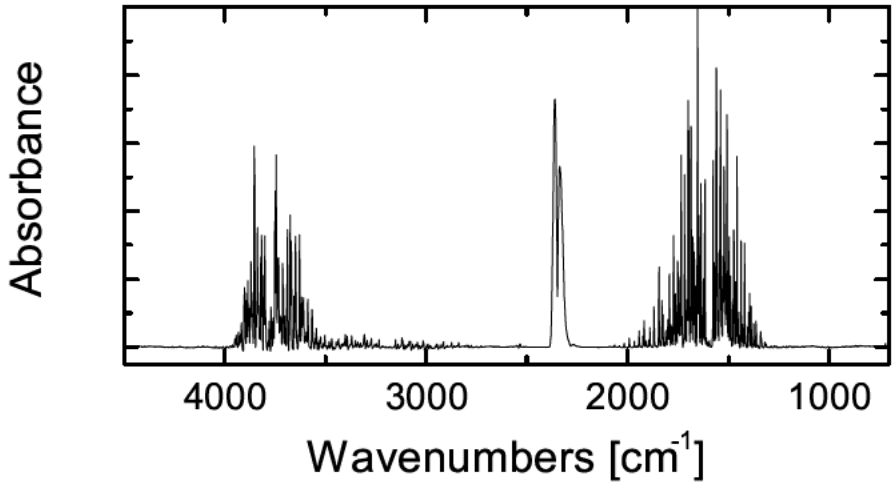

Figure 3.7: The absorption spectrum of air in the mid-infrared spectral range shows three wavelength regions with strong absorption lines of the molecules H_2O and CO_2. Around 3700 cm^{-1} the symmetric and antisymmetric OH stretch in water vapor exhibit a rovibrational fine structure. Around 1600 cm^{-1} the ν_2 bending mode of H_2O displays a similar fine structure. Absorption around 2300 cm^{-1} is due to the strong IR active CO_2 asymmetric stretching vibration. To avoid laser pulse distortion due to propagation in air the setup is placed in a box purged with nitrogen gas.

spectra are recorded simultaneously for each shot using a liquid nitrogen cooled double array (2 × 32 pixels) of MCT (HgCdTe) detectors.

Normalizing on a single shot basis probe and reference signal leads to a significant improvement of the sensitivity. The monochromator was not tuned during measurements to avoid repositioning errors (± 2 cm^{-1}). Synchronous chopping of the UV pump pulses is also used to eliminate long term drift effects, allowing a comparison of the probe intensity with and without pump pulse on two subsequent laser shots. The experimental curves shown in this thesis represent typically an average of 100-200 delay time traces each taking 400 shots per delay step. The pump-probe arrangement described here has the potential to resolve changes in absorbance down to the level of 10^{-4}.

The change of absorbance displayed is then calculated normalizing with respect to the transmission of the reference pulses and comparing on two subsequent shots with the unexcited case:

$$\Delta OD = \log\left[\left(\frac{I_{\text{probe}}}{I_{\text{reference}}}\right)_{\text{pumpon}} \cdot \left(\frac{I_{\text{reference}}}{I_{\text{probe}}}\right)_{\text{pumpoff}}\right] \tag{3.3}$$

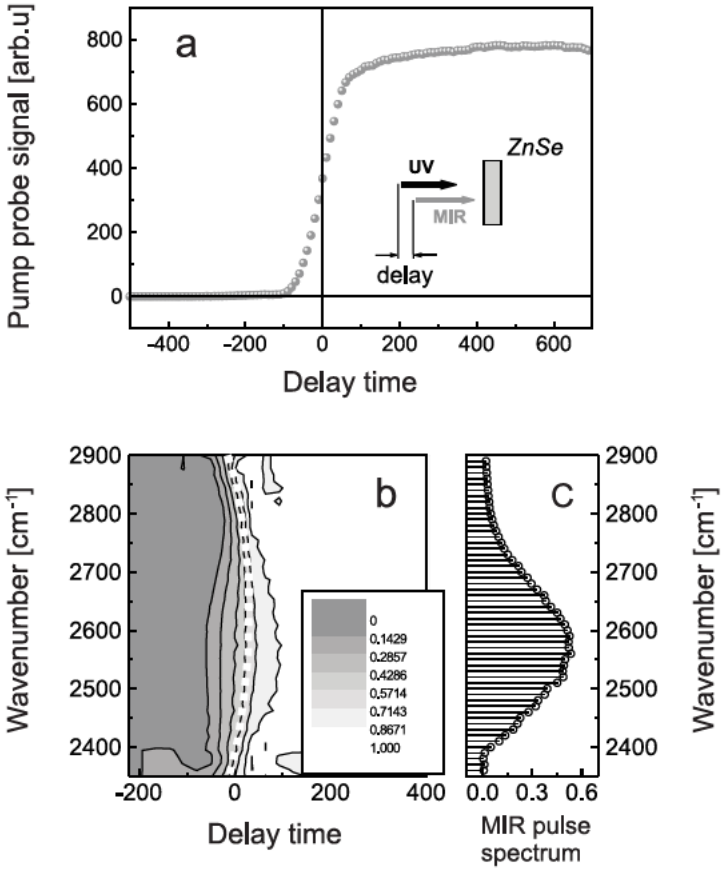

Figure 3.8: Results of a cross correlation experiment in ZnSe for infrared pulses centered at 2580 cm^{-1}. (a) Spectrally integrated pump-probe signal, corresponding to a pulse duration (FWHM) of 120 fs. (b) Spectrally resolved pump probe signal. The white dotted line shows the zero delay at each spectral position, indicating that the pulses possess a moderate quadratic chirp. (c) Spectrum of the MIR pulses.

With the unavoidable exceptions of a bandpass filter and of the BaF_2 wedge which splits off probe and reference, care was taken in using only reflective optics, to avoid distortion of the profiles of the laser pulses due to dispersion or nonlinear effects in the optical elements of the experimental setup. The choice of the material BaF_2 was made taking into account its transparency and dispersion properties in the mid-IR spectral range. In the region between 3 and 5 μm it introduces very little negative group velocity dispersion. At longer wavelengths, materials like Ge or ZnSe would be more appropriate [84]. The use of reflective optics allows accurate prealignment with a semiconductor laser emitting in the visible.

To avoid spectral and temporal distortion of the mid-IR laser pulses due to

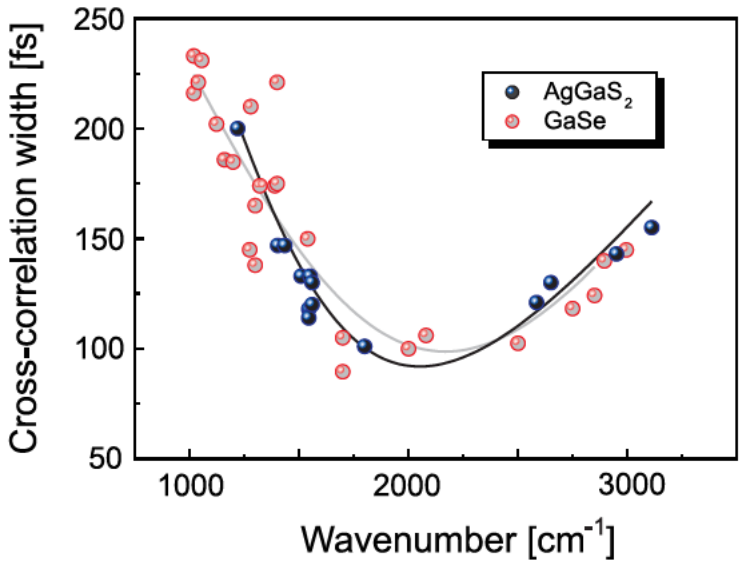

Figure 3.9: Time resolution (FWHM) of the ultraviolet pump/mid-infrared probe experiments as function of the central frequency of the MIR pulses, as determined by cross correlation experiments in ZnSe. For all the experimental points, the pulse duration of the UV pump pulses, as determined by self-diffraction autocorrelation, was below 35 fs (FWHM).

the absorption of water vapor and CO_2 (see Figure 3.7), the whole pump-probe setup is purged with nitrogen gas. Significant pulse distortion of the infrared pulses is expected at frequencies where gaseous components of air have resonant transitions. The absorption spectrum of air in the mid-infrared spectral range shows three wavelength regions with strong absorption lines due to the presence of the molecules H_2O and CO_2: 3700 cm^{-1} (stretching modes of water), 1600 cm^{-1} (bending mode of water), and 2300 cm^{-1} (stretching mode of CO_2). In standard atmospheric air, propagation on distances of the order of several tens of cm produces dramatically distorted pulses, with long trailing wings due to the resonant interaction [85].

For reference purposes the sample is replaced by a polished semiconductor (ZnSe) window to determine the zero delay point (including the chirp of the infrared pulses) and to control the pulse duration. This is made in a spectrally resolved cross correlation measurement, where the absorption of the UV radiation in the semiconductor produces an electron plasma, which then absorbs the mid-infrared pulses. Assuming an instantaneous response of the semiconductor, the measured signal is then proportional to the intensity cross correlation function $G(\tau)$:

$$G(\tau) = \int I_{UV}(t) I_{IR}(t-\tau) \mathrm{d}t \tag{3.4}$$

where I_{UV} has been separately obtained by self diffraction autocorrelation (cf. Section 3.3.2). Figure 3.8 shows a typical result for a cross correlation experiment in ZnSe. The semiconductor was excited by 36 fs pulses at 330 nm, and the MIR pulses were centered at 2580 cm^{-1}. The spectrally integrated pump-probe signal corresponds to a pulse duration (FWHM) of 120 fs. From the spectrally resolved measurement, it is possible, at each spectral position, to extract zero delay and cross-correlation width. The frequency dependent zero delay indicates a quadratic chirp in the infrared pulses. From the data one gets a value for the product $\Delta\nu \cdot \Delta\tau = 0.65$. Fig. 3.9 shows the time resolution (FWHM) of the ultraviolet pump/mid-infrared probe experiments as function of the central frequency of the MIR pulses, as determined by cross correlation with the UV pulses. For all the experimental points, the pulse duration of the UV pump pulses, as determined separately by self-diffraction autocorrelation, was below 35 fs (FWHM). Hence, the duration of the MIR pulses coincides to a good approximation with the width of the cross-correlation.

Another important issue which limits the achievable time resolution in the experiments is the unavoidable group velocity mismatch (GVM) between the UV and mid-IR frequencies, which, in a 100 μm thick sample, leads to a significant temporal walk-off of the pump and probe pulses. In the case of the solvent C_2Cl_4 (tetrachloroethene) for instance, the group velocity mismatch between UV-pump pulses at 330 nm and probing MIR-pulses centered at 1550 cm^{-1} was measured to be 880 fs/mm in the neat solvent, the UV-pulse traveling slower. In order to minimize this effect a relatively high concentration of absorbing molecules has been chosen in the experiments, leading to effective jet thicknesses of less than 30 μm.

Chapter 4

Intramolecular excited state hydrogen transfer

4.1 Introduction

The structure and the structural dynamics of many important molecular systems (e.g. protic solvents such as water, biomolecular polymers such as proteins and DNA) are largely determined by the special properties of hydrogen bonds. The molecular function of such systems often involves the transfer of hydrogen atoms or protons along pre-existing hydrogen bonds. In the most elementary case, the hydrogen transfer reaction consists in the shift of an hydrogen atom H, initially part of a covalent bond A-H, to a new binding site B:

$$\mathrm{A\quad H\cdots B\ \rightarrow\ A\cdots H\quad B}$$

where A and B can be two groups of the same molecule (*intramolecular* transfer) or belong to neighboring molecules (*intermolecular* transfer).

Proton exchange along hydrogen bonds occurs frequently in hydrogen bonded networks such as water (proton hops, Grotthuss mechanism) [86–88]. Proton pumps through membranes also operate by proton transfer along “water wires" to maintain a certain pH gradient along membranes, e.g. in the case of photosynthetic reaction centres [89]. Dynamics of hydrogen bonds occur on ultrafast time scales, mainly set by motions of the hydrogen donor and acceptor groups, both in thermal equilibrium and for non-equilibrium excitations. In thermal equilibrium, i.e. in the electronic ground state, vibrational and translational motions of the nuclei comprising the hydrogen bonded system cause fluctuations in the geometrical parameters of the hydrogen bond, leading to a breaking and reformation of hydrogen bonds and - in some cases - to proton transfer. In addition, fluctuating solvent configurations may alter the relative energies of the donor and acceptor moieties of the hydrogen bonded complex, thereby stabilising or de-stabilising the newly formed configuration after proton transfer [90,91]. Proton/hydrogen trans-

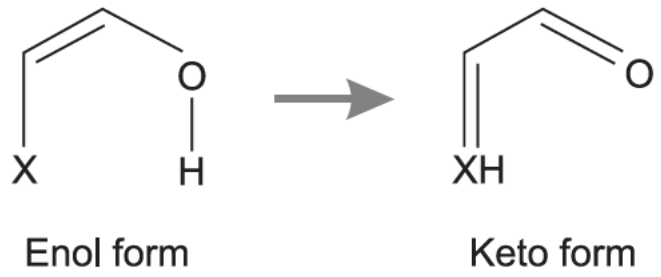

Figure 4.1: A typical intramolecular proton transfer reaction where an initial enol form experiences a structural isomerization leading to the keto form.

fer processes can also occur after photoexcitation to a higher electronic state. The work described in this thesis deals with this latter class of photoinduced transfer processes. In this Chapter, an experimental study of *intramolecular* transfer is reported, whereas the following Chapter 5 is devoted to the case of *intermolecular* transfer.

The excited-state intramolecular hydrogen transfer (ESIHT) process is an interesting model system for studying basic microscopic reaction mechanisms and - thus - it is one of the most thoroughly studied photoinduced reactions [92]. The study of ESIHT system by means of spectroscopic techniques has been pioneered by Weller, who for the first time ascribed the large red-shift of the fluorescence of protonated salicylic acid and methyl salicylate to the intramolecular transfer of a proton [93,94]. Weller interpreted the hydrogen transfer reaction in terms of photoinduced changes of acidity and basicity of the relevant molecular groups. Since then, the large Stokes shift of the fluorescence of numerous compounds has been explained in terms of a photoinduced reaction involving an intramolecular hydrogen transfer [95,96]. In a large variety of aromatic molecules with intramolecular hydrogen bonds, a typical intramolecular hydrogen transfer reaction takes the form of a enol-keto tautomerization reaction (Fig. 4.1 and Fig. 4.2). Fig. 4.2 shows the structure of several important molecular systems exhibiting ESIHT. In the ground state, in nonpolar solvent, these compounds are predominantly in their enol-tautomeric form. The ESIHT reaction consists in a structural isomerization after which the keto-tautomer is formed. The acronym ESIHT instead of the widely used ESIPT (excited state intramolecular proton transfer) should be preferred, since the existing calculation of the electronic wavefunctions have shown that this reaction is more properly described as the transfer of a neutral hydrogen atom [97], and not of a proton, in contrast to the early assumptions of Weller [93,94]. In some cases, proton and hydrogen transfer can be distinct and

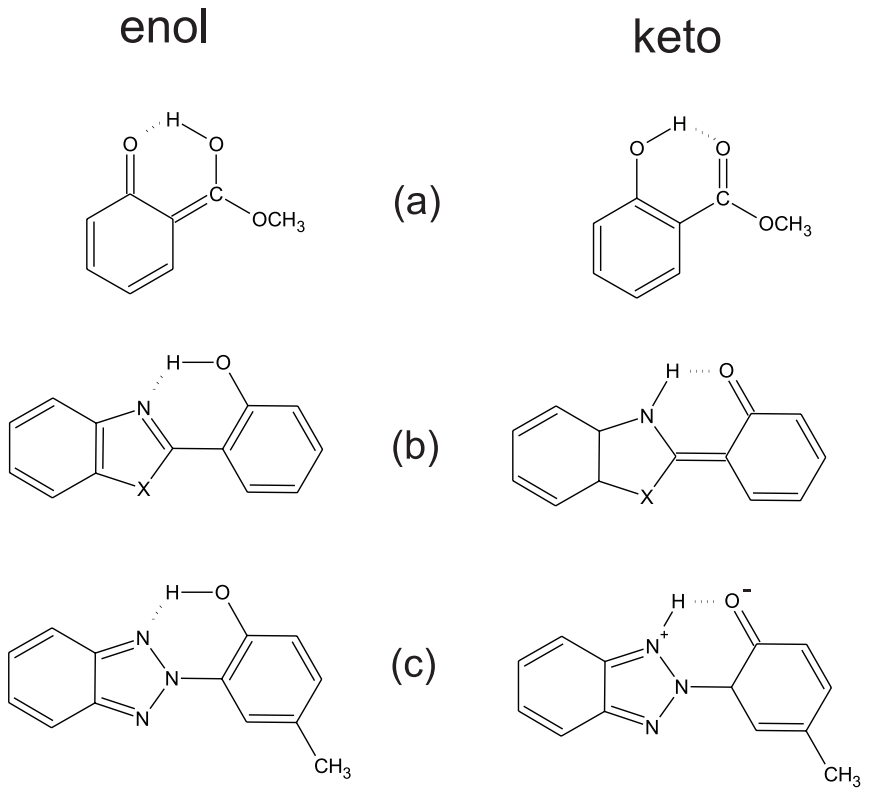

Figure 4.2: Molecular structures of the enol- (left) and keto-type (right) tautomers of (a) methyl salicylate (MC) (b) X=S: 2-(2'-hydroxyphenyl) benzothiazole (HBT), X=O: 2-(2'-hydroxyphenyl) benzoxazole (HBO) (c) 2-(2'-hydroxy-5'-methylphenyl) benzotriazole (TIN). The enol tautomer is the initial ground state species in nonpolar solvents, the keto tautomer results from intramolecular hydrogen transfer.

competing processes [97].

Molecular systems exhibiting ESIHT have been proposed as laser dyes [98], fluorescence probes of biomolecules [99] and found their most important application as UV absorbing additives in polymers and cosmetics [100, 101], where their photochemical stability is exploited. This property, e.g. in molecules of the families of hydroxy-benzophenones and hydroxyphenyl-benzotriazoles, is assumed to derive from an ultrafast internal conversion IC process which quickly deactivates the fluorescing electronic state. The IC rates are enhanced by the reduction of the energy gap due to the ESIHT reaction. The ultrafast IC process is essential to avoid the population of photochemically reactive triplet states [96].

The dynamics of the hydrogen transfer process depend critically on the shape of the potential energy surface on which the transfer proceeds. In the case of hydrogen transfer from metastable triplet states, time scales in the microsecond range have been reported [102, 103] and interpreted in terms of a hydrogen trans-

fer mechanism involving tunnelling through a potential barrier. As soon as picosecond time-resolution was achieved in spectroscopy, studies of the much faster hydrogen transfer dynamics in excited singlet states have been reported [104–107]. These first picosecond studies have been carried out in the optical domain, using electronic transitions to study the reaction dynamics through the rise and decay of fluorescence or stimulated emission from the product species. In most cases, such studies have not been able to resolve the formation of the product species, which appeared within time resolution (as determined by the resolution of a streak camera or by the pulse duration in pump-probe experiments). Even at cryogenic temperatures (4 K) rate constants for the ESIHT reaction were too large to be measured [105, 106]. The relaxation processes following the sub-picosecond reaction (vibrational energy redistribution, cooling, radiatonless decay ...) were also addressed by these picosecond studies [106].

The first direct proof of the ultrafast appearance of the keto geometry following electronic excitation was obtained by picosecond ultraviolet pump/mid-infrared probe experiments in which the reaction was observed by monitoring the changes of vibrational spectra upon electronic excitation [108, 109], giving site-specific insight into the local changes of molecular geometry due to the ESIHT reaction. The evidence of the formation of the keto tautomer of the HBT molecule within 5 ps after electronic excitation of the enol species was given by detecting the formation of high frequency N-H, C=O stretching vibrations which mark the keto tautomer.

In order to resolve the formation of the final species, femtosecond time resolution is needed. The first experiment capable to follow the reaction dynamics leading to the formation of the keto tautomeric form has been done by means of a UV pump visible probe measurement on the HBT system, with a time resolution of 100 fs [110], where a rise-time of 170 fs of the long-wavelength part of the keto-stimulated emission spectrum has been detected. Several ESIHT systems have been since then investigated by this technique and rise times of the emission of the product species between tens and few hundreds of femtoseconds have been reported [111–118], pointing at transfer mechanisms along a molecular coordinate without a significant potential barrier between the initial and the final molecular structures. Experimental studies addressing the effect of deuteration [115] and the dependence of the reaction dynamics on the excitation wavelength [119] as well as ab initio calculation [97] have confirmed this picture for several representative ESIHT systems. This raises the question whether the excited state reaction is a transition between well defined enol and keto excited states or rather an intrastate relaxation process connected with a change of the nuclear configuration.

Despite extensive research, both theoretical and experimental, many fundamental aspects of the ESIHT mechanism are not fully clarified and a full microscopic understanding of the hydrogen transfer reaction has not yet been developed [92]. A number of crucial, partially unresolved questions can be pointed out here: Which vibrational degrees of freedom play a role in the hydrogen transfer,

in other words, which modes define the reaction coordinate? Are these modes elongated directly by the electronic excitation, or after propagation in the excited state? In many ESIHT systems, the range of the excited state potential populated by the excitation on the enol S_0-S_1 transition has an excess energy of about 3000 cm^{-1} with respect to the keto-S_1-state minimum. This excess energy is redistributed within the vibrational manifold during and after hydrogen transfer and a stable keto product species is formed. So far, the time scales and pathways of this redistribution process which may play a key role for the irreversible character of hydrogen transfer, are not understood. Which vibrational modes accept the excess energy? In particular, to which extent the excess energy is accepted by high frequency stretching vibrations of the modes whose atoms are directly involved in the proton transfer (carbonyl, N-H groups)? Femtosecond excitation creates vibrational wavepackets in those modes which couple strongly to the enol-S_0 $\rightarrow$ enol-S_1 transition: before the loss of coherence due to relaxation and dephasing processes, the initial dynamics of hydrogen transfer will be a coherent propagation along different vibrational coordinates. How fast is the wavepacket spread? How is the final keto species stabilized against the back reaction?

Femtosecond vibrational spectroscopy represents the most direct way of monitoring, in a site specific fashion, the hydrogen transfer reaction dynamics as well as the following relaxation processes induced by the H transfer.

4.2 2-(2'-hydroxyphenyl)benzothiazole (HBT)

The ESIHT reaction was studied in the model system 2-(2'-hydroxyphenyl) benzothiazole (HBT, see Fig. 4.3). In HBT, after excitation to the enol-S_1-state, a

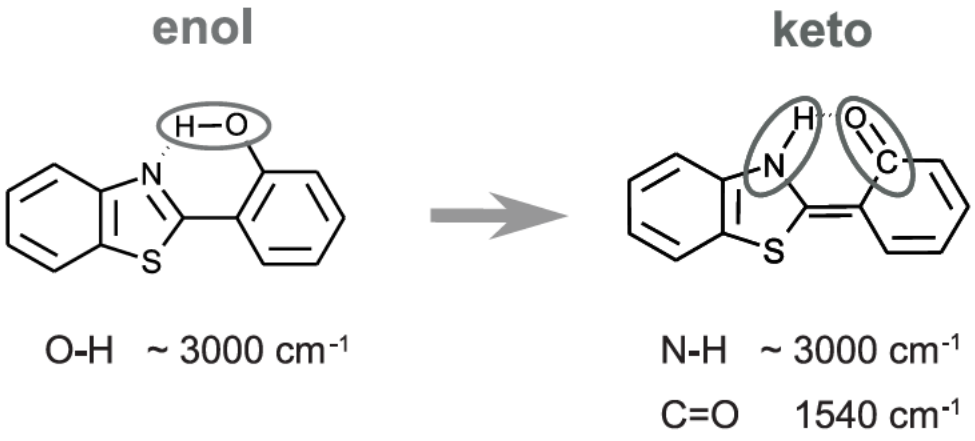

Figure 4.3: Molecular structures of HBT in the enol and keto-tautomer configurations and most relevant stretching vibrations. The hydrogen transfer reaction occurs after electronic excitation to the enol-S_1-state.

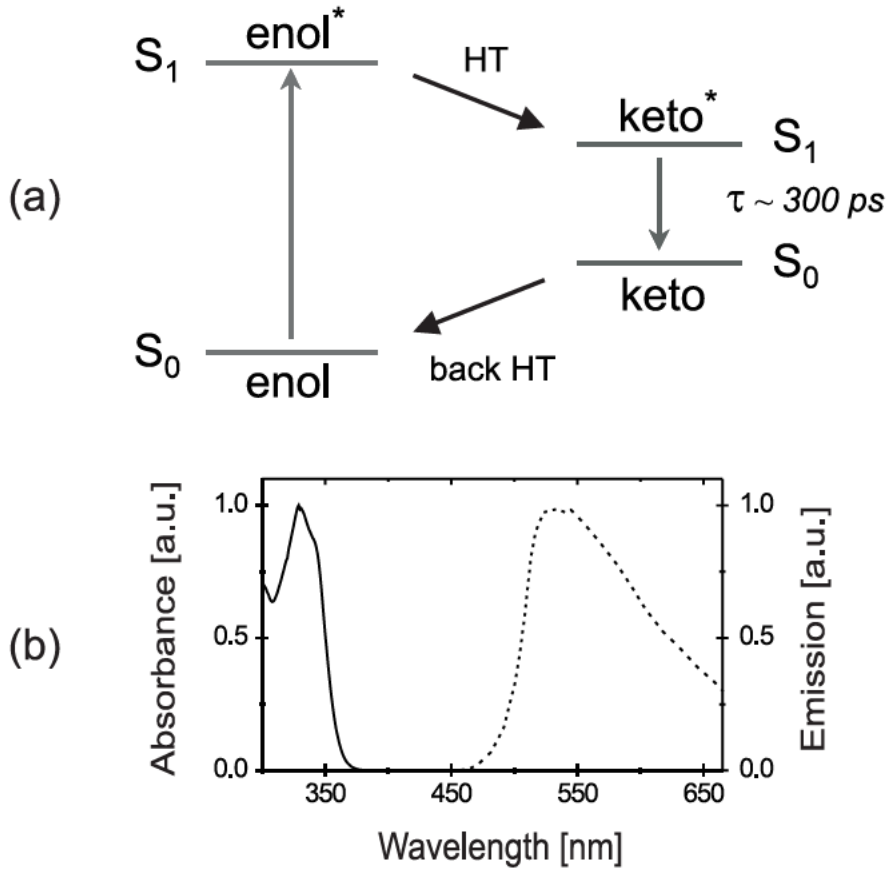

Figure 4.4: (a) Reversible cycle triggered by excitation of the enol form of HBT to the enol-S_1-state. The keto-S_1-state decays on subnanosecond time scales to the keto-S_0 state by photo-emission. HBT relaxes then to the enol-S_0 state by back hydrogen transfer (back HT). (b) The optical spectra show the large Stokes-shift between absorption and emission bands that typifies the excited state hydrogen transfer reaction.

reversible cycle is initiated, where on an ultrafast time scale the keto-S_1 product is formed in its first excited state (see Fig. 4.4). Whereas in similar molecular systems, such as e.g. in 2-(2'-hydroxy-5'-methylphenyl) benzotriazole (TIN [111]), internal conversion depopulates the excited product state on a subpicosecond timescale, this is not the case for HBT, where the keto-S_1 state is long lived, with a lifetime on the order of 300 ps. On longer time scales the fully reversible reaction cycle is completed with the hydrogen back transfer in the enol ground state.

Already 15 years ago it was shown with picosecond infrared spectroscopy that a clear signature of the appearance of the keto-S_1-state nuclear configuration of HBT is the mid-infrared (MIR) absorption band around 1540 cm^{-1}, corresponding to the C=O double bond stretching mode [109]. Measurements around 3000

cm^{-1} supported the evidence of the enol → keto isomerization showing the disappearance of the O-H stretch marking the enol state and the formation after the reaction of a N-H streching vibration (see Fig. 4.3). In such measurements, the transfer reaction was not temporally resolved.

The first femtosecond study of intramolecular hydrogen transfer was performed on the HBT molecule: Femtosecond pump-probe studies of stimulated emission in the red part of the keto S_1-S_0 emission spectrum gave a rise time 170 fs for the emission which was attributed to hydrogen transfer [110]. Very recently, this process in HBT has been studied with a substantially improved time resolution of 30 fs and over a spectral range covering the full keto*-emission band [120,121]. At short wavelengths, emission rise times of about 60 fs were found whereas a substantially slower rise was detected at long wavelengths, in quantitative agreement with the data of Laermer et al. [110]. The delayed onset of stimulated emission was described as consequence of a ballistic evolvement of the nuclear configuration, leading to sudden, delayed population of the keto-S_1-state of HBT. The 60 fs delay of the keto*-stimulated emission at short wavelengths was assigned to the hydrogen transfer time.

The most recent experiments with a time resolution of about 20 fs allow for the observation of vibrational coherences occurring during and after excited state hydrogen transfer. This has been demonstrated for the first time for 2-(2'-hydroxy-5'-methylphenyl)benzotriazole where two low-frequency modes at 299 and 470 cm^{-1} are elongated upon electronic excitation and give rise to oscillatory features in the rise of product emission [122]. An analysis of the microscopic motions connected with such modes that was based on resonance Raman studies and theoretical calculations [123], led to a qualitative microscopic picture of hydrogen transfer in which motions along low-frequency modes determine the pathway of the reaction on the excited state potential energy surface. HBT displays similar features: superimposed on the incoherent (rate-like) kinetics are pronounced oscillations with frequency components of 118, 254, 289, and 529 cm^{-1} [120, 124]. Such oscillations persist for 2 to 3 ps and reflect coherent wavepacket motions along several Raman-active low-frequency modes which couple strongly to the enol S_0-S_1 transition and are elongated upon electronic excitation. Based on such findings and theoretical ab initio calculations of potential energy surfaces, microscopic pictures for 'barrierless' hydrogen transfer have been developed in which coherent motions along one or several low-frequency modes promote the reaction. It should be noted, however, that such modes are strongly elongated upon excitation of the enol-S_1-state, as they couple strongly to the electronic transition.

The study of electronic spectra does not allow for a direct characterization of transient molecular structures during and after the reaction. Besides, the spectrally dependent rise time of the keto* state stimulated emission does not allow an unambiguous determination of the ultrafast reaction rate. Here, ultrafast vibrational spectroscopy monitoring local changes of molecular geometries provides

direct site-specific access to molecular structure and nuclear motions. The work reported in this chapter has given insights into several aspects of the ESIHT reaction in HBT, concerning the dynamics of the formation of the keto species, the observation of coherence phenomena in the photoinduced chemical reaction and the processes of redistribution and dissipation of the excess energy released upon hydrogen transfer.

4.3 Experimental results

HBT was dissolved in C_2Cl_4 and pumped through the 100 μm-thick free streaming jet. In the experiments the excitation wavelength was tuned from 315 nm to 350 nm, corresponding to the transition to the first singlet state S_1 of HBT. The excitation pulse energy was 2-4 μJ and the pulse duration around 40 fs. The pump pulses excited about 10% of the HBT molecules in a sample volume of 180 μm diameter. The group velocity mismatch between UV-pump pulse and the MIR-pulses was measured to be 880 fs/mm in the neat solvent, the UV-pulse traveling slower. In order to minimize the effect of temporal walk-off between the pulses a relatively high concentration of 4 g/l was chosen leading to an effective jet thickness of less than 30 μm. Nevertheless the high extinction of the UV pulse did not lead to substantial temporal reshaping, since excitation was performed around the peak of the broad absorption band, leading to spectrally uniform attenuation. The probing mid-infrared pulses were tuned between 1000 and 1700 cm^{-1} and detected with a spectral resolution of 4 cm^{-1}. The pump-probe set-up was purged with nitrogen gas to avoid spectral and temporal reshaping of the mid-infrared pulses due to water and CO_2 absorption. Measurements in the neat solvent were performed under the same experimental conditions. Experimental curves shown here represent an average of 100-200 delay time traces each taking 100 shots average per delay step.

The present study concentrates on the fingerprint region of the vibrational spectrum from 1000 to 1700 cm^{-1}. The spectral region at 3000 cm^{-1} of the O-H stretching band of the enol-form and the N-H spectral region of the keto*-form was also inspected. However, the broad O-H and N-H stretching bands overlap significantly with implicit complications in the interpretation of the experimental data. Hence, the discussion focuses here on the results obtained in the fingerprint region. The structure and the vibrational spectra of HBT in the enol ground state were calculated using the B3LYP/6-31G(d) level of theory implemented in Gaussian98 [126]. The calculated bands are listed in Table 4.1, Fig. 4.5 shows a comparison of the calculated and the measured infrared spectrum of HBT in C_2Cl_4. The very good agreement allows for the assignment of essentially all the lines. The following bands are relevant in terms of hydrogen transfer forming the keto tautomer: ν(phOH-19b) + ν(C-O) + d(OH) + ν(C=N) = 1483 cm^{-1}, ν(phBT-19a) + ν(phOH-19a) + ν(C=N) + δ(OH) + ν(C-O) = 1460 cm^{-1},

Experimental	Calculation	Assignment*
1624	1622	ν(phOH-8a) + δ(OH)
	1593	ν(phBT-8a)
1588	1581	ν(phOH-8b) + δ(OH)
1561	1553	ν(phBT-8b)
1504	-	
1492	1508	ν(C=N) + δ(OH)
1483	1488	ν(phOH-19b) + ν(C–O) + δ(OH) + ν(C=N)
1460	1456	ν(phBT-19a) + ν(phOH-19a) + ν(C=N) + δ(OH) + ν(C–O)
	1448	ν(phBT-19a) – ν(phOH-19a) + ν(C=N) + δ(OH) + ν(C–O)
1441	1433	ν(phBT-19b) + ν(C=N)
1406	1412	δ(phOH: CH-3) + δ(OH)
1318	1323 +	ν(phOH-14) + ν(C–O)
	1318	ν(phBT-14)
1272	1275	ν(C–O, 13)
1254	1250	δ(phBT: CH-3)
1242	1234	δ(phBT: CH-9a) + ν(phBT–N)
1217	1205	δ(OH) + ν(phOH–CS=N)
1155	1151	δ(phOH: CH-9a)
1128	1117	δ(phBT: CH-18a)
1122	1112	δ(phOH: CH-18a)
1071	1047	δ(phOH-12) + ν(phBT–S)
1035	1029	δ(phOH: CH-18b) + ν(phOH-1)
1017	1007	δ(phBT: CH-18b) + ν(phBT-1)

Table 4.1: Experimental (in C_2Cl_4) and calculated (B3LYP/6-31G(d), scaled by 0.965) infrared bands for HBT in the enol ground state in the fingerprint region (in cm^{-1}).

*Varsanyi nomenclature [125], ν = stretching mode, δ = in-plane deformation mode, phOH = phenol ring, phBZ = benzene ring in the benzothiazole fragment.

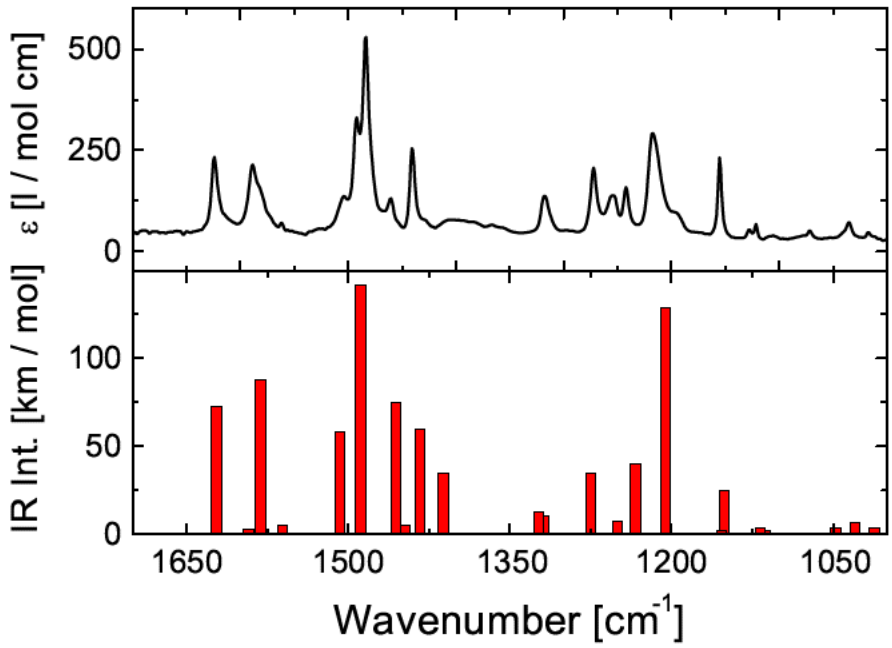

Figure 4.5: Ground state absorption spectrum of HBT in C_2Cl_4 compared with results of B3LYP/ 6-31G(d) calculations in the fingerprint region. The calculated lines are listed in Table 4.1.

δ(phOH: CH-3) + δ(OH) = 1406 cm^{-1}, ν(phOH-14) + ν(C-O) = 1318 cm^{-1} and ν(C-O, 13) = 1272 cm^{-1}.

Fig. 4.6a shows transient infrared spectra of HBT recorded at different time delays between the pump pulses at 330 nm and the infrared probe pulses. The measured change of absorbance $\Delta A(\nu) = -log[T(\nu) - T_0(\nu)]/T_0(\nu)$ is plotted as a function of probe frequency, where $T(\nu)$ and $T_0(\nu)$ are the infrared transmissions of the sample with and without excitation, respectively. Fig. 4.6b shows $\Delta A(\nu)$ between 1350 and 1580 cm^{-1} on an extended scale. The negative contributions to $\Delta A(\nu)$ originate from the bleaching of ground state modes upon ultraviolet excitation. Such bleaching signals occur already at negative time delays, as is evident from time-resolved measurements at a fixed probe frequency (Fig. 4.7a). The absorbance change at negative delay times is due to the perturbed free induction decay (PFID) of the coherent polarization created on the vibrational transition by the probe and disturbed at later times by the pump pulse (see Chapter 2, Section 2.3). At positive delays, the bleaching signals are nearly constant for tens of picoseconds. Around delay zero a peak is observed at all probe frequencies; separate experiments performed in the neat solvent have

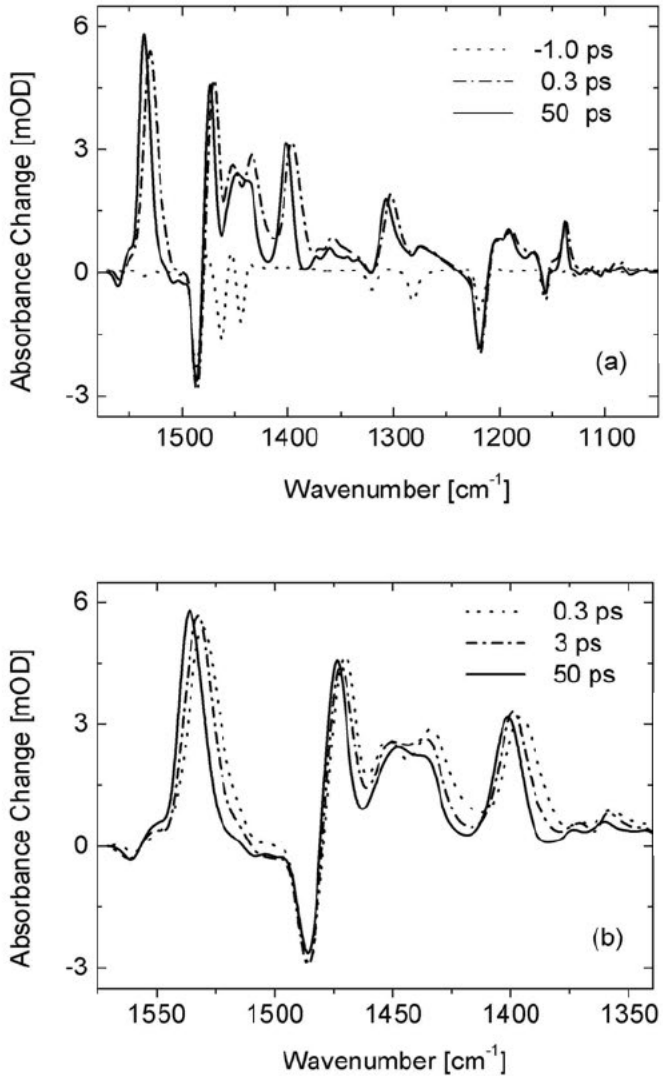

Figure 4.6: (a) Transient infrared spectra of HBT measured at delay times of -1 ps (dotted line), 300 fs (dash-dotted line) and 50 ps (solid line) after electronic excitation. The change of infrared absorbance $\Delta A(\nu) = -log[T(\nu) - T_0(\nu)]/T_0(\nu)$ is plotted as a function of infrared probe frequency ($T(\nu)$, $T_0(\nu)$: transmission with and without excitation). (b) Transient spectra measured 300 fs (dotted line), 3 ps (dash-dotted line), and 50 ps (solid line) after electronic excitation on an extended frequency scale from 1350-1550 cm^{-1}.

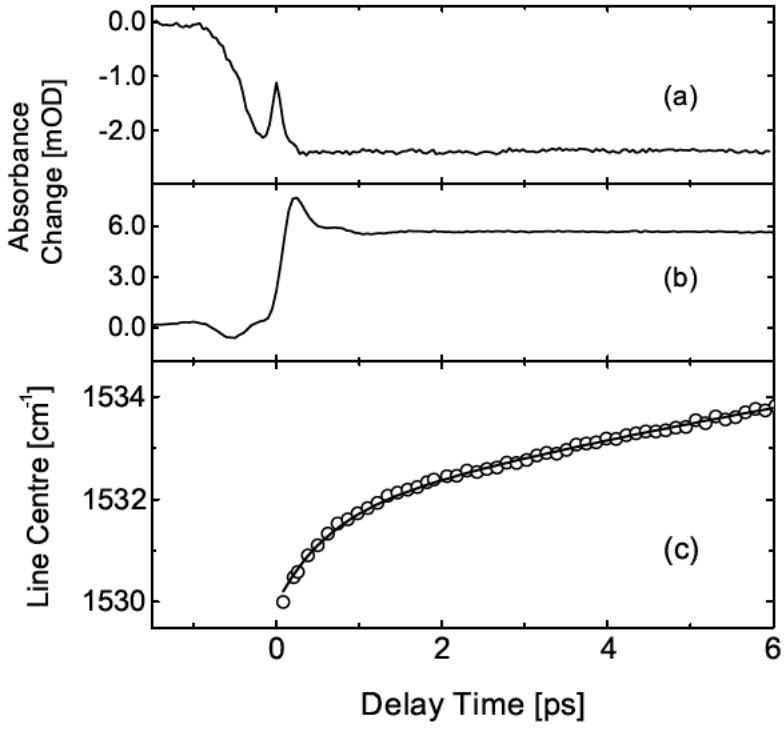

Figure 4.7: Temporal evolution of the absorption changes at fixed spectral positions of (a) 1483 cm^{-1} (bleaching of a ground state vibration) and (b) 1530 cm^{-1} (formation of the carbonyl stretching vibration) as a function of the time delay between pump and probe. (c) Line centre of the C=O band as a function of time delay (symbols) and biexponential fit (solid line) with the following time constants and relative amplitudes: $\tau_1 = 610 \pm 80$ fs, $A_1 = 0.28$, $\tau_2 = 14.5 \pm 1$ ps, $A_2 = 0.72$.

proved that this peak is essentially due to the nonlinear response of C_2Cl_4. The positive signals in Fig. 4.6 represent the vibrational spectrum of the keto S_1 state. The band at 1530 cm^{-1} is caused by the C=O stretching absorption of the keto tautomer. With respect to a free C=O vibration, the frequency is lower because the carbonyl group is part of a hydrogen bond and conjugated to a C=C bond [127]. In Fig. 4.7b, the absorption change at this spectral position is plotted up to picosecond delay times. Fig. 4.8 shows in detail the features of the experimental results obtained when probing in the spectral region between 1400 and 1600 cm^{-1}, around the position where the C=O stretch appears. In this case the UV excitation pulse was tuned at 335 nm. Fig. 4.8a shows transient infrared spectra recorded between 1410 and 1590 cm^{-1}. As a comparison, the infrared spectrum of the enol ground state is plotted in Fig. 4.8b. The PFID contribu-

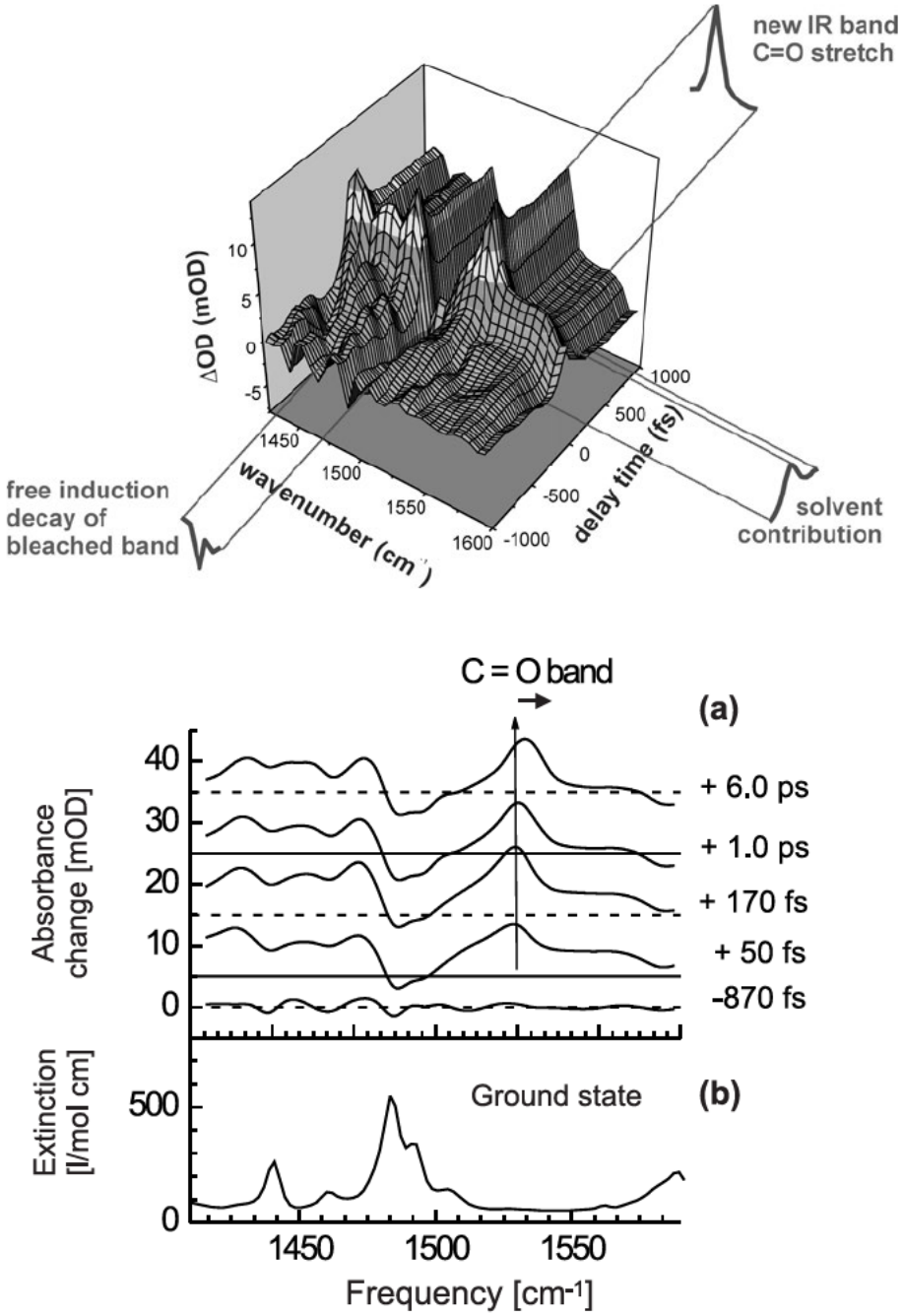

Figure 4.8: Three-dimensional plot of the spectrally and time-resolved pump-probe signals of HBT in the C=O stretch spectral region (upper graph). The data show typically perturbed free induction decay contributions at negative delays, solvent-signals around zero delay, and bleaches and induced absorptions of transient vibrational bands at positive delays. Transient spectra at several pulse delays are shown in the lower graph (a), indicating the rapid rise of the C=O stretching band and subsequent up-shifting at picosecond time scales. As a comparison the ground state infrared spectrum of HBT is shown in (b).

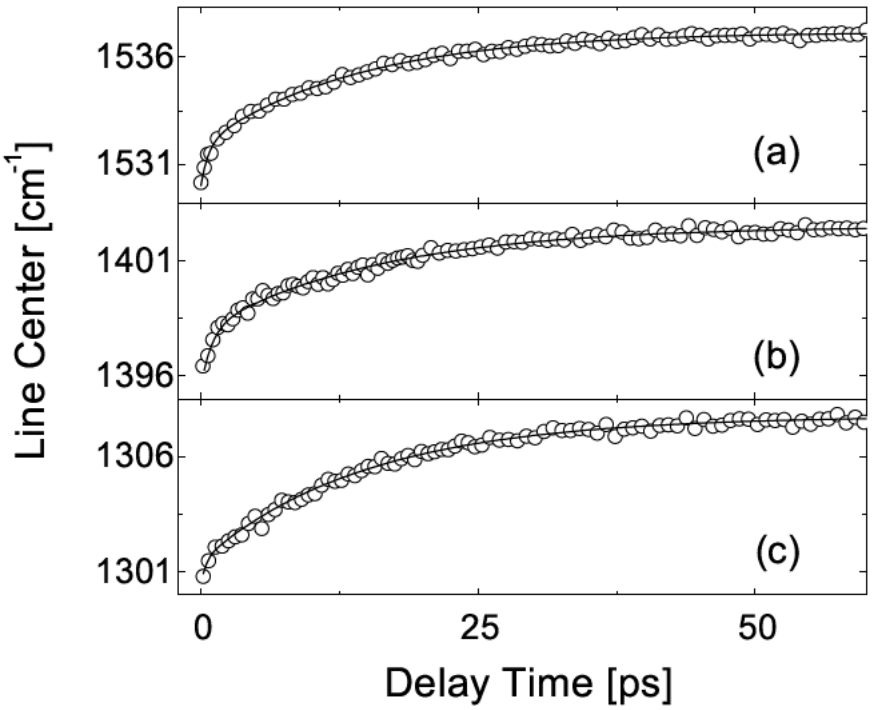

Figure 4.9: Long time behavior of the line centers (symbols) of the transient bands at (a) 1530, (b) 1396, and (c) 1301 cm^{-1} as a function of time delay. The data follow bi-exponential kinetics (solid lines) with the following time constants ti and relative amplitudes A_i (i=1,2): (a) $\tau_1 = 610 \pm 80$ fs, $A_1 = 0.28, \tau_2 = 14.5 \pm 1$ ps, $A_2 = 0.72$, (b) $\tau_1 = 750 \pm 80$ fs, $A_1 = 0.35, \tau_2 = 15.6 \pm 0.9$ ps, $A_2 = 0.65$, (c) $\tau_1 = 590 \pm 100$ fs, $A_1 = 0.13, \tau_2 = 14.9 \pm 1.1$ ps, $A_2 = 0.87$.

tions at negative delay times are evident at those frequencies where ground state bands are located. The solvent contribution around zero delay manifest itself as an overshoot of 1-2 mOD which is constant at all frequencies.

Apart from a slight broadening by 2-3 cm^{-1} at early delay times, the spectral envelopes of all the new bands in the fingerprint region are time-independent. However, they occur initially at spectral positions which are 5-7 cm^{-1} down-shifted from the positions reached after 50-60 ps. To quantify such spectral shifts, Gaussian envelopes were fitted to the different measured bands and the line centres determined in this way are plotted as a function of delay time (Figs. 4.7c, 4.9). The blue-shift of all bands displays nonexponential kinetics with a fast subpicosecond component followed by slower kinetics. The observed time traces are well accounted for by fitting bi-exponential kinetics to the data with time

constants of 600-750 fs and 15 ps.

4.4 Discussion

Our experiments allow to discuss several issues of the ESIHT reaction in HBT, concerning the dynamics of the formation of the keto tautomer, the observation of coherence phenomena due to the anharmonic coupling of the C=O stretch to low frequency vibrations, and the processes of redistribution and dissipation of energy.

4.4.1 Ultrafast formation of the keto tautomer

The dynamics of the enol* → keto* photoinduced tautomerization have been studied in a site specific way by time resolving the appearance of the C=O stretching mode marking the product state. An additional, direct evidence of the formation of the keto geometry is the bleaching of several vibrations, which, according to the calculations (see previous Section, Table 4.1), possess some C-O single bond character. The C-O bond disappears upon formation of the C=O double bond in the keto tautomer.

The prominent new band formed at 1530 cm^{-1} represents the C=O stretching band of the keto*-species. Strength and spectral position of this band agree with earlier picosecond measurements [109]. The new C=O band builds up with a delay of 30-50 fs (Fig. 4.10a), representing the formation time of keto*-HBT. The delay was estimated by comparison with a cross-correlation experiment in ZnSe, with the assumption of an instantaneous response by the semiconductor. Gaussian fitting of the C=O band was performed in order to derive the temporal development of the strength, width and line centre, of which results for excitation at 335 nm are shown in Fig. 4.11. The strength and width of the C=O band do not change at longer delay times. Following the discussion in Section 2.4 of Chapter 2, one can deduce that the C=O mode is populated in its $v = 0$ state, since a feeding of the $v = 1$ state would lead to a spectral reshaping of the band with time. For the C=O stretching mode the anharmonic shift is estimated to be around 15-20 cm^{-1} [30]. Taken into account this anharmonicity, changes in absorbance due to the decay $v = 1 \rightarrow v = 0$ state by population relaxation would have been easily detectable (see Chapter 2, Figs. 2.4 and 2.5) given the experimental time resolution. As a matter of fact, the observed spectral width of the C=O stretching band, directly after generation of the keto*-state, is 12.5 ± 0.5 cm^{-1}. Such a value indicates that even for the extreme case of a line shape completely determined by population relaxation, the $v = 1$ state of the C=O transition has a lower limit of the population lifetime T_1 of 424 fs. More likely the T_1-value will be larger, since pure dephasing processes will also contribute to the line width.

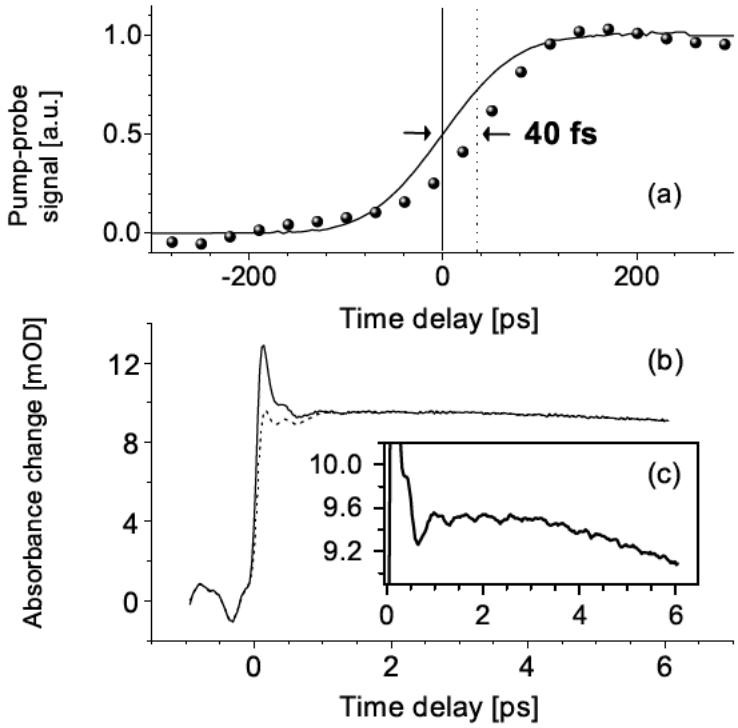

Figure 4.10: Transient signals measured at 1530 cm^{-1} with excitation at 335 nm. In (a) the initial delayed dynamics of HBT (dots) are compared with a cross-correlation signal measured in ZnSe (solid line). In (b) the dynamics are shown over a larger time range, with the measured signal (solid line) compared to that of HBT only after substraction of the solvent contribution (dashed line). In (c) a blow-up is presented of the signal due to HBT and solvent indicating the oscillatory contribution due to the anharmonically coupled low-frequency modes.

The decrease of absorption in the transient infrared spectra (see Fig. 4.6) is due to the bleaching of vibrational bands of the enol ground state of HBT (cf. Fig. 4.5). Even though, according to the calculations, no band can be assigned to a pure C-O stretch, the bands at 1272, 1318, 1460 and 1483 cm^{-1} possess some C-O single bond character which should disappear upon formation of the C=O double bond in the keto tautomer. At positive time delays, the analysis is complicated by the fact that new keto S_1 bands are created in the same spectral region (Fig. 4.6). At negative time delays, however, the time-resolved data measured at these frequencies show typical PFID features, i.e. a slow rise of bleaching with time, confirming that the original bands bleach after ultraviolet excitation (Fig. 4.6a, dotted line). These observations together with

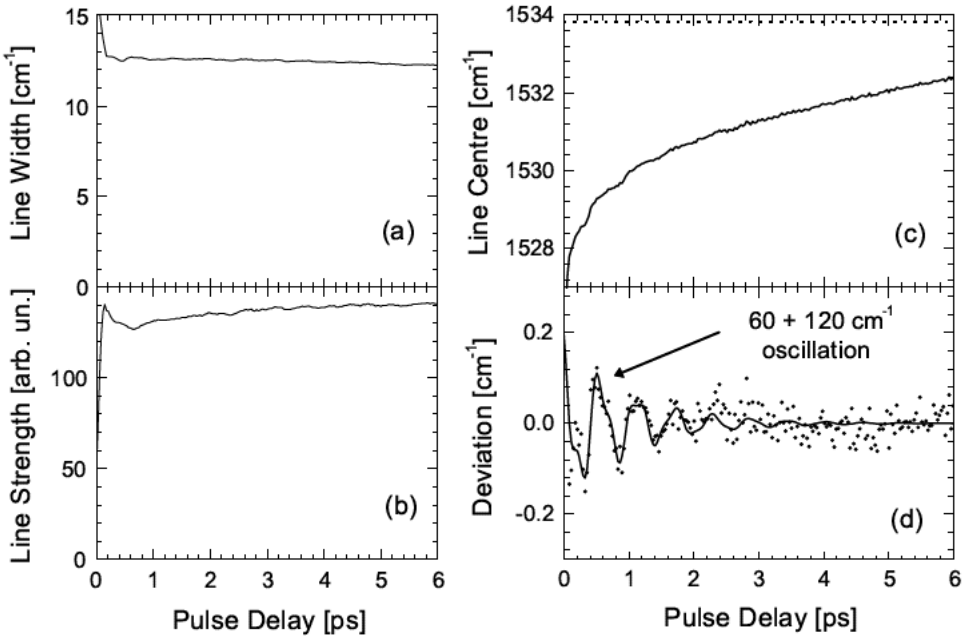

Figure 4.11: Results of the fitting procedure of the measured C=O band (excitation at 335 nm) with a Gaussian line shape. The width (a) and strength (b) of the C=O band do not change at longer delays. At early times the fitting routine is affected by the additional solvent contribution. In (c) the line centre of the C=O band (dots) shows a frequency up-shift with components of 0.6 ps and 14.5 ps. The coherent modulation of the line centre is clearly visible in (d), where the residue (dots) is shown after substraction of the biexponential fit on the data in (c). The solid line in (d) shows a function consisting of two oscillating contributions with frequencies of 60 and 120 cm^{-1} and a decaying constant of $\sim$1 ps.

the formation of the C=O stretching band around 1530 cm^{-1} give direct evidence of the formation of the keto geometry of HBT.

4.4.2 Coherence phenomena in photoinduced chemical reactions

Inspection of the transient recorded at 1530 cm^{-1} after excitation at 335 nm shows that oscillatory components are present in the response of the C=O mode (Fig. 4.10). The Gaussian fitting procedure of the transient C=O stretching mode band shape reveals that the temporal behavior of the line center exhibits these oscillatory features superimposed on the dynamical blue-shift in a more pronounced way (Fig. 4.11). Fourier analysis of the transient line center recorded

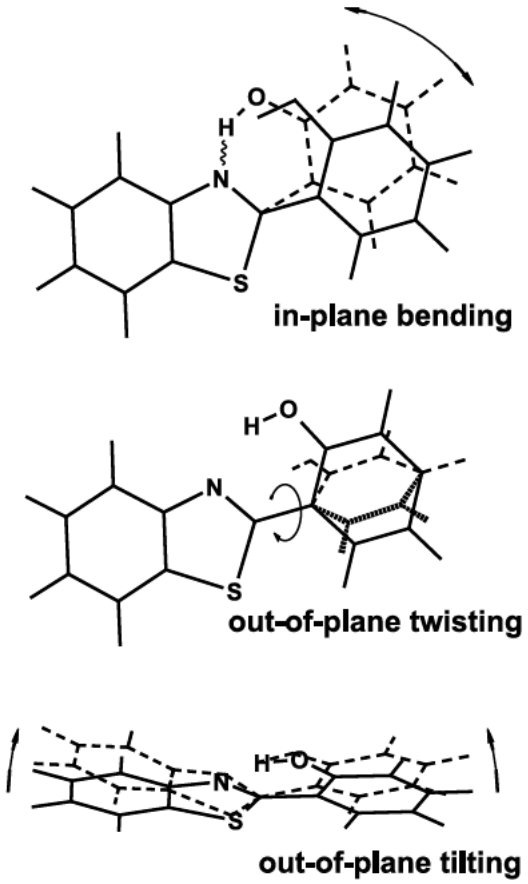

Figure 4.12: Schematic representation of the low-frequency in-plane bending, out-of-plane twisting and out-of-plane tilting modes. These modes are similar in the enol- and keto-tautomers.

with UV excitation at 335 nm reveals two components with frequencies of about 60 and 120 cm^{-1}. In contrast, with UV excitation at 349 nm only the 120 cm^{-1} component is observed.

Oscillatory features on vibrational bands have been observed before in IR-pump-IR-probe studies on O-H and O-D stretching modes in intramolecular hydrogen bonds in the electronic ground state [128,129]. In these works the oscillatory parts of the pump-probe signals are caused by coherent modulations of the O-H/O-D stretching band positions due to anharmonic coupling with coherently excited low-frequency modes. Here the frequency position of the C=O stretching mode is modulated by anharmonic coupling to one or two low-frequency modes, respectively. It was thus possible to detect, for the first time, such a spectral modulation by coherently excited low-frequency modes of a vibrational band marking the product state after a chemical reaction.

The assignment of these low-frequency modes in the keto*-product state can

be made by comparison to the well-known vibrational mode spectrum in the enol-ground state [123, 130] (see also Fig. 4.12). Although there is no guarantee that the vibrational mode spectrum is similar, ultrafast electronic pump-probe spectroscopic data have not shown substantial differences for the low-frequency Raman-active modes [120, 121]. One could anticipate that this also applies for other (infrared-active) modes. With this in mind one can correlate the 120 cm^{-1} vibrational mode to an *in-plane bending* motion of the two ring systems modulating the hydrogen bond length [123, 130]. This mode has been observed in electronic resonance Raman spectra indicating a strong displacement between the two enol potential energy surfaces. An *out-of-plane twisting* motion of the ring systems can be ascribed to the 60 cm^{-1} mode, also modulating the hydrogen bond length. This mode has an extremely low electronic resonance Raman cross-section, in contrast it is known to be infrared active [123]. A third mode is present at the low-end of the vibrational spectrum. This mode however involves an *out-of-plane tilting* motion of the two ring systems without strong motions of the atoms that constitute the hydrogen bond. The involvement of this mode is discarded in the following discussion.

A clear distinction between ultrafast UV-pump-VIS-probe and UV-pump-IR-probe spectroscopy must be made in relation to what one can expect in terms of coherently excited wave packet motions in the system under study. The ultrashort UV-pump coherently excites vibrational coherences on the enol-excited and enol-ground states of those modes that are strongly Raman active, and whose frequency lies within the bandwidth of the UV excitation pulse [3, 131–137]. These light-field driven coherences then evolve on the respective potential energy surfaces, and may even survive level crossings if the modes are not strongly coupled to the reaction coordinate. Another option is that vibrational wave packets are generated by rapid nonradiative processes from the initially excited reactant state to a product state [138–141]. In the latter case the surface crossing along the reaction coordinate is accompanied by the creation of a vibrational coherences along the coordinate of the vibrational mode that, in contrast to the previously mentioned case, is strongly coupled to the reaction coordinate. In the case of probing the product state the transient absorption or emission of a UV/VIS probe pulse is modulated by coherences in Raman-active vibrational modes. If no other knowledge than the Franck-Condon factors of the electronic transition induced by the UV-pump pulse exists on the particular molecular systems, one cannot decide whether the coherences are induced by the applied light pulse or by the subsequent chemical reaction. With regard to HBT for instance the Franck-Condon factors of the enol-S_0 to enol-S_1 state transition are well known [123,130], however this is not the case for the keto-S_1- to keto-S_0 state. Only when a coherence in the keto-S_1-state is observed that cannot be correlated to one of the modes that are Raman-active in the enol $\rightarrow$ enol* transition, one can safely conclude that the coherence is driven by nonradiative processes.

In the case of the ultrafast UV-pump-IR-probe experiment we probe the keto-

S_1-state by inspection a C=O stretching vibrational marker mode. Vibrational coherences in low-frequency modes are observed if the anharmonic coupling constants to the C=O stretching mode are sufficiently large. The factors determining the magnitude of coherent modulation of the infrared-signals by anharmonic coupling are different from those for coupling of vibrational modes to electronic transitions, and it should be of no surprise that coherences in both infrared- and Raman-active modes are visible.

With regard to the observation of the frequency and damping time of the 120 cm^{-1} mode earlier UV-pump-VIS-probe observations [120, 121] are confirmed. Higher frequency oscillations, most notably the 254 cm^{-1} mode, are not detectable in this work due to limited time resolution in comparison to the UV-pump-VIS-probe experiment. The observation of the 60 cm^{-1} mode, however, is a surprising result. The fact that this mode is not observed in the UV-pump-VIS-probe experiment suggests that for this mode there is not a huge shift between potential minima on the keto* $\rightarrow$ keto transition. Moreover it is known that the mode cannot be coherently excited by the UV-pump pulse as it has a low Franck-Condon factor in the enol $\rightarrow$ enol* transition. Excitation of this mode is thus driven by nonradiative processes after preparation of the excited enol*-state. One could regard this fact as an indication that the mode is impulsively excited by the hydrogen transfer reaction, where the reaction time is only one tenth of the oscillation period of the mode. From the observations that a) the 60 cm^{-1} mode is not observable at 350 nm where the electronic origin (0-0) transition is located, whereas b) the reaction time appears to be independent of the excitation energy, one can tentatively conclude that the coherent excitation of the infrared-active 60 cm^{-1} out-of-plane deformation mode is driven by an IVR mechanism in the enol excited state.

4.4.3 Vibrational relaxation processes induced by hydrogen transfer

The new (positive) vibrational bands in the spectra of Fig. 4.6 mark the keto S_1 state. All new bands display blue-shifts with time without undergoing a significant reshaping and/or broadening of their spectral envelopes. For the same reasons mentioned above for the C=O stretch, all new bands can be assigned to the $v = 0 \rightarrow 1$ transition of the respective vibration. For all of them, attributing the spectral width of the measured lines to (homogeneous) lifetime broadening, a lower limit to the population lifetimes of $v \geq 1$ levels of 200 to 400 fs is estimated, i.e. populations of $v \geq 1$ levels could easily be detected in our experiment. As all modes in the fingerprint region display a finite anharmonicity on the order of 10-30 cm^{-1} [30], stimulated emission and/or absorption from $v \geq 1$ levels would give rise to additional spectral components, different from the $v = 0 \rightarrow 1$ transition. We conclude from the absence of such features that nonequilibrium populations

of $v \geq 1$ levels are negligible. All such modes are created in their $v = 0$ ground state, i.e. are not elongated and do not accept vibrational excess energy upon hydrogen transfer.

The blue-shift of the central frequencies of all new bands by 2 to 7 cm^{-1} within 50-60 ps is due to transient populations in other modes that couple anharmonically to the fingerprint vibrations. Blue-shifts of vibrational bands after a photo-induced chemical reaction have been observed before in the picosecond time regime in the case of for instance trans-stilbene [142] and azobenzene [39]. It can be rationalized by the model briefly described in Section 2.4 of Chapter 2,describing the spectral position of vibrational lines as a function of vibrational populations of anharmonically coupled modes [39]. For negative values of the off-diagonal anharmonic coupling constants, which is the most common case, this model predicts a red-shifted $v = 0 \rightarrow 1$ transition of a mode k for high excess populations of modes i ($i \neq k$) coupling to the mode k, and a subsequent blue-shift to the steady-state spectral position with decreasing population. In the cited studies [39, 142] it was assumed that at picosecond time scales the excess energies are thermally distributed amongst the vibrational modes. Specific spectator modes appear shifted due to anharmonic coupling with the bath of all highly populated low-frequency modes. However, the same red-shift behaviour would occur when only a limited set of highly populated normal modes takes place. This may be the case for HBT, since a full equilibration of excess energy is unlikely on the time scale of 50 fs. It is likely that only a limited number of accepting normal modes strongly coupled to the hydrogen bond coordinate will initially redistribute the excess energy between the enol* and keto* excited states [143, 144].

The transient spectra in the fingerprint region give no direct insight into which anharmonically coupled modes underlie the blue-shift of the different bands. There is, however, detailed information from steady-state resonance Raman spectra of enol-HBT and from femtosecond studies of electronic transitions: (i) The resonance Raman spectra give evidence of several modes at frequencies below 700 cm^{-1} that are strongly coupled to the S_0-S_1 transition of the enol tautomer and display substantial anharmonicities giving rise to combination bands in the Raman spectrum [123, 130]. Upon femtosecond excitation, such modes are elongated, i.e. acquire a substantial nonequilibrium population. Some of them, the vibrations at 118, 254, 289, and 530 cm^{-1}, display coherent oscillations within the first few picoseconds [120, 124]. Such oscillations represent the coherent motion of vibrational wavepackets which are made up of a coherent superposition of at least the $v = 1$ and $v = 2$ eigenstates of the respective oscillator, i.e. contain at least 2 vibrational quanta of the respective mode. This gives a minimum excess energy in such modes of about 2200 cm^{-1} which is a major fraction of the total excess energy of $\sim$3000 cm^{-1} released upon hydrogen transfer [143]. These findings strongly suggest that the blue-shift of the vibrational bands in the fingerprint region is mainly due to excess populations of such Raman active low-frequency vibrations.

Coherent wavepacket motions in the anharmonically coupled low-frequency modes result in a periodic modulation of the spectral position of high-frequency modes. For the O-H stretching mode in the enol ground state of HBT, oscillations with an amplitude on the order of 10^{-4} OD have been observed [129]. In the measured blue-shift of the fingerprint vibrations (Figs. 4.7, 4.9), oscillations due to Raman-active modes are absent because of the limited spectral resolution and sensitivity of the present experiment which in fact averages over the spectral modulation. Consequently, we observe a continuous blue-shift of the bands with time constants of 700 fs and 15 ps (see Fig. 4.9), reflecting the decreasing excess populations of the low-frequency modes.

The fast component is most probably due to intramolecular redistribution processes (IVR) by which the excess populations are randomized within the excited HBT molecules [145]. It is interesting to note that the damping time T_2=1-2 ps of the coherent oscillations observed in Refs. [120, 121] is about twice the redistribution time $T_1 \cong 700$ fs found here, as is expected for a dephasing dominated by the population relaxation of excited vibrational levels. The slower component in the blue-shift is attributed to a flow of excess energy from the HBT molecule into the liquid surroundings [145], i.e. a cooling of the excited molecule towards ambient temperatures. For medium-sized molecules typical values for time scales of cooling are found to lie in the picosecond range [145–147].

4.5 Summary and conclusions

Fig. 4.13 presents an overview of the ESIHT reaction in HBT and of the processes that follow the ultrafast hydrogen transfer reaction, as suggested by the ultraviolet pump/mid-infrared probe experimental results.

Within 50 femtoseconds, the formation of the keto species was directly observed by probing the dynamics of the C=O carbonyl stretching mode formed by hydrogen transfer, thus avoiding the ambiguity resulting, in the optical techniques, from the wavelength dependent rise time of keto*-emission. The bleaching of those vibrational bands of the enol ground state which possess C-O single bond character also gives the evidence of the formation of the keto tautomer.

As consequence of coherence phenomena, the observed dynamics of the carbonyl band show oscillatory features, due to the motions of wavepackets along two low frequency modes which anharmonically couple to the C=O stretching vibration, an IR active mode (60 cm^{-1}) - coherently excited by nonradiative processes within the excited enol state after electronic excitation - and a Raman active mode (120 cm^{-1}) - impulsively excited upon the electronic transition. These wavepackets are destroyed through the loss of coherence induced by dephasing processes occuring on time scales of 1-2 picoseconds, as typical for vibrational excitation in the liquid phase.

The transient vibrational spectra in the fingerprint region between 1000 and

1700 cm^{-1} have given insight into the processes of vibrational energy redistribution. The range of the excited state potential populated by the excitation on the enol S_0-S_1 transition has an excess energy of several about 3000 cm^{-1} with respect to the keto minimum. This excess energy is redistributed within the vibrational manifold during and after the hydrogen transfer. After the ESIHT reaction, the different vibrational bands display a red-shift with respect to their asymptotic spectral position which is reached within 50 to 60 ps. All the IR active keto*-vibrations appear to be created in their ground state, i.e. they do not accept vibrational excess energy upon hydrogen transfer. It is specially interesting to note, in particular, that the elongation of the C=O stretch is not implied in the hydrogen transfer reaction. The initial red-shift is caused by transient populations of Raman-active low-frequency modes which couple anharmonically to the modes in the fingerprint region. During the first few picoseconds, such low-frequency modes contain the major fraction of vibrational excess energy which subsequently flows into a multitude of modes cooling down on a 50 to 60 ps time scale. These relaxation processes manifest themselves in a blue-shift with time of the vibrational lines in the fingerprint region. The fast and the slow component of the shifting dynamics can most probably be assigned to intramolecular redistribution processes (IVR) and flow of energy from the molecule into the surroundings (cooling), respectively.

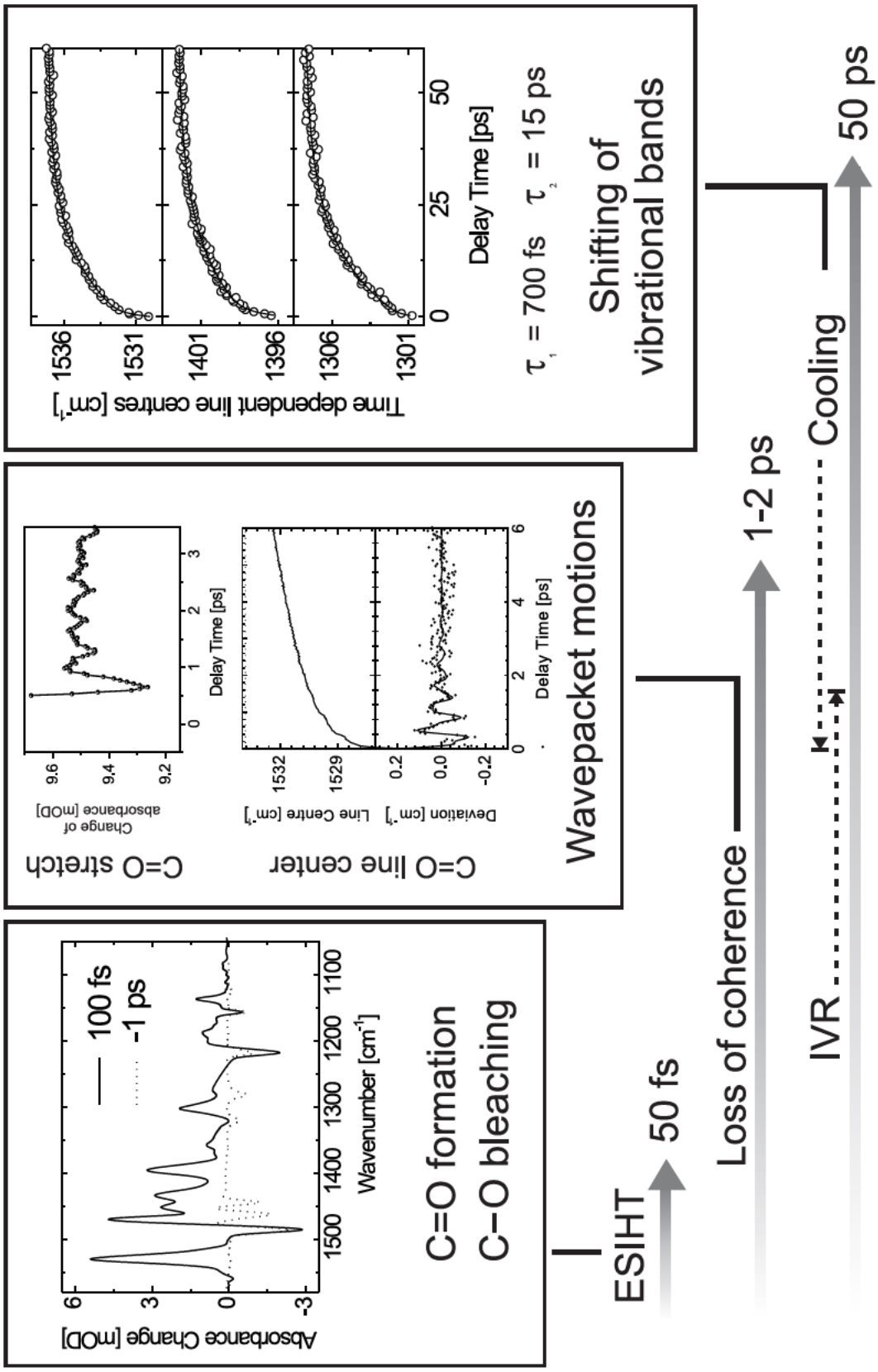

Figure 4.13: Overview: ESIHT reaction and following processes in HBT.

Chapter 5

Intermolecular excited state proton transfer

5.1 Introduction

The classic work of Brnsted [148, 149] has shown that an intermolecular proton transfer reaction is involved in the paradigm reaction of solution chemistry: the acid-base neutralization reaction. In the most general case, it can be written as:

$$\mathrm{AH(acid) + B(base) \rightleftharpoons A^-(base) + BH^+(acid)}$$

where A^- is the conjugated base of the acid AH, BH^+ the conjugated acid of the base BH. A more modern observation is that proton transfer proceeds typically along a pre-existing hydrogen bond, where the reactive coordinate is of the type $A{-}H\cdots B$. Intermolecular proton transfer reactions of Brnsted acids and bases are of fundamental importance in chemistry and biology as these are key processes in phenomena such as the autoionization in water [88], the anomalous high proton mobility in water (von Grotthuss mechanism) [150, 151], acid-base neutralization reactions [152], enzyme catalysis [153], and proton pumps through membrane protein channels [154].

More than 50 years ago, Förster [155–157] showed that the large Stokes shift found in the fluorescence spectra of several classes of aromatic dyes was the consequence of an excited state proton transfer (ESPT) reaction. Such aromatic compounds that exhibit strong photoacidity (or photobasicity), i.e. an increase of the acidity (or basicity) constant after photoexcitation, may be viewed as molecular initiators of acid base reactions as well as molecular probes for real-time observation of the progress of proton transfer reactions. To be more precise, the term *photoacids* describes those molecules that may undergo a non-destructive, fully reversible proton transfer reaction in their electronic excited state [158], not to be confused with other classes of molecules generating protons following a photo-destructive process, termed *photoacid generators* [159]. Photoacid

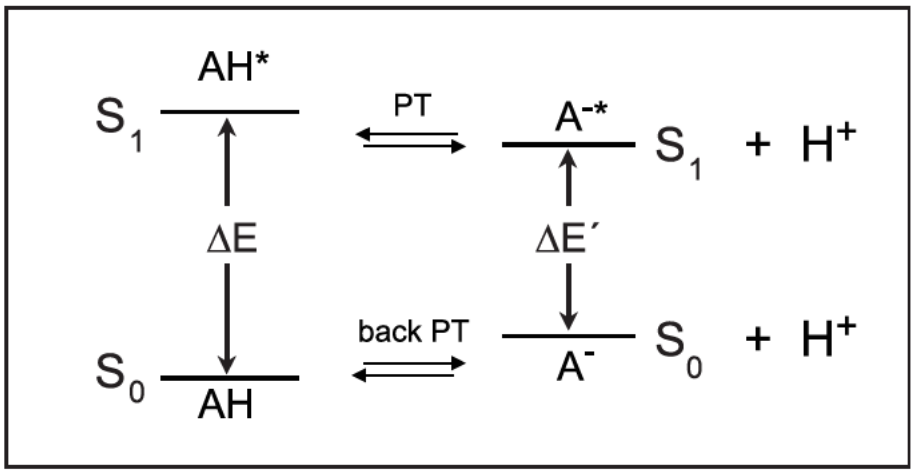

Figure 5.1: Schematic representation of the reversible Förster cycle initiated by electronic excitation of a photoacid molecule AH. S_0: ground state, S_1: first singlet excited state, PT: proton transfer, ΔE and ΔE': energy changes for the transition from the ground state to the first singlet state of the photoacid and its conjugated anion, respectively.

and photobase probes have provided, in combination with short-pulse laser spectroscopy, efficient means for creating and monitoring the progress of very rapid acid-base reactions in solutions, making many aspects of the intermolecular proton transfer reactions experimentally accessible. The enhancement of acidity after photo-excitation has also been the basis for several technological and scientific applications, such as photo-polymerization and photo-depolymerization [160], pH jump experiments [161], probing of the environment around proteins and micelles [162].

Fig. 5.1 shows a schematic representation of the reversible cycle (Förster cycle) initiated by excitation of a photoacid to the first singlet state S_1. The electronic excitation is accompanied by a dramatic increase of the acidity, leading to the proton transfer reaction, either to the solvent or to a base dissolved in solution. If the excited state lifetimes of both the protonated and deprotonated form of the photoacid are long compared to the rate constants for the dissociation and the recombination reactions, an excited state acid-base equilibrium is reached. In this case, except for their transient nature, photoacids resemble completely ground-state acids. The strength of a conventional ground-state acid is usually quantified by its acidity constant K_a, defined as the equilibrium constant for the proton transfer reaction in water:

$$AH + H_2O \rightleftharpoons A^- + H_3O^+$$

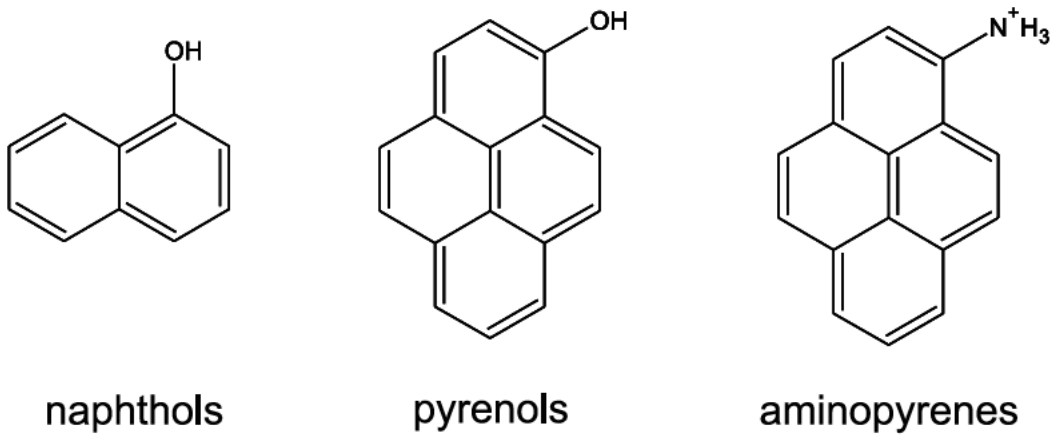

Figure 5.2: Most commonly used families of photoacids.

K_a is then given by:

$$K_a = \frac{[H_3O^+][A^-]}{[AH]}$$

Usually the acidity constant is expressed in logarithmic units, because this simplifies a number of thermodynamic equations [163]:

$$pK_a = -\log K_a$$

Similarly, one can characterize the strength of a photoacid by assigning an excited state equilibrium constant pK_a^* to the proton dissociation reaction in water. pK_a^* can be determined by measuring quantum yields of fluorescence as a function of the pH of the solution. In the literature, the jump of pK following the electronic excitation has been often estimated from absorption and fluorescence spectra [164, 165]. Referring to the schematic energy diagram of Fig. 5.1, if one assumes equal entropy changes due to the proton transfer reactions in the ground and excited states, it follows that [164]:

$$pK_a - pK_a^* = \frac{\Delta E - \Delta E'}{2.303RT}$$

The values obtained by the two methods are normally in good agreement. In photoacids, the enhancement of acidity after photoexcitation is typically by a factor of 10^6-10^8 in the acidity constant, i.e. a decrease of 6-8 units in the pK_a value [94].

Since the early discovery of photoacidity, hundreds of molecules have been shown to exhibit photoacidity [166]. Among them, the most commonly used belong to the three families initially introduced by Förster and Weller [94, 155–157]: the naphthols, the pyrenols and the aminopyrenes (see Fig. 5.2). The

naphthols and the pyrenols are neutral photoacids, whereas the aminopyrenes need to be protonated in the ground state in order to exhibit photoacidity. It cannot be claimed that the excited state proton transfer is completely understood from a microscopic point of view: in the literature, two perspectives have tried to give a general description of photoacidity. In a charge transfer picture [167, 168], upon excitation an intramolecular charge transfer occurs from a non bonding orbital of the electronegative atom X of the R-X-H structure (X = O, N or S) into a π^* orbital of the aromatic ring system, creating a partial positive charge on the atom X. The enhanced acidity is then seen as the result of the Coulombic repulsion of the proton. A more spectroscopic perspective [169, 170] points at a full internal conversion process between two electronic states, from a relatively non-polar to a polar state (L_b to L_a transition according to the Platt notation for aromatic compounds [171]), where L_b is the spectroscopically accessed state and L_a is a state of different symmetry. The two aforementioned perspective have been largely orthogonal, and neither explains satisfactorily all fundamental questions about the excited state proton transfer from photoacids. The exact molecular mechanism of the ESPT, e.g. the identity of the reaction coordinate, still has to be cleared. Another interesting observation is that, in the majority of photoacids, the ESPT is essentially observed only in water or in aqueous solutions and not in other polar solvents [172, 173], whereas e.g. the ground state proton transfer occurs both in water and in other organic solvents [173]. The fundamental reasons behind the special role of water in the ESPT remains to a large extent unknown.

From an experimental point of view, the dynamics of the ESPT reaction have been typically studied by probing the electronic states of the molecular systems involved in the reaction (photoacids and conjugated photobases) through time-resolved fluorescence or optical-pump/optical-probe spectroscopy [172, 174].

One of the first goals of the research on these systems was the measurement of the rate of the proton transfer from photoacid to solvents, especially in aqueous solutions. The suggestive idea behind these studies was to explore the possibility of using the ESPT reaction to address fundamental questions concerning proton-solvation and proton transfer mechanisms in these solvents, to shed light on problems such as e.g. the anomalous high mobility of protons in liquid water [150]. For 8-hydroxy-1,3,6-pyrene trisulfonate (HPTS), one of the most studied photoacids, the ESPT reaction was found to proceed in water within 100 ps [175], as measured by monitoring with a streak camera the decay of the neutral species fluorescence and the growth of the anionic species emission. 1- and 2-naphthols and their sulfonate derivatives as well as 2-naphthols with a cyano group substitution in the distal ring (cyano-naphthols) have also received considerable attention [158]. The effect of deuteration and of adding organic solvents to water on the dissociation rate of naphthols-photoacids has been studied by Robinson et al. [176, 177], who proposed the description of the reaction as a barrier-crossing along a solvent coordinate with a frequency factor given by the dielectric relaxation time of the solvent; in these works, the decrease of the proton transfer rate with increasing

concentration of organic solvents in water was interpreted as a manifestation of a water structure breaking effect.

The dissociation rate and the excited state equilibrium constants of various photoacids were found to correlate very well with their photoacidity [178], confirming that photoacids obey the same empirical reactivity laws as the overwhelming majority of ground-state acids. From these observations, an empirical 'universal' law was suggested which relates the pK_a^* values of photoacids to the proton transfer rate constants [178].

Other studies [179,180] have underlined the importance of the competing geminate recombination process (back recombination following the proton dissociation), showing that it has a considerable effect on the dissociation rate. The experimental signature of this process is the non-exponential decay of the fluorescence of the photoacid, following the $t^{-3/2}$ law which is predicted by classical models describing reversible geminate dissociation-recombination reactions [179].

The introduction of moderate concentrations of base in the photoacid solution [181] results in the reduction of the geminate recombination yield: the base acts as 'proton scavenger', reacting with the geminate proton before it recombines with the anion, hence reducing the probability for the proton to recombine with its geminate anion. Several experimental studies have been devoted to the direct proton transfer from the photoacid to a base [181–183], where a diffusive model based on the Smoluchowski theory [184], previously extended to the description of fluorescence quenching reactions [185], has been employed to describe the dynamics of the bimolecular acid-base proton transfer process. The reaction rate in this case is then limited by the relatively slow mutual diffusion coefficients of the reactants. An attempt of measuring the intrinsic proton transfer rate to a base, separating the reaction rate at contact from the diffusive aspects, has been proposed in [183].

Recently ESPT reactions in clusters of cyano-naphthols, generated in a molecular beam, have been studied as a complement to solution experiments [186], giving insight into the cluster size threshold for ESPT, the rates of ESPT and geminate recombination in clusters, the role of vibronic coupling as a trigger for the reaction.

The work reported in this chapter provides a complete and clear picture of the ESPT reaction from a photoacid to water and to a base dissolved in water, as obtained by means of femtosecond mid-infrared spectroscopy, following specific infrared active vibrational marker modes, present at the proton-donor and proton-acceptor sides. All time scales governing the acid-base reaction dynamics have been monitored, distinguishing between the ultrafast on-contact proton-transfer along a connecting hydrogen bond and the case of reaction between initially uncomplexed acid base pairs.

5.2 Excited state proton transfer from HPTS

The object of the ultrafast mid-infrared study is the photoacid 8-hydroxy-1,3,6-trisulfonate-pyrene (HPTS) [156] dissolved in deuterated water, a molecular system that has extensively been studied with a variety of experimental approaches, including time-resolved single photon counting fluorescence measurement [179, 183,187] and UV/VIS-pump-VIS-probe spectroscopy [181]. The photoacid HPTS changes it pK_a value by about seven units from pK_a (S_0) = 6.6 to pK_a (S_1) = 0.0, making HPTS in the excited state a strong acid. Our work investigates the dynamics of the deuteron transfer to solvent (DTTS) in deuterated water and of deuteron transfer to base (DTTB) in the reaction between HPTS and acetate. Fig. 5.3 shows the reaction schemes and the electronic absorption spectra of HPTS and of the conjugate anion. Reaction I shows deuteron transfer to solvent (DTTS) water. The introduction of moderate concentrations of base in the solution adds a competing reaction channel (II), the deuteron transfer to base (DTTB) acetate. At moderate concentrations, the proton appears to be first transferred to the solvent and then shuttled to the base. At sufficiently high base concentration direct deuteron scavenging dominates (Reaction III). Deuterated water is employed, since the studied vibrational marker modes fall in the spectral region where the absorption due to the O-H bending mode of H_2O would make experiments in a 100 μm jet unfeasible.

In acid-base complexes, the general dependence of the percentage yield of proton/deuteron transfer on the difference between the pK of the base (pK_B) and that of the acid (pK_A), $\Delta pK = pK_B - pK_A$, is given by a curve such as the one plotted in Fig. 5.4, exhibiting a switching behavior: for small ΔpK no proton/deuteron transfer occurs, whereas when a certain threshold is exceeded ($\Delta pK^{50\%}$), 100% of the protons/deuterons are transferred to the base. This curve based on an extensive compilation of data of several families of related acid-base reactions reviewed by Zundel [188]. The $\Delta pK^{50\%}$ values at which 50% proton transfer is observed are characteristic of the families of systems and depend on interaction effects influencing the symmetry [188]. Values of $\Delta pK^{50\%}$ between 2 and 3 are typically encountered. Comparing the pK_a value of acetate (pK_a = 4.8) with that of HPTS in the ground (pK_a (S_0) = 6.6) and in the excited state (pK_a (S_1) = 0) it is clear that in an HPTS-acetate complex the photoacid will only transfer its deuteron to acetate when excited to the S_1-state.

Until now, proton transfer dynamics of photoacids have been studied by inspection of the photoacid decay or the rise of its conjugated photobase by probing electronic states of these molecular systems through time-resolved fluorescence or optical-pump/optical-probe spectroscopy [172, 174]. It has not been possible to detect the arrival of the proton at the accepting site with electronic spectroscopy, where the proton accepting base is either the solvent or a Brønsted base added to the solution in a suitable concentration. Moreover, for condensed phase studies electronic transitions are usually sensitive to intramolecular vibrational redistri-

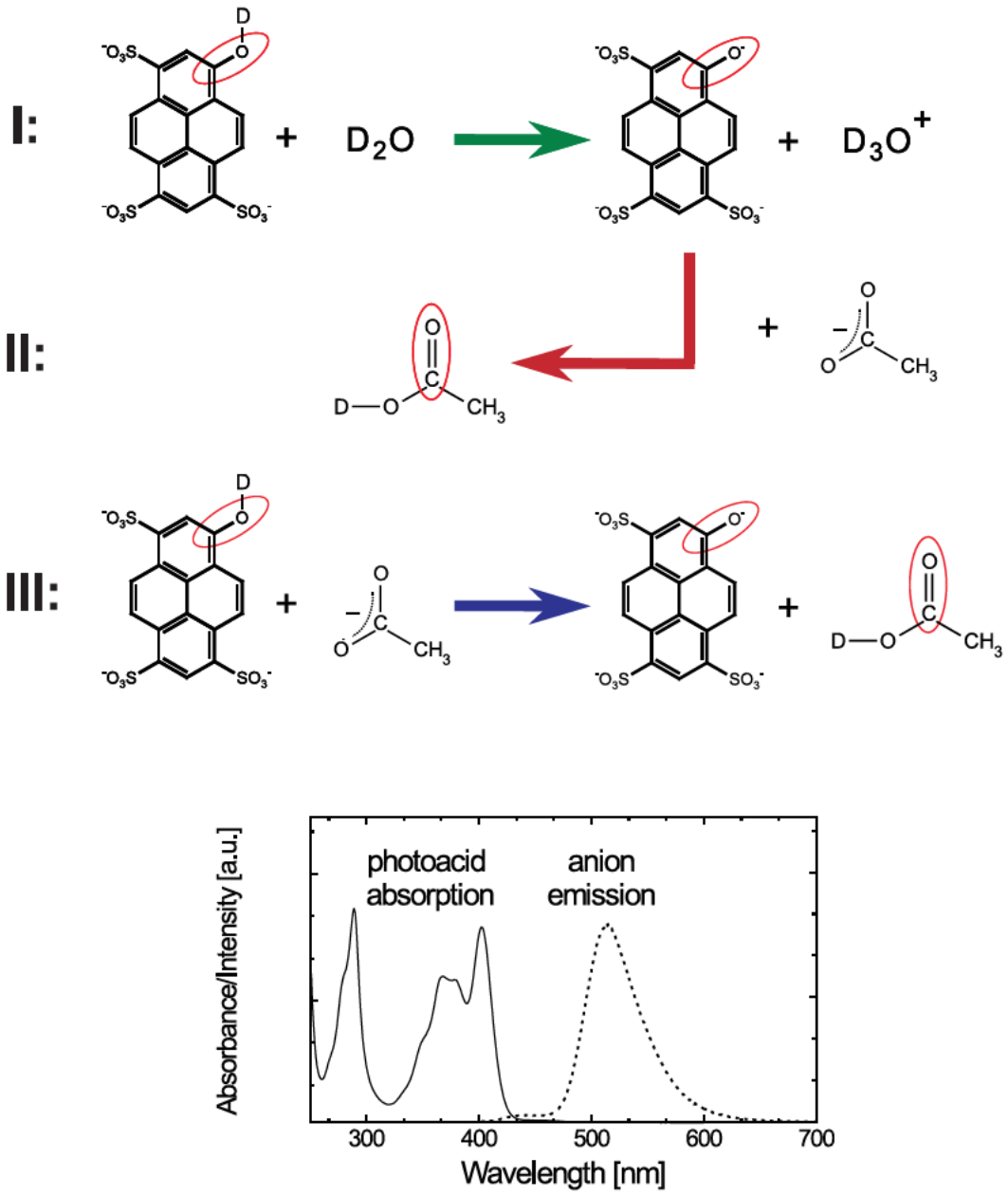

Figure 5.3: Reaction schemes (HPTS is shown with the hydroxy-group in the up-configuration). Reaction I shows deuteron transfer to solvent (DTTS) water. The introduction of moderate concentrations of base in the solution adds a competing reaction channel (II), the deuteron transfer to base (DTTB) acetate. Reaction III: At high base concentration direct deuteron scavenging dominates. The groups determining the most relevant vibrational modes in terms of the deuteron transfer reaction are marked: the C=O stretching mode of acetic acid and those vibrations with aromatic ring C-O stretching activity. Lower panel: steady-state absorption spectrum of HPTS and fluorescence spectrum of the conjugate anion $HPTS^-$, typifying the Förster cycle of Fig. 5.1.

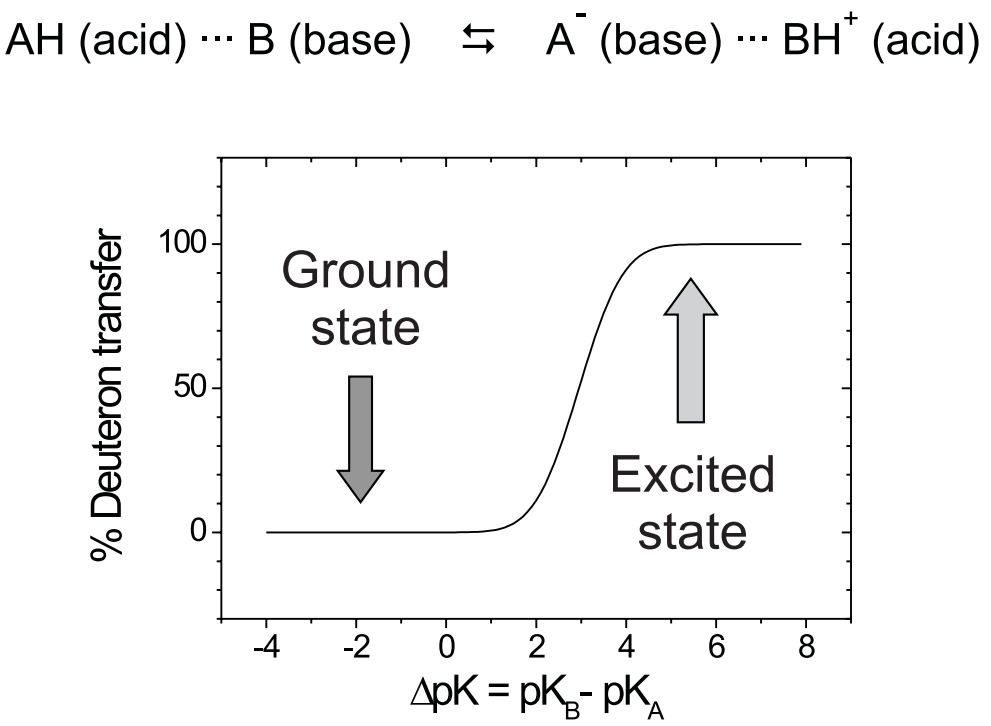

Figure 5.4: Photoacidity of HPTS and deuteron-transfer to solvent or acetate are switched on by optical excitation. The solid line indicates the general dependence of the percentage yield of proton/deuteron transfer on $\Delta pK = pK_B - pK_A$ and is based on compilation of data of several families of related acid-base reactions reviewed by Zundel [188]. For a HPTS-acetate complex, $\Delta pK(S_0) = -1.8$, $\Delta pK(S_1) = +4.8$

bution (IVR), vibrational cooling (vibrational energy dissipation to the solvent) and solvent reorganization (solvation dynamics). These effects may mask the dynamics of the proton transfer process. In addition practical experimental issues concern the limited time-resolution in time-correlated single-photon counting and excited-state absorption in UV pump/VIS probe. In both cases these factors may hinder the observation of those phenomena occurring on a sub-picosecond time scale.

In this work, mid-IR spectroscopy after the optical trigger pulse is used to follow specific IR-active vibrational marker modes present at the proton-donor and proton-acceptor sides. In Fig. 5.3 the molecular groups determining the most relevant vibrational marker modes are marked. The deuteron arrival at the accepting base can be monitored by detecting the IR active C=O stretching mode of acetic acid located at 1720 cm^{-1}. The decay of the photoacid population in favor of the anion is observed by detection of changes of the IR spectrum in the 1250-1600 cm^{-1} frequency range, where according to steady-state ground-state

measurements and to ground-state *ab initio* calculations, major changes in the vibrational spectrum are expected upon the photoacid → anion transition (see the discussion of the IR spectrum of HPTS presented in the following section 5.3).

5.3 Results and discussion

In order to identify which vibrational marker modes have to be studied, a careful experimental and theoretical analysis of the ground state spectra of the HPTS molecule in the acidic and in the anionic form has been carried out. A comparison of the steady-state experimental infrared spectra of HPTS and its anion in the electronic ground state is shown in Fig. 5.5 (C), as measured in a solution of HPTS in D_2O respectively at a $pD = 5$ (HPTS predominantly in its acidic form) and at a $pD = 12$ (HPTS in its ionic form) - pD is the analogue of pH for the deuterated case. Quantum chemical calculations have been performed with the B3LYP/6-31G(d) density functional method implemented in GAUSSIAN98 [126]. The theory indicates that two different configurations occur for HPTS, with different conformation angles of the hydroxyl group with a small energy difference of 90 cm^{-1}. It is thus likely that both conformers occur in room temperature solutions. The calculations allow to assign the observed vibrational bands in the fingerprint region to three groupings, both for the case of HPTS (Fig. 5.5 A) and for its anion (Fig. 5.5 B). The vibrational transitions of modes involved in motions of the sulfonate groups are found between 950-1050 cm^{-1} (aryl-SO_3^- stretching modes) and 1100-1250 cm^{-1} (S-O stretching modes). These modes do not change their characteristics significantly when HPTS converts into the anion. Modes predominantly involving aromatic ring deformations, and modes where the mixing of C-O stretching and aromatic ring deformation vibrations contribute are found in the range 1250-1650 cm^{-1}. No single isolated C-O stretching vibration occurs for HPTS, and the same applies for the anion. However, since a transition from HPTS to anion due to proton transfer is accompanied by a change in electronic charge distribution, the vibrational transitions due to modes with C-O stretching content will change in frequency position and absorbance strength. This is most pronounced when comparing the IR spectra of ground state HPTS and ground state anion in the frequency range between 1450-1600 cm^{-1}. It can be argued that a successful observation of deuteron transfer dynamics of HPTS in the electronic excited state is thus expected when studying the transient mid-infrared absorbance changes in this frequency range. Despite the a priori lack of identifiable marker modes in HPTS and the anion the time-resolved study in this frequency range, as shown in the following, reveal the deuteron transfer dynamics. The arrival of the deuteron at the accepting base acetate, on the other hand, is perfectly observable, since the reaction product acetic acid has a strong C=O stretching marker mode which can be unambiguously assigned to a vibrational

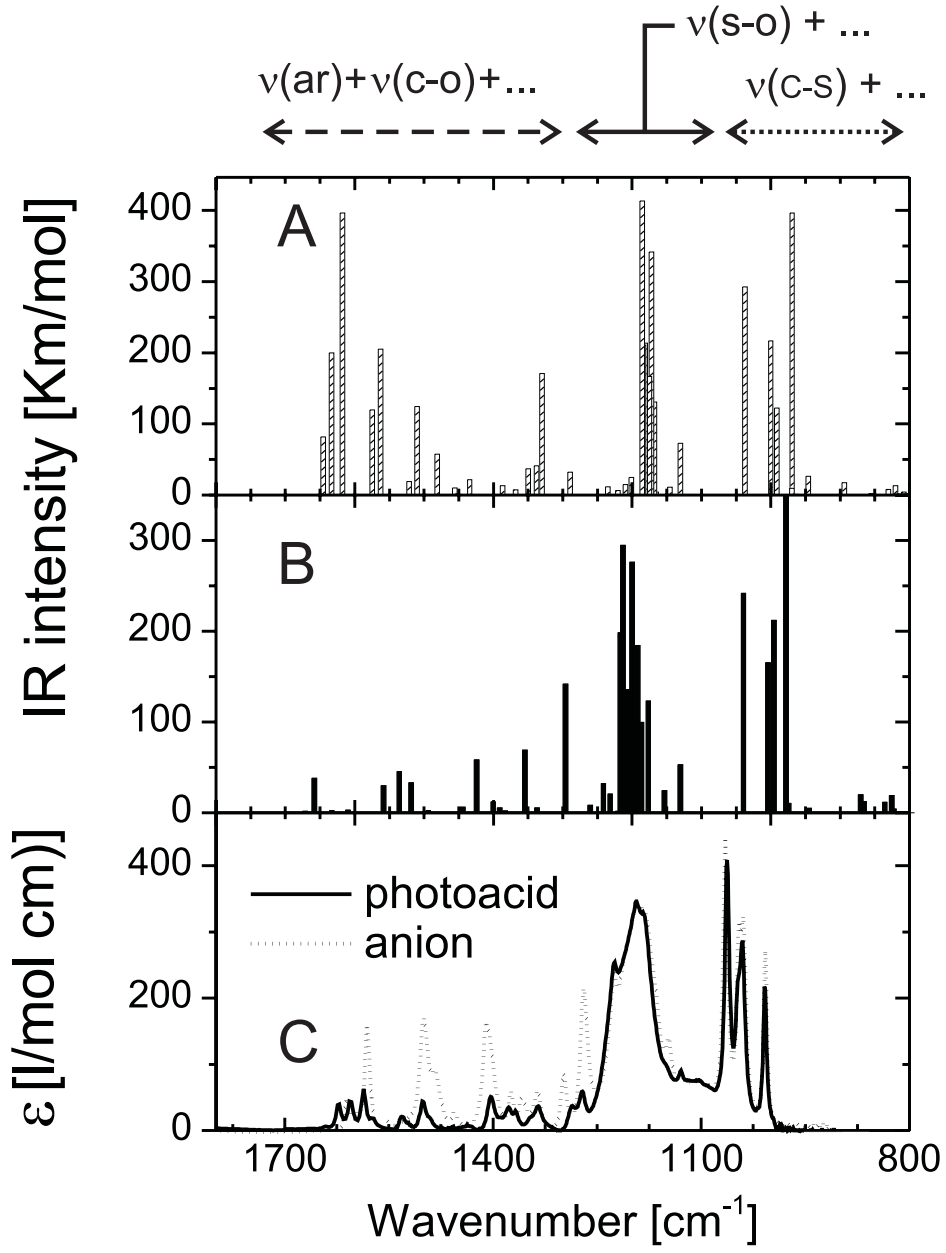

Figure 5.5: Ground state spectra in the fingerprint region for HPTS and its anion: Calculated (B3LYP/6-31G(d), scaled by 0.975) infrared bands in the ground state for (A) HPTS (up-conformer) and (B) the $HPTS^-$ anion. (C) Experimental steady-state infrared spectra of HPTS in D_2O at a $pD = 5$ (solid line, HPTS predominantly in its acidic form) and at a $pD = 12$ (dashed line, HPTS in the anionic form). The bands are assigned to three groupings according to their character.

line located at 1720 cm^{-1} (see Fig. 5.6 C).

The deuteron transfer dynamics from HPTS to the solvent (deuterated water) and to the base (acetate) were investigated. In the ultraviolet pump/mid-infrared probe experiments, solutions of HPTS (at a fixed concentration of 20mM) in deuteriumoxide (99.8% deuteration grade) were used. Potassium acetate (Aldrich) served as the accepting base at different concentrations. The deuteron transfer dynamics were studied as a function of acetate concentration, varied in the range of 0.25-4 M. A small amount of acetic acid (Aldrich) was added to ensure that HPTS was present in the photoacid form. The second harmonic of the Ti:sapphire laser was used for excitation (wavelength 400 nm, pulse duration 55 fs, energy 6 μJ, spot diameter at the sample about 200 μm) to excite about 15% of the HPTS molecules in the 100 μm-thick jet of the sample solutions. The mid-infrared probe pulses were tuned between 1250 and 1800 cm^{-1} in order to monitor the evolution in the spectral range where those vibrations identified as marker modes are located (see discussion in the previous section).

Fig. 5.6 (A) shows the measured transient spectra of HPTS in D_2O (1350-1600 cm^{-1}) and the growing in of the C=O stretch signal indicating the acetic acid formation in a 4 M solution of acetate (1650-1780 cm^{-1}) after femtosecond laser excitation. As a comparison, Fig. 5.6 (B) shows the steady state IR spectra of the photoacid HPTS in D_2O (recorded at $pD = 5$) and its conjugate photobase (recorded at $pD = 12$) in their electronic ground states, whereas Fig. 5.6 (C) gives the IR spectrum of acetic acid, characterized by the IR-active C=O stretching vibration. The transient bands at 1486 and 1539 cm^{-1}, appearing upon electronic excitation of HPTS within time resolution, are assigned to be indicative of the photoacid in the S_1-state. The 1539 cm^{-1} band cannot be used as marker mode since it is hidden behind strong acetate bands in the experiments with the scavenging base. A band at 1503 cm^{-1} is observed, growing in on a time scale of several hundred of picoseconds in the case of HPTS in D_2O (no acetate added). This band is allocated to be a marker for the deuteron transferred HPTS anion (photobase) in the S_1-state. From here on the band at 1486 cm^{-1} is used as marker mode for the photoacid and the 1503 cm^{-1} transition as indicator for the generation of the anion. It is clear from the transient spectra of Fig. 5.6 that at 1486 cm^{-1} a band of the anion replaces the photoacid band, suggesting that the vibrational mode responsible for the transition only changes its absorption strength upon the photoacid $\rightarrow$ anion transition.

Figure 5.7 shows the decay of the photoacid band at 1486 cm^{-1} and the rise of the anion band at 1503 cm^{-1} for two orthogonal polarizations of the mid-IR probing pulses. Since the observed bands in this spectral region partially overlap, a singular value decomposition analysis of the transient spectra was performed in order to better evaluate the dynamics of the vibrational lines. The differences in the dynamics measured at different polarizations are a consequence of the dependence of the pump-probe signal on the relative angle λ between optical and infrared transition dipole moments. The dynamics are affected by effects

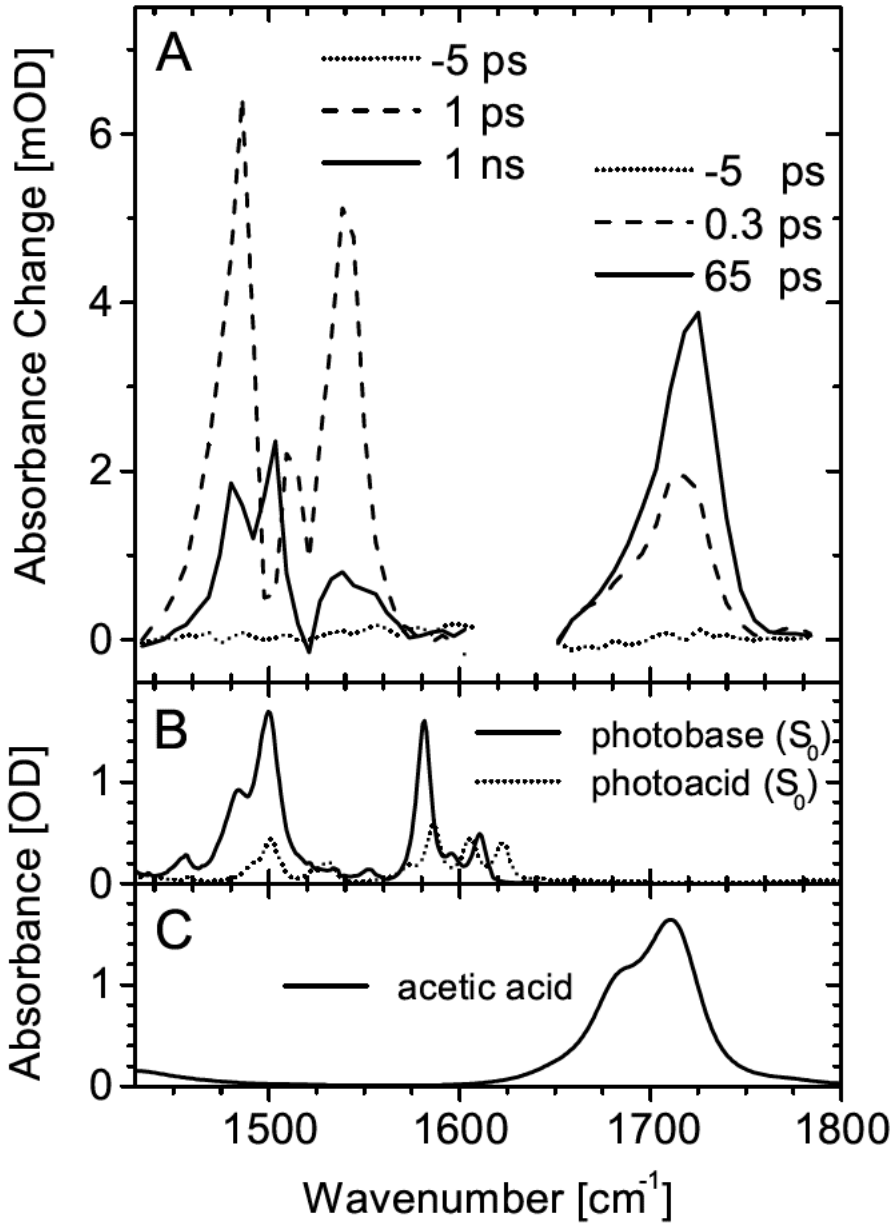

Figure 5.6: (A) Transient spectra of HPTS in D_2O (1350-1600 cm^{-1}) and growing in of acetic acid signal in a 4 M solution of acetate (1650-1780 cm^{-1}) after femtosecond laser excitation. (B) steady state IR spectra of the photoacid HPTS in D_2O (recorded at $pD = 5$) and its conjugate photobase (recorded at $pD = 12$) in their electronic ground states. (C) IR spectrum of acetic acid.

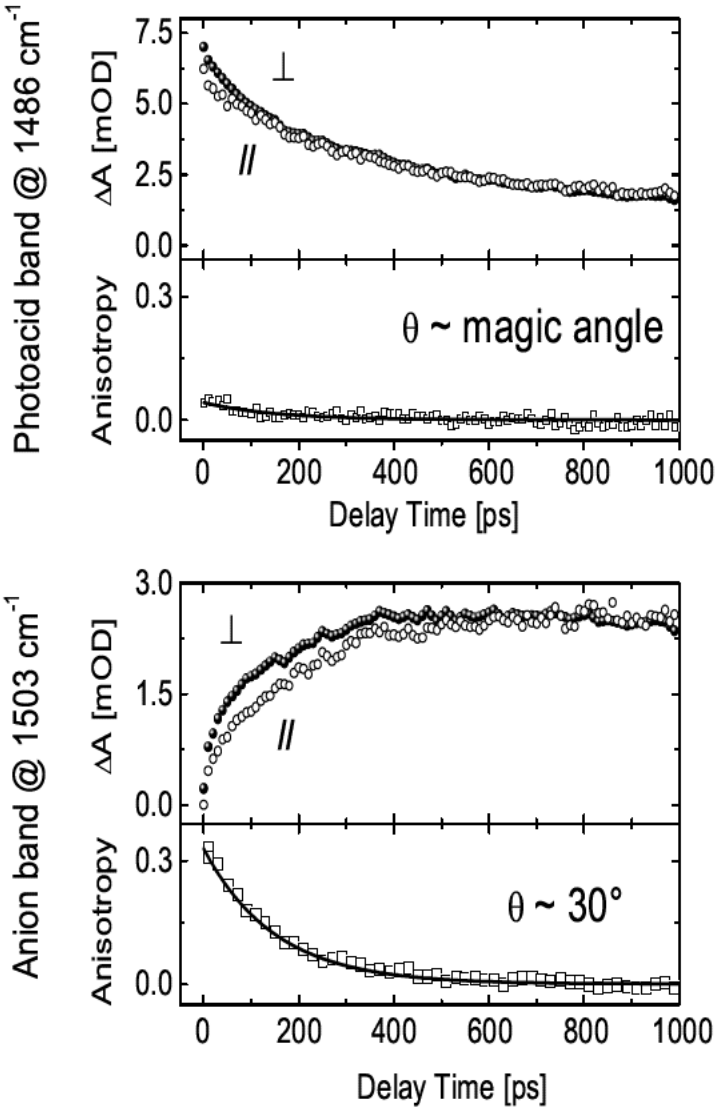

Figure 5.7: Transients at 1486 and 1503 cm^{-1} recorded for parallel and perpendicular polarizations, and calculated anisotropy $r = (N_{\parallel} - N_{\perp})/(N_{\parallel} + N_{\perp})$. From the value of the initial anisotropy, the relative angles between the optical transition dipole moment of the photoacid and the infrared transition dipole moments of either the photoacid or the anion in the S_1-state can be derived: $\lambda_{photoacid}$ (1486 cm^{-1}) = 50±5 degrees, λ_{anion} (1503 cm^{-1}) = 30 ± 5 degrees. The *magic angle* corresponds to 54.74 degrees.

of rotational relaxation that occurs on the same time scale. The pump-probe signals in presence of rotational relaxation have been described following the model proposed in Chapter 2, Section 2.5, assuming HPTS and its anion to be a symmetric rotor with identical rotational principal axes and identical rotational diffusion times τ_{rot}, using the expression 2.28 for the time-dependent rotational anisotropy $r(t)$. This approach can be justified by the fact that the photoacid and anion have almost identical structures, and that in both cases the SO^{3-} and OH/O^{-} moieties form hydrogen bonds with the surroundings. One can thus assume that rotational motion is not significantly affected by proton/deuteron transfer. A rotational diffusion time $\tau_{rot} = 1/6D_s = 150$ ps is obtained, as typical for molecules of similar size in water [42]. A similar value has been obtained for τ_{rot} of the HPTS anion by picosecond fluorescence spectroscopy [189]. The reaction dynamics have been described by standard expressions with a single exponential decay for the deuteron transfer. The measured pump-probe signals are affected by the contributions of the intrinsic deuteron transfer dynamics, the electronic population decay for the photoacid (4.8 ns) and the anion (5.3 ns), and the rotational anisotropy decay. Taking into account all these effects, the resulting time constant for the deuteron transfer reaction is of 250 ± 30 ps, in very good agreement with previous reports [187]. Within the assumption made, one derives a relative angle between the optical $S_0 \rightarrow S_1$ transition dipole moment of the photoacid and the infrared transition dipole moments of either the photoacid or the anion in the S_1-state to be: $\lambda_{photoacid}(1486\ cm^{-1}) = 50 \pm 5$ degrees, $\lambda_{anion}(1503\ cm^{-1}) = 30 \pm 5$ degrees.

Having grasped the essentials of the dynamics of the marker modes of HPTS photoacid and the anion in the case of deuteron transfer to the solvent, one can now focus the attention to the dynamics in the presence of the base acetate (Fig. 5.3, reactions II and III). For this study the reaction dynamics of the same two marker modes can be followed as well as the C=O stretching band of acetic acid located at 1720 cm^{-1} (see Fig. 5.6), as a function of the concentration of acetate. Detection of the transient C=O marker band is a direct indication of the fraction of acetic acid generated by deuteron transfer, since no other species (HPTS photoacid and conjugated photobase or acetate) contributes to the IR absorption in this frequency range. Figs. 5.8 and 5.9 summarize the experimental findings. As anticipated the deuteron transfer rates increase with increasing acetate concentration, a consequence of a decrease in the average diffusion times required for the acetate scavenger to encounter a HPTS photoacid molecule. One can monitor both the arrival of the deuteron at the base acetate (by following the rise of the acetic acid 1720 cm^{-1} band, Fig. 5.8) and the deuteron dissociation of the photoacid, by inspection of the rise of the anion 1503 cm^{-1} band (Fig. 5.9, lower panel), and of the decay of the photoacid 1486 cm^{-1} band (Fig. 5.9, upper panel). For concentrations of 2 M acetate or higher the anion band at 1503 cm^{-1} as well as the photoacid band at 1486 cm^{-1} are hidden behind strong acetate bands and cannot be reliably detected.

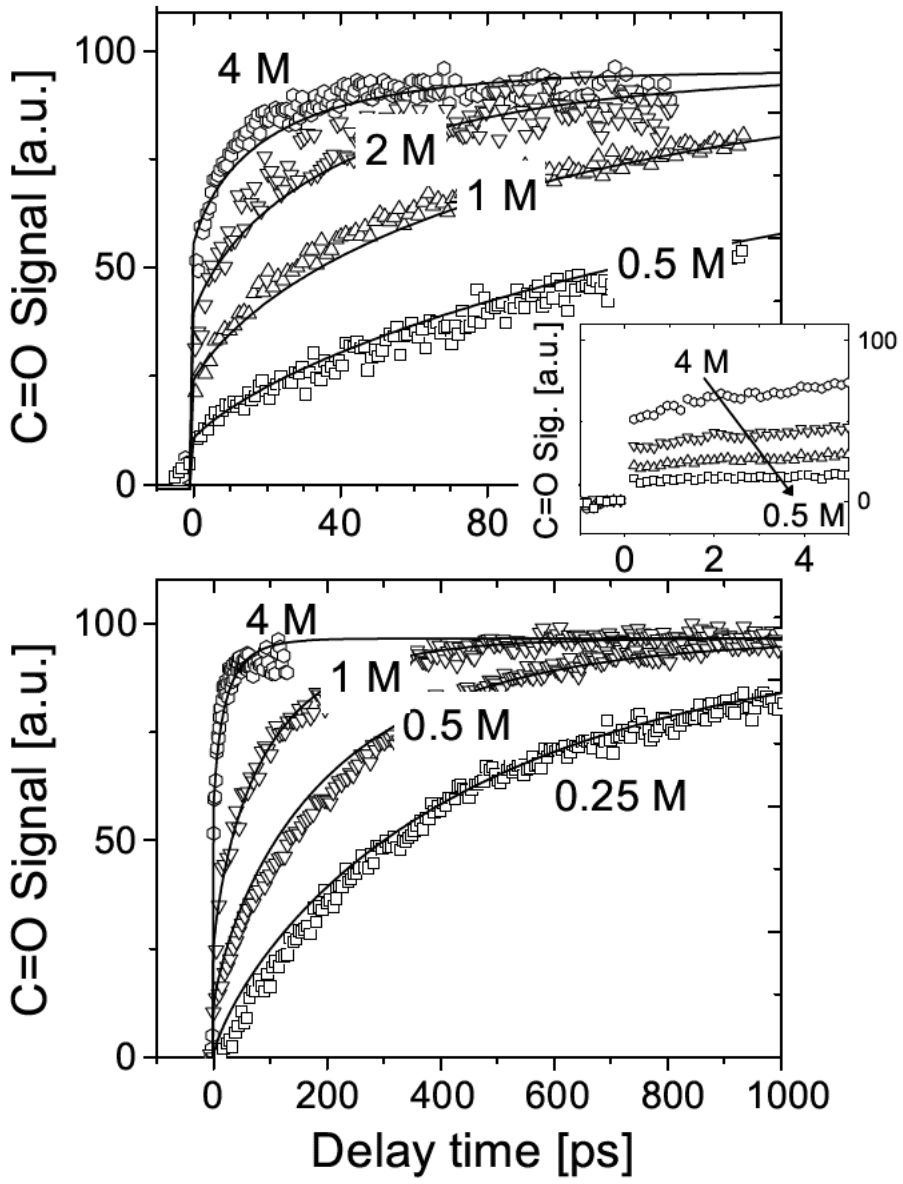

Figure 5.8: Transient experimental band intensities of the C=O stretch of the acetic acid as function of acetate concentration, together with traces calculated following the Szabo model with Collins-Kimball boundary conditions (see Section 5.3.2). The transients are plotted (A) over an extended scale of 160 ps (insert: zoom on the first 5 ps) and (B) over 1 ns.

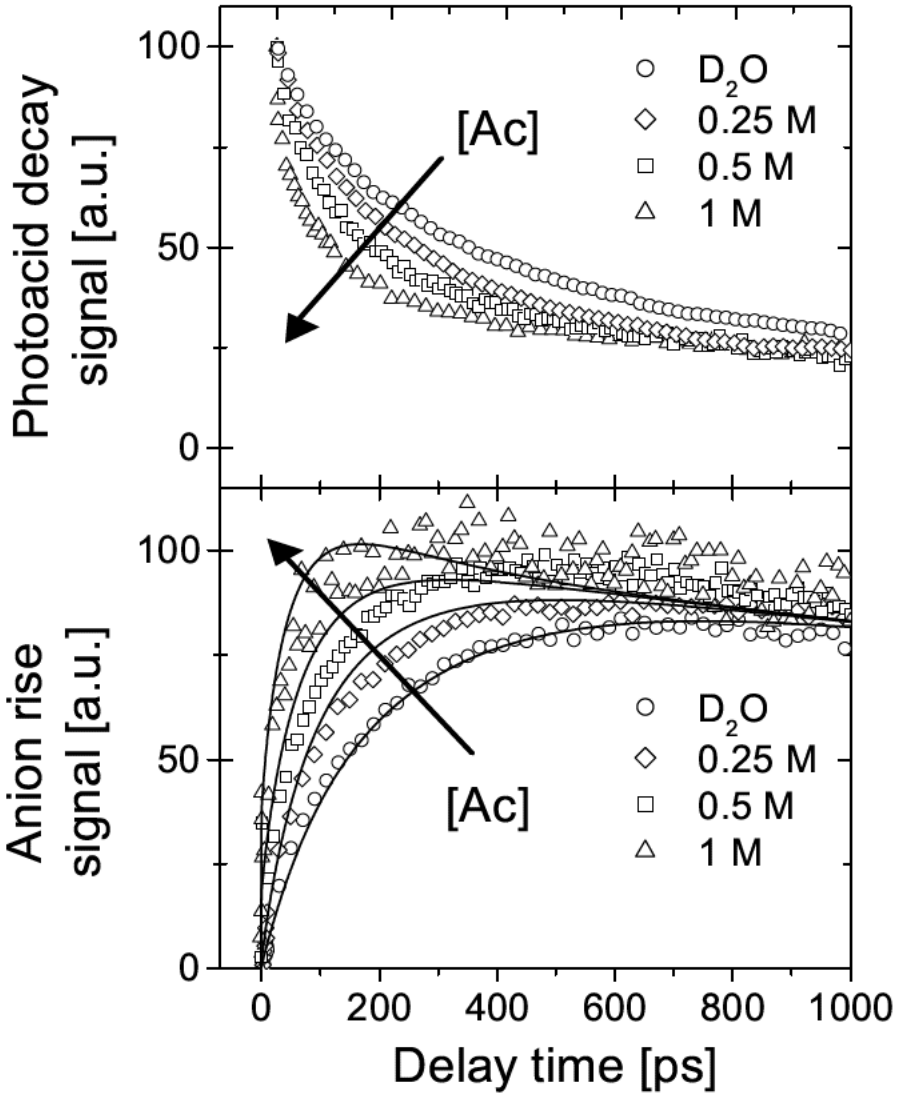

Figure 5.9: Transient experimental band intensities of the photoacid at 1486 cm^{-1} (upper panel) and of the anion at 1503 cm^{-1} (lower panel), together with traces calculated following the Szabo model with Collins-Kimball boundary conditions (see Section 5.3.2).

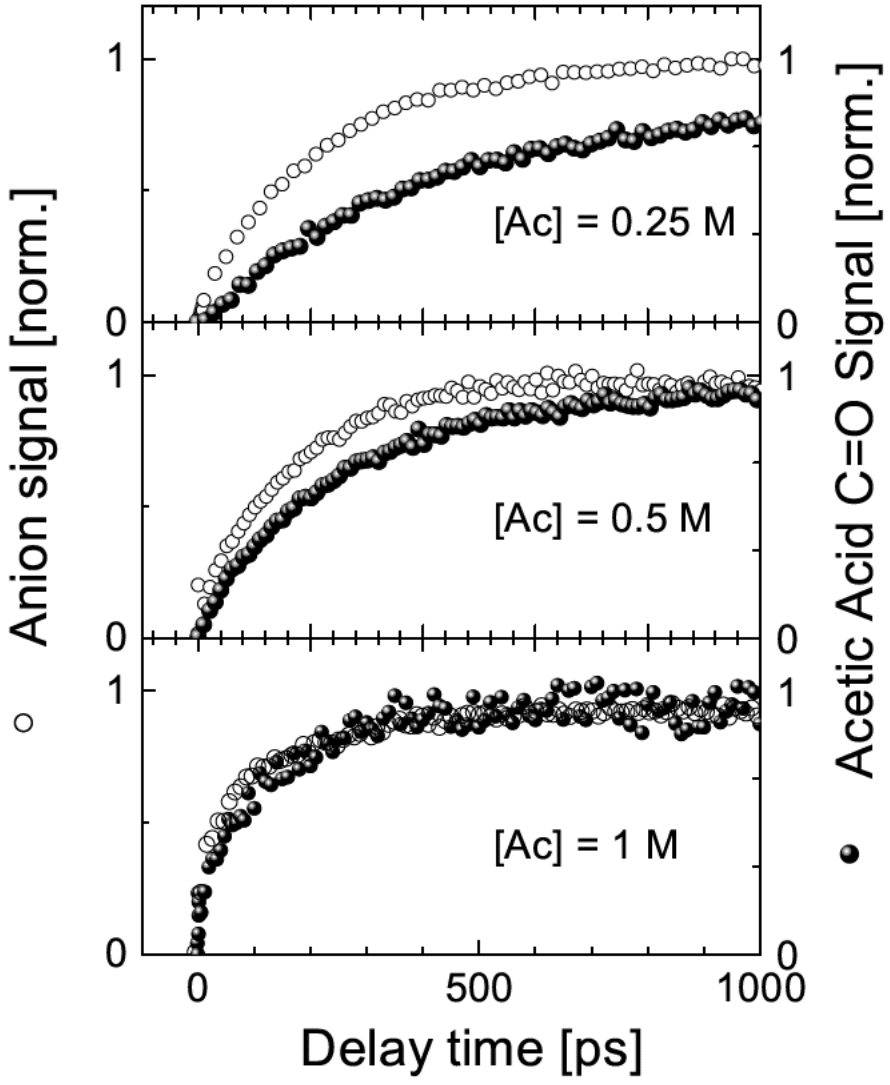

Figure 5.10: Comparison between the rise of the anion (photobase), corrected for rotational diffusion and electronic excited state decay (open symbols) and of the acetic acid (solid symbols) for increasing acetate concentration: 0.25, 0.5, 1 M. The experimental curves are normalized to have the same asymptotic value (for the 0.25 M case the asymptotic value of the C=O signal is reached after few ns). At lower concentrations the deuteron is first transferred to the solvent and subsequently picked up by the base, at concentration above 1 M the deuteron scavenging by the acetate base dominates the reaction dynamics and the anion formation coincides with that of the acetic acid.

It is interesting to compare measurements of the rise of the HPTS-anion band (at 1503 cm^{-1}) with the rise of the C=O band of acetic acid at (1720 cm^{-1}) at a specific acetate concentration (see Fig. 5.10). In order to directly compare the temporal behavior of both bands one has to correct the anion signals for the effects of rotational diffusion and electronic excited state decay, resulting in a rise only due to deuteron transfer dynamics. The comparison of the rise times of the HPTS-anion and the acetic acid signals reveals clearly that for concentrations of 1 M of acetate or higher, direct deuteron transfer to the base dominates the reaction dynamics. In contrast, for lower concentrations of acetate the HPTS-anion rises with faster pace than the acetic acid signal, indicating that deuteron transfer to the solvent occurs before deuteron pick-up by the base.

5.3.1 Proton transfer in hydrogen-bonded complexes

As appears from Figs. 5.6 and 5.8, for an acetate concentration above 1 M, a significantly large initial contribution to the transient C=O band, whose amplitude increases with the concentration, is generated within the experimental time resolution of 150 fs. Since the transient C=O stretching band signal does not alter its

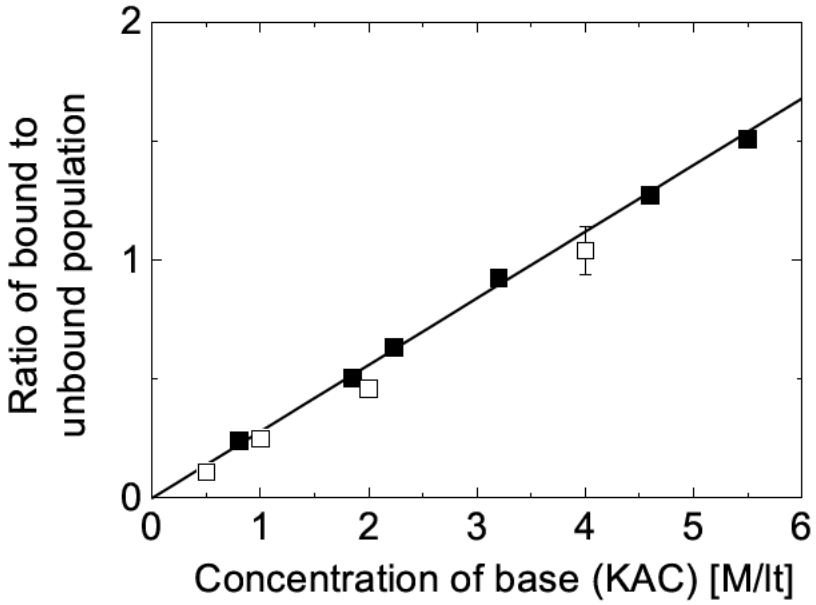

Figure 5.11: Ratio of H-bonded to unbound HPTS molecules as function of the salt concentration. Solid symbols: values obtained by analyzing solvatochromic shifts of the electronic absorption bands. Open symbols: values derived comparing the magnitude of the initial component relative to the total C=O signal.

magnitude and shape significantly within the first 1-2 ps, this initial contribution clearly reveals through its dynamics the different microscopic origin as opposed to the additional C=O signal that grows in with a time constant depending on acetate concentration (see Fig. 5.8). This initial component of the transient C=O stretching band signal is ascribed to the fraction of HPTS molecules that form a hydrogen-bonded complex with acetate when HPTS is in the ground electronic state. This fraction transfers its deuteron, after electronic excitation, to the associated acetate, at an ultrafast pace, not resolvable with a time resolution of 150 fs. When comparing the magnitude of the initial component relative to the total C=O signal that is generated (relative fraction 0.54 for an acetate concentration of 4 M, 0.39 for 2 M, 0.24 for 1 M and 0.11 for 0.5 M; no detectable fraction observed for 0.25 M), one derives a complexation constant for HPTS and acetate of 0.28. This same value is obtained by analyzing solvatochromic shifts of the electronic absorption bands of HPTS as function of acetate concentration [190], as shown in Fig. 5.11.

At this point, one should mention that judging the presence of hydrogen-bonded complexes from the analysis of solvatochromic shifts of the electronic absorption bands gives a rather indirect proof. A more direct and easily recognizable signature of hydrogen bonding is represented by the spectral effects on the OH (OD in this case) stretching band [13]. Nevertheless, this approach is not practicable here, due to the fact that the OD stretch of the solvent dominates the absorption in this spectral region and to the difficulty of distinguishing, under this condition, the effects due to the hydrogen-bonding to water and those due to the hydrogen-bonding to the acetate. On the other hand, the HPTS molecule has been used in a multitude of applications (e. g. as sensor of pH [191], carbon dioxide [192] and ammonia [193], as a pH probe of liposome interiors [194] and reversed micelles [191]) and the solvent effects on the fluorescence and absorption spectra of this molecule are well known [195]. The proposed hypothesis that explains the solvatochromic shift of HPTS observed in water-acetate solutions in terms of a specific hydrogen bond to the acetate seems reasonable and, together with the findings of this work, forms a very consistent picture (see Fig. 5.11).

Such a fast bimolecular reaction rate is more than one order of magnitude larger than previously reported [181]. Since the deuteron transfer reaction dynamics occur at such a fast pace, it is highly likely that the HPTS-acetate “tight" complex observed at high acetate concentrations is made up by a direct hydrogen-bond between the photoacid and the base of the type $A^-H^+ \cdots B$, with water solvent molecules present only in the outer sphere of the complex. Direct hydrogen-bonded complexes are typical of relatively non-polar environments not rich with water molecules. Aqueous solutions of acetate salts in excess of 1 M concentration appear to resemble water-deficient environments as far as their solvation abilities are concerned. At lower concentrations of acetate salts, aqueous solutions retain their bulk properties and fully solvate the acid and base molecules.

5.3.2 Diffusion limited proton transfer

The slower, concentration-dependent dynamics of the C=O signal are ascribed to the fraction of HPTS molecules that are initially uncomplexed in the ground state, and that upon electronic excitation to the S_1-state will either, depending on the acetate concentration, transfer the deuteron to a nearby acetate molecule that has diffused to form an encounter complex with HPTS, or to the solvent D_2O, after which the deuteron will be ultimately picked up by an acetate ion. As mentioned before, for concentrations of 1 M of acetate or higher, direct deuteron transfer to the base dominates the reaction dynamics (see Fig. 5.10).

The observed diffusion-limited component of the bimolecular reaction can be analyzed using a model for diffusion-influenced reactions based on the Smoluchowski approach [184]. Within the Smoluchowski framework, theoretical treatments of important classes of bimolecular reactions have been developed, allowing to better distinguish the role of diffusion from that of the intrinsic reaction. Examples include processes like diffusion-influenced fluorescence quenching [185] and diffusion-controlled electron transfer reaction [196]. According to the conventional Smoluchowski formulation, the reaction between the photoacid HPTS and the acetate:

$$\mathrm{ROH}^* + \mathrm{B}^- \rightleftharpoons \mathrm{RO}^{-*} + \mathrm{BH}$$

can be described assuming that the survival probability $S(t)$ of the ROH* species, surrounded by a distribution of acetate anion of concentration c, satisfies the following equation:

$$\mathrm{d}S(t)/\mathrm{d}t = -c \cdot k(t) S(t) \tag{5.1}$$

where $k(t)$, referred to as the "time-dependent rate constant" is derived from the solution of the Debye-Smoluchowski diffusion equation for the reactants. Fig. 5.12 shows a scheme of the problem.

The reacting species ROH* is a triply negatively charged molecule, the base has a negative charge. Overall the solution is electrically neutral, containing K^+ and Na^+ cations coming from the dissociation of potassium acetate and HPTS respectively. In the Smoluchowski approach, reaction is assumed to occur in two steps: (i) The reactants mutually diffuse until their distance equals a *contact radius* R^*. (ii) The reaction occurs at contact with a finite rate k_r.

For an arbitrary interaction potential between the reactants, the Smoluchowski equation cannot be solved analytically. An approximate expression for the time-dependent rate constant has been derived by Szabo using the Collins-Kimball radiative boundary conditions at contact [185]:

$$k(t) = \frac{k_D k_r \mathrm{e}^{-\beta U(R^*)}}{k_D + k_r \mathrm{e}^{-\beta U(R^*)}} \left[1 + \frac{k_r \mathrm{e}^{-\beta U(R^*)}}{k_D} \mathrm{e}^{\gamma^2 D t} \mathrm{erfc}\left(\sqrt{\gamma^2 D t} \right) \right] \tag{5.2}$$

where erfc is the complementary error function, $U(R^*)$ is the interaction potential between reactants calculated at a distance equal to the contact radius, $R^* = 6.3$ Å

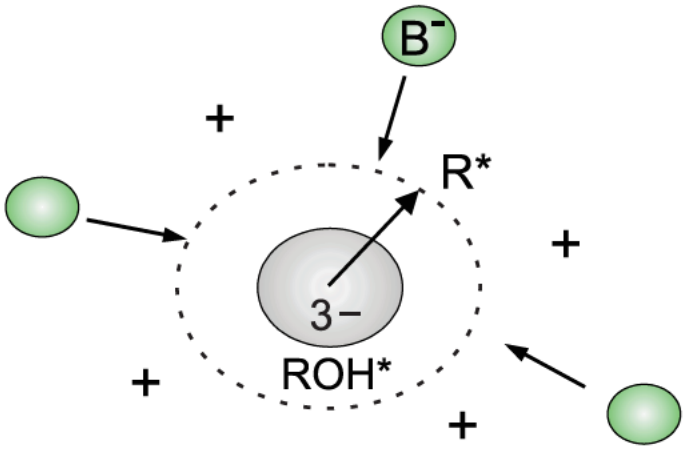

Figure 5.12: Scheme of the problem. The excited ROH* is triply negatively charged, the base has a single negative charge. Reaction occurs at a contact radius R^*.

is the contact radius, $\beta = 1/k_B T$ (k_B is the Boltzmannt's constant, $T = 300$ K the absolute temperature). The parameters D, γ and k_D depend on the concentration of the acetate base in the experiments. Their values are collected in Table 5.3.2 and are taken from literature data [181]. D is the relative diffusion coefficient ($D = D_{ROH} + D_B$), k_D is the diffusion-controlled rate constant [163, 197].

Table 5.3.2: Concentration-dependent fitting parameters.

Salt concentration [M]	D [10^{-9}m^{2}s^{-1}]	k_D [10^{-9}M^{-1}s^{-1}]	γ [10^{-9}m^{-1}]	Complexed fraction
0.25	1.26	6.01	9.51	–
0.5	1.23	5.87	9.71	0.11
1	1.15	5.48	10.27	0.24
2	0.98	4.67	11.78	0.39
4	0.6	2.86	18.23	0.54

For the deuteron transfer rate k_r (actually the only fitting parameter) a value $k_r = 3 \cdot 10^{10}$ M^{-1}s^{-1} was used. The ultrafast component of the dynamics due to the fraction of initially hydrogen-bonded HPTS-acetate complexes is described by a step-function in time. The electrostatic repulsive potential $U(r)$ between HPTS and acetate is assumed to be fully screened at above-molar salt concentrations ($U(r \geq R^*) = 0$; $U(0 \leq r \leq R^*) = \infty$).

The rise of the anion signal (see Fig. 5.9) is governed by the reaction dynamics,

electronic population decay and rotational diffusion. All these effects as well as the competing deuteron transfer to the solvent have been incorporated in the model. On the other hand, the rise of the acetic acid signal (see Fig. 5.8) is only determined by deuteron transfer to base, and thus directly controlled by either the direct transfer in the HPTS-acetate “tight" complex or by diffusive dynamics for the other component in the observed signals. With this model it is assumed that any excited photoacid will transfer its deuteron either to the solvent or the base, where any deuteron released to the solvent eventually will be picked up by the base. Further improvements can be made when considering electrostatic screening between the reaction partners that is of course dependent on the base concentration.

At this point, one should highlight the approximation contained in this approach. In the description of diffusion-influenced bimolecular reactions one is faced with a many-particle problem that can be solved only in special cases and with several limitations. The calculation of the interaction potential $U(r)$ in the ionic solution is in itself a challenging problem, usually approached within the Debye-Hückel theory of ionic solutions (a full screened potential has been used here, using a Debye-Hückel formalism gave similar results). However, for an arbitrary interaction potential between the reacting species $U(r)$, the Smoluchowski treatment is exact under two conditions [185]: (i) The diffusion coefficients of the ROH^* species must be close to zero. In other words, when the ROH^* species can be described as static targets towards which the species B^- diffuse. This is probably a justified assumption in this case, given the difference in size between the HPTS molecules and the small and fast diffusing acetate bases. (ii) The interactions between the B's must be negligible. The Smoluchowski model only considers the RO^*-B^- interactions and assumes that the motion of the B's is not correlated. This can be the most serious limitation, especially at high salt concentrations where the average distances between base molecules are on the order of few tens of Å.

Nevertheless, the calculated response for the rise of the acetic acid and anion signals appears to mimic the measured signals in a consistent way, considering the drastic assumptions made. A comparison with the experimental curves in shown in Figs. 5.8 and 5.9. Discussing the validity of the Smoluchowski approach for the description of diffusion-influenced reactions is beyond the scope of this work.

5.4 General mechanism for an acid-base reaction

According to Eigen [198, 199] and Weller [94] general acid-base reactions in solutions being bimolecular in nature, consists of (i) diffusional motion, where the acid and base approach each other to form an encounter pair where the mutual distance equals the contact radius, followed by (ii) intrinsic proton transfer (iii) subsequent diffusive separation. The theoretical interest focusses mainly on step

(ii) in the reaction dynamics and on whether the reaction rate is determined by activated dynamics of the proton over a reaction barrier [200–202], or by proton tunneling motion through the barrier [203], or even concern a dominant role of the solvent motions that accompany the proton transfer [204]. However, since the diffusion rates are typically much slower than the on-contact proton transfer rates, a direct access to the actual proton transfer reaction dynamics between freely diffusing acid and base molecules in liquid solution remains problematic. The obvious way the eliminate the diffusive aspect is to study acid-base complexes, that are in direct contact to each other. Real-time observation of proton transfer is only possible when acid and base reach contact at a well-defined point in time, and this is hard to reach for a macroscopic ensemble of standard acid-base pairs.

With ultrafast ultraviolet pump/mid-infrared probe spectroscopy it is possible to trigger a switch in the acidity of a photoacid and to monitor the dynamics of deuteron transfer reactions both at the donor and the acceptor sides. The data show clearly two aspects. In the case where, in the ground state, non-reactive “tight" photoacid-base complexes are prepared, that are linked by a specific intermolecular (weak) hydrogen bond, an ultrafast, non-diffusion limited deuteron transfer occurs, on a time scale which is too fast to be measured with an experimental time resolution of 150 fs. In contrast, slower, concentration-dependent dynamics are found to characterize those reactions occurring by diffusion of the reactants to form a complex prior to reaction.

The dynamical model emerging from these observations points to a three stage reaction-scheme for acids and bases forming encounter-pairs in water-rich environments (Fig. 5.13). Initially, diffusion allows the acid and the base to form a “loose" complex, each retaining its water solvation shell, at a contact-distance R^*. The reaction continues to be driven downhill, but now at the expense of the solvation energy of the solvent that needs to at least partially desolvate (or ’rearrange’) the acid and base pair before they can further approach each other. This stage that occurs within the contact volume has a reaction barrier in the solvent and is relatively slow as compared to the final reaction stage of proton transfer along the hydrogen bond connecting the acid with the base. The final reaction stage of proton transfer is so fast as to be considered instantaneous with respect to the first two stages of the reaction.

The deuteron transfer dynamics of the slower, diffusion-limited component appear to have a finite “on contact" rate of 8 ps^{-1}, at least one order of magnitude slower than the rate found for the hydrogen-bonded HPTS-acetate complex. The reason for this much slower “on contact" reaction rate may lie in the fact that the solvent shell reorganization of HPTS and acetate occur on this time scale [205]. This reorganization of the solvent constitutes, in the scheme of Fig. 5.13, what is defined as the “Encounter stage" which precedes the formation of a direct hydrogen bond complex with subsequent deuteron transfer. The solvent rearrangement (with a rate k_{SR} being the rate-limiting step) leads then to the

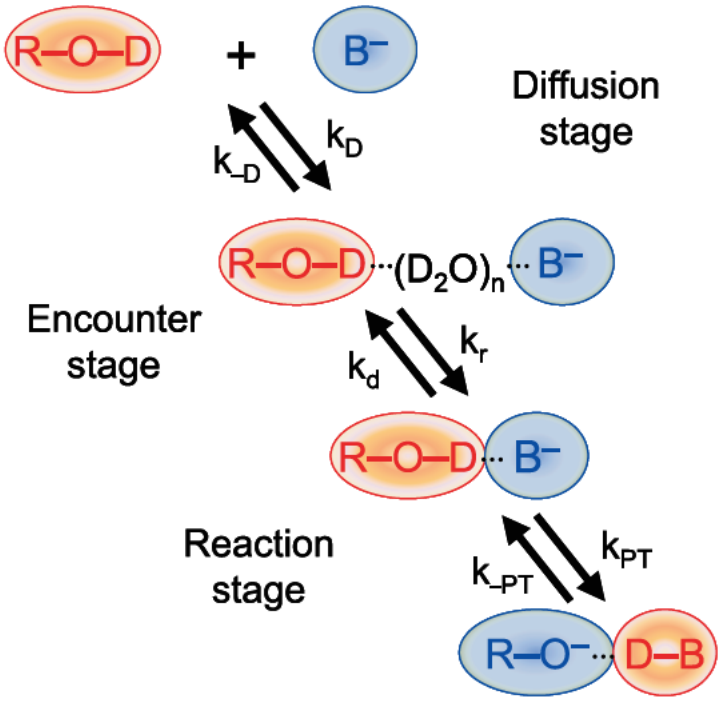

Figure 5.13: Three-stage reaction mechanism for a general acid base reaction.

formation of a direct complex, before the actual deuteron transfer can occur with a rate constant $k_{direct} < 150$ fs. The processes following the formation of a "loose" complex after diffusion could be then schematized in the following way:

$$\mathrm{R-OD\cdots[D_2O]_n\cdots B^-} \underset{k_{-SR}}{\overset{k_{SR}}{\rightleftarrows}} \mathrm{[R-OD\cdots B]^-} \xrightarrow{k_{direct}} \mathrm{[R-O\cdots DB]^-} \underset{k'_{-SR}}{\overset{k'_{SR}}{\rightleftarrows}} \mathrm{R-O^-\cdots[D_2O]_m\cdots DB}$$

An alternative and suggestive option could also explain consistently the experimental data, whereby the deuteron transfer in dilute aqueous solutions does not require to form a direct acid-base contact pair but is rather a through-

solvent mechanism ("von Grotthuss" [150, 151]) involving few neighboring water molecules:

$$R-OD\cdots\left[D_2O\right]_n\cdots B^- \xrightarrow{k_{Grotthuss}} R-O^-\cdots\left[D_2O\right]_n\cdots DB$$

The rate-limiting step $k_{Grotthuss}$ would in this case be due to the "von Grotthuss"-type transfer of protons (deuterons in this case). This conduction mechanism is usually described in terms of "structural diffusion", i. e. propagation of a "structural defect" between adjacent water molecules, rather than as the motion of an isolated ion through the solvent [150, 151].

Chapter 6

Ring opening reaction of photochromic compounds

6.1 Introduction

Photochromic compounds have the property that they change color after the absorption of light of specific wavelengths, as a consequence of a reversible transformation between two isomeric forms, which differ from one another in various properties (e.g. the absorption spectra, dielectric constants etc). In addition, for a compound to be photochromic it is necessary that this color change can also be reversed by exposure to light, yielding again the original substance (see Fig. 6.1).

Although more than 100 years have passed since its discovery, photochromism continues to generate much scientific interest, both in academic and industrial research groups [206–221]. Wide applications are envisaged for photochromism, including optical data storage [207], displays [208] and optically controlled molecular switching [209] that ultimately may drive developments in molecular nanotechnology [209]. For applications to actual devices, photochromic systems should also fulfill several conditions: thermal stability of both isomers, rapid response, high sensitivity, nondestructive readout capability.

Research has been concentrated on a relatively small number of compounds. In particular, four photochromic systems have been extensively studied: azobenzenes, spiropyrans, fulgides and diarylethenes [206–208]. In azobenzene, the photochromic properties arise from the cis-trans isomerization of the N=N bond. The ring opening reaction induced by the photoexcitation is responsible for the property change of spiropyran derivatives. In fulgides and diarylethens electrocyclic ring-closure reactions occurring in the excited state are the origin of photochromism; in these compounds the photochromic properties are thermally irreversible [208]. Many of the features of the reactions of these compounds have been well established and evidence concerning the nature of the structure and

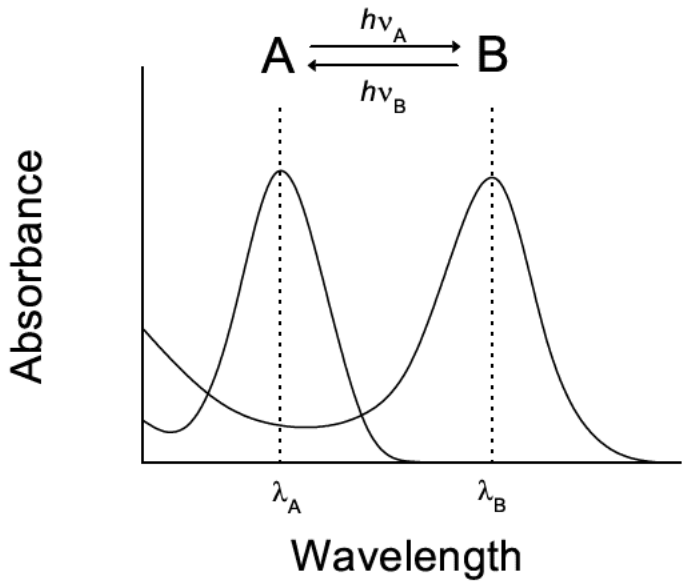

Figure 6.1: Photochromism: reversible photo-induced transformation of a chemical species between two states having distinguishable absorption spectra.

properties of the colored and the uncolored forms have been obtained by means of a variety of experimental techniques (e.g. ultraviolet, visible, infrared and NMR data, dipole moment determinations, evaluations of kinetic, equilibrium and thermodynamic constants, studies of the effects of substituents on the reactions). From a scientific and technological standpoint it is relevant to map reaction pathways and efficiencies, and to identify intermediates involved in the switching between the different photochromic isomers. The quick response and high reaction yield of a photochromic system are of special importance: the reaction in the excited state will generally occur in competition with other non desirable processes, such as radiative (fluorescence and phosphorescence) and non-radiative (internal conversion and intersystem crossing) transitions, quenching reactions with energy transfer to other molecules, etc.

Time-resolved laser spectroscopy provides excellent tools to shed light on the dynamics of photochromism. The majority of time-resolved investigations of photochromism, from femtosecond to millisecond timescales, so far focuses on the evolution of the electronic absorption bands responsible for the color changes. Although such investigations have been paramount to the advancement of understanding reaction mechanisms in general, and photochromic reactions in particular, complications may occur if the complexity of the reaction increases, due to formation of several different isomers and involvement of numerous electronic

states. In these situations electronic absorption bands of different species may significantly overlap, or go unnoticeable if the oscillator strength of electronic transitions in different species differs considerably. Femtosecond time-resolved vibrational studies open a new window on the dynamics from a different perspective: the evolution of the vibrational absorption spectrum. Vibrational IR absorption lines are typically very narrow, and thereby increase the chances of finding regions where different lines do not overlap. Moreover, certain IR absorption regions are known to correspond to specific structural molecular features and therefore monitoring the time dependence of the vibrational spectrum offers better chances for obtaining detailed information on changes in the spatial structure of the molecule.

This chapter reports the investigation with $\sim$ 100 femtoseconds time resolution of one of the most studied photochromic reactions [206–221]: the spiropyran-merocyanine chemical ring opening/closure reaction (see Fig. 6.2). The photochemical ring opening reaction of a spiropyran molecule is initiated by femtosecond UV pump pulses, and the time-evolution of the vibrational absorption spectrum towards the formation of merocyanine product species is directly followed by probing with mid-IR pulses. Given the enormous research effort on these systems and the importance of understanding the ultrafast steps of the reaction, it is remarkable that up to now only a handful of studies have been performed with sub-nanosecond time-resolution [210–216]. The experimental results reported here have helped developing a clearer picture of these reactions by solving some ambiguities present in the literature concerning the reaction dynamics, addressing the existence of different merocyanine isomers and providing insight into the competing internal conversion process, which was never mentioned in previous investigations as a rather influential decay channel and may result to be the most important factor in determining the overall quantum yield of the photochromic reaction.

6.2 Photochromic spiropyrans

Two spiropyran systems were investigated: 1',3',3',- trimethylspiro -[-2H-1- benzopyran -2,2'- indoline], commonly referred to as BIPS, and a derivative of BIPS, 1',3'- Dihydro -1',3',3'- trimethyl -6- nitrospiro [2H-1- benzopyran -2,2'-(2H)- indole], referred here as 6-nitro-BIPS, which has a nitro substituent on the benzopyran ring. The spiropyran compound can to first approximation be regarded as two nearly independent orthogonal halves [217]: a chromene and an indoline unit. In the ground state, the BIPS and 6-nitro-BIPS molecules do not absorb in the visible (cf. Fig. 6.3). Upon absorption of a UV photon a ring opening and cis-trans isomerization take place, resulting in a more or less planar molecule with a strong broad absorption around 540 nm. The huge shift in absorption wavelength can easily be understood from the fact that now the delocalized π-system

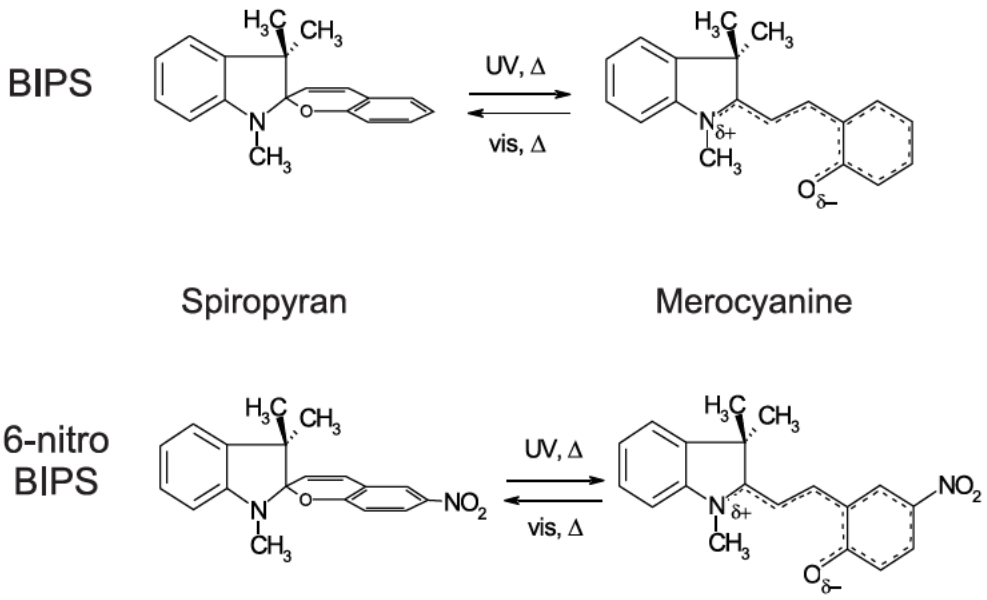

Figure 6.2: Reactant and product structures for the photochromic reaction of BIPS (top) and 6-nitro-BIPS (bottom).

extends over the entire molecule.

A consistent fraction of the experimental work found in the literature has concentrated on nitro-substituted spiropyrans, such as 6-nitro-BIPS, since these compounds have a higher quantum yield for the photochromic reaction that makes them more interesting for applications [211]. It has been concluded that if the chromene part contains an NO_2 substituent the ring opening reaction of spiropyrans will (at least to some extent) involve triplet states [218]. For spiropyran compounds without this NO_2 substituent, such as the one investigated here, it has been stated [211] that the reaction involves only singlet states. The addition of the nitro substituent as a way to obtain more efficient photochromism has been ascribed to two reasons [208, 222]: first, it was suggested that the nitro group increases the quantum yield of photochromism by introducing a triplet pathway; second, it stabilizes the zwitterionic merocyanine form of the molecule, so that the thermal back reaction is slowed down. However, it introduces other technical problems because it affects the photochemical stability. The participation of the triplet pathway in the 6-nitro-BIPS derivatives was shown by triplet sensitization [223] and transient absorption spectroscopy [215, 224, 225], suggesting that for nitro-substituted spiropyrans, merocyanines are formed both from singlet and triplet manifolds. Analyzing the oxygen effect on transient absorption, it was proved that, in contrast to the nitro-substituted spiropyran derivatives,

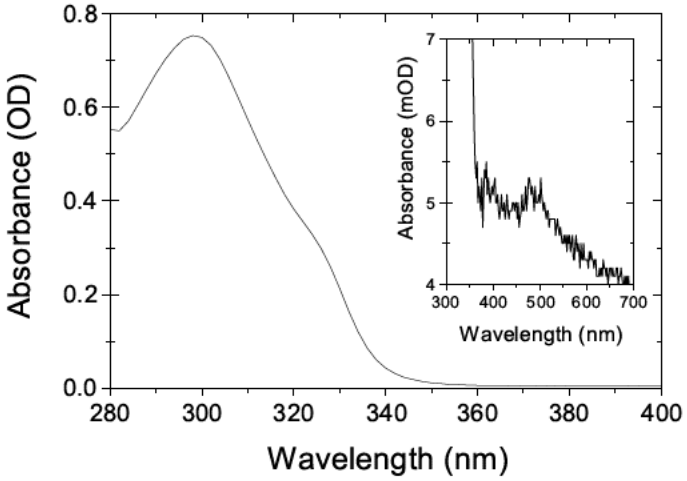

Figure 6.3: Absorption spectrum of BIPS in tetrachloroethene (C_2Cl_4). The insert illustrates the nearly complete absence of merocyanine absorption around 540 nm.

indolinospiropyrans without nitro-substitution show photochromism only in the excited singlet manifold. Introduction of the nitro group also gives rise to the possibility of hydrogen bond formation between the NO_2 group and hydrogen-bond-donor solvents [226].

The open merocyanine form of the molecule possesses a central chain of three carbon-carbon bonds, C_2-C_3-C_4-C_{4a} (cf. Fig. 6.2). Any geometrical arrangement may be described by the three associated dihedral angles α, β, and γ. In the electronic ground state, the merocyanine molecular structure confers partial double-bond character to each of the bonds of the central chain, so that each dihedral angle will be close to either 0°or 180°, corresponding to a cisoid or transoid configuration of the particular chain segment [220]. Hence, in principle eight isomers can be formed of the merocyanine compound, due to cis-trans configurations at the three double bonds of the bridge segment. Theoretical calculations have indicated however that due to steric hindrance only isomers with a trans configuration around the second bond are stable [212].

6.3 Ring opening reaction of BIPS

Femtosecond UV-pump/white-light probe experiments have been performed at room temperature on BIPS in ethanol [210] and n-pentane [211, 212], and on the naphthopyran analogue [211, 212] naphtho-BIPS and 6-nitro-BIPS in n-pentane [211]. These data demonstrated the appearance after about a picosecond of a

broad nearly featureless absorption, covering the entire probing range of 380-680 nm. At the wavelengths of the merocyanine product absorption band, the rise time [211] in n-pentane was 0.9 ps for BIPS (at 540 nm) and 1.4 ps for naphto-BIPS (at 520 nm). During the following 6 ps the absorption at the maximum did not change drastically, however the featureless initial spectrum did evolve towards sharper spectral features that more closely resemble the product spectra observed on μs time-scales [211, 212]. The broad initial absorption and subsequent sharpening was ascribed to transitions from the spiropyran excited state to higher electronic states, and to transitions from vibrationally hot merocyanine in the electronic ground state [211]. For the 6-nitro-BIPS compound the initial spectrum was similar. However, at later times two absorption bands, at 430 nm and 575 nm, increased in intensity with a 20 ps time constant [211]. Room temperature experiments with femtosecond UV-pump and probing at diverse wavelengths in the visible have been performed on 6-hydroxy-BIPS in 1-propanol, methanol, and 1-hexanol [213]. Pumping at 310 nm and probing at 620 nm an exponential rise of the signal with $\leq$2 ps was identified in 1-propanol. The general conclusion from these experiments seems therefore that the merocyanine product is formed with a 1-2 ps time constant in the compounds without a nitro-group, and with a 20 ps time constant for 6-nitro-BIPS. The nearly featureless absorption after 1 ps, covering at least the range of 380-680 nm [211], was the motivation to undertake the present UV pump/mid-IR probe studies. Electronic transitions of molecules in solutions are typically significantly broadened by optical dephasing and inhomogeneity effects. Therefore, at every wavelength several different vibronic and/or electronic states contribute to the absorption, resulting in smooth broad spectral features.

In contrast, vibrational IR absorption lines are typically very narrow and without much inhomogeneous broadening. Although the large number of vibrations for larger molecules can also be complicating, there are still good chances of finding regions with relatively few IR absorption lines. In addition, no time-resolved single color UV experiment has yet been reported to directly determine whether any recovery of the spiropyran (closed form) absorption occurs. Such a measurement is essential for obtaining quantitative information on the quantum yield of this photochemical reaction. This information will be extracted here from the time evolution of bleaches related to the IR vibrational absorption spectrum of the spiropyran compound. Vibrational spectroscopy can increase the insight in the possible existence and structure of reaction intermediates, the time scale(s) of product formation, and whether different isomers are being formed on femtosecond and picosecond time scales. The FT-IR spectrum of BIPS in tetrachloroethene, and existing resonance Raman spectra on the photoproducts of BIPS in different solvents [221] taken 200 ns after UV excitation, are used to support the analysis.

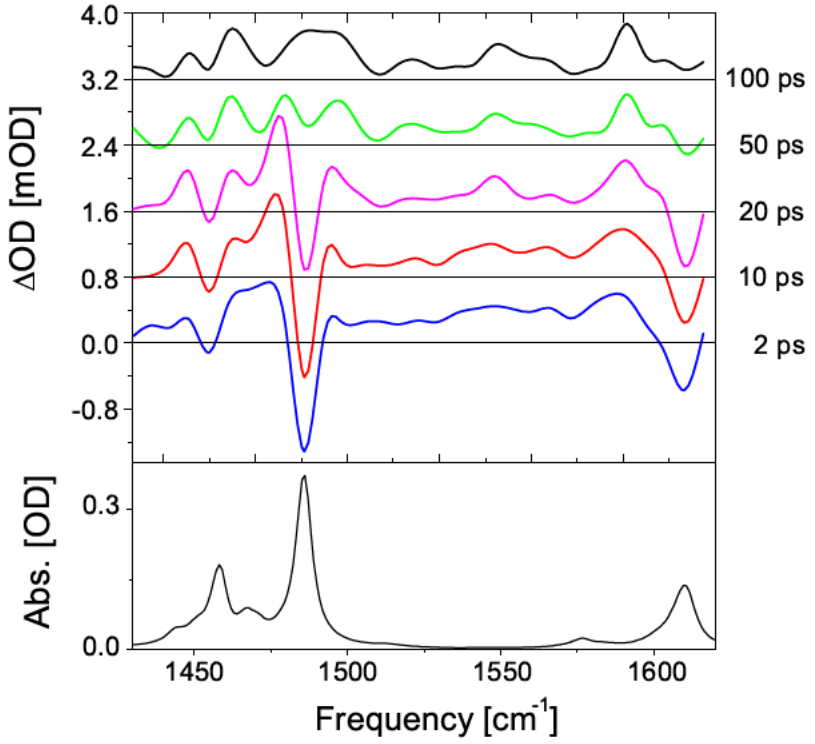

Figure 6.4: Upper panel: Transient changes in the IR absorption spectrum between 1430 and 1620 cm^{-1} at 2, 10, 20, 50, and 100 ps (from bottom to top) after UV excitation at 316 nm. For representation purposes the signals are displayed with the offset at consecutive delay times increased in steps of 0.8 mOD. The dashed lines indicate the zero signal level for the different traces. Lower panel: Steady-state IR spectrum of 50 mM BIPS (closed form) in tetrachloroethene.

6.3.1 Experimental results

The absorption spectrum of 1 mM BIPS in a 1 mm quartz cuvette was recorded in a Perkin-Elmer UV-VIS spectrometer. Below 280 nm strong absorption from the solvent C_2Cl_4 (tetrachloroethene) prevents an accurate determination of the absorption spectrum. Steady-state FT-IR spectra were recorded with 2 cm^{-1} resolution, using a Biorad FT-IR spectrometer. The 50 mM sample of BIPS in C_2Cl_4 was injected in a home-built cell with CaF_2 windows and a spacer of approximately 100 μm. For the femtosecond pump-probe experiments a 21 mM solution of BIPS in C_2Cl_4 was used, and pumped through the 100-μm free streaming jet. In these experiments, the excitation wavelength was tuned to 316 nm, the pulse energy was 2.5 μJ and the pulse duration around 70 fs. The center

frequency of the mid-infrared probe pulses was tuned to 1530 cm^{-1} and the output energy was about 700 nJ. Under these experimental conditions, the detection of absorption changes as small as 0.10 mOD was feasible, with an accuracy of ±0.05 mOD. The experimental curves presented here are the average of 15-25 time delay scans, with each scan averaging 400 shots per data point. The time-resolution was of 130 fs (FWHM).

The spectral evolution of the transient changes in optical density (OD) of the IR absorptions between 1430 cm^{-1} and 1620 cm^{-1} during the first 100 ps after excitation of BIPS at 316 nm is illustrated in the upper panel of Fig. 6.4. For comparison the IR absorption spectrum of BIPS in the electronic ground state, at a concentration of 50 mM in C_2Cl_4, is depicted in the lower panel of Fig. 6.4 over the same frequency range. The entire spectral range from 1200 to 1800 cm^{-1} was investigated, but it did not provide additional information. The presented range contains the strongest IR band, as well as the most isolated IR band. Note furthermore that the merocyanine compound does not exhibit a true carbonyl stretching mode in the range 1600-1800 cm^{-1}, probably because it is part of the delocalized π-system.

The spectrum after 2 ps is dominated by strong bleaches of the ground state IR absorption bands at 1458, 1486 and 1610 cm^{-1}. For the data in Fig. 6.4 each detector pixel integrates signal over a range of 6 cm^{-1}. This implies that for vibrational bands broader than 6 cm^{-1} the peak position of bands can be determined within 4 cm^{-1}. The calibration of the grating spectrometer was checked by comparing the positions of the bleaches to those observed in the steady-state FT-IR spectrum. In addition, weak transient (increased) absorption is seen at most other frequencies. Between 1535 and 1585 cm^{-1} most of this absorption (amplitude ranging from 0.1-0.4 mOD) disappears with time constants ranging from 2-22 ps, leaving a residual change in absorbance (ΔOD) varying between 0.06 and 0.20 mOD (accuracy ±0.05 mOD). The height of this residual offset was found to depend clearly on the duration of the UV pulses and is ascribed to minor undesirable multiphoton contribution from BIPS molecules and the solvent. After 100 ps the strong bleaches have nearly entirely recovered, indicating that the majority ($\geq$ 90%) of the BIPS molecules have by that time returned to the vibrational and electronic ground state of the closed spiropyran form. At this time delay product vibrational absorption bands can clearly be identified at 1461 cm^{-1} (0.6 mOD), 1489 cm^{-1} (0.6 mOD), and 1591 cm^{-1} (0.6 mOD).

6.3.2 Discussion

(i) Kinetic scheme for analysis of the time-resolved data. The kinetic scheme shown in Fig. 6.5 is used for the data analysis. The assignments are defined in the following. This scheme assumes that the initial species generated by UV photoexcitation is the excited singlet state of spiropyran, $SP(S_1)$. This either

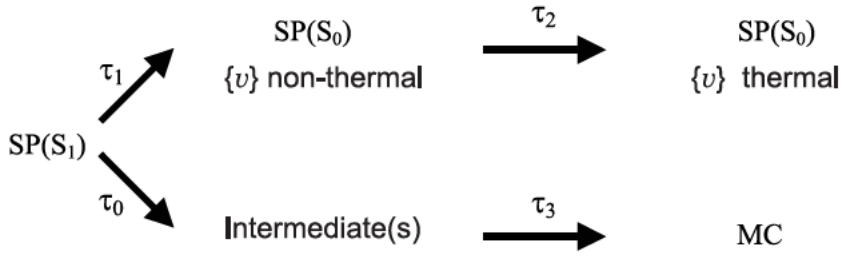

Figure 6.5: Kinetic scheme for the analysis of the time-resolved data.

decays through internal conversion to form hot spiropyran in the electronic ground state, ($\{v\}$ designates the vibrational manifold), or decays to other intermediate states which eventually may lead to merocyanine product formation. The $SP(S_1)$ decays with time t according to:

$$A \cdot \exp[-t(1/\tau_0 + 1/\tau_1] \tag{6.1}$$

where A is the amplitude at delay time $t = 0$. The time constant τ_1 does not represent the true internal conversion time constant in this analysis. A complete characterization of the cooling process (from the initial hot vibrational distribution to the thermally equilibrated vibrational distribution in the electronic ground state) requires knowledge about many more parameters than the data give access to. Therefore the data related to vibrational cooling were fitted using an effective description involving only two time constants: τ_1, which characterizes the average arrival time at the vibrational levels within the frequency interval covered by the relevant detection diode, and the time constant τ_2, which characterizes the effective average departure time from this frequency interval. Note that the signals are the net difference between (increased) absorption from $v \rightarrow v+1$ and stimulated emission from $v+1 \rightarrow v$. The signals related to transient passage of vibrational levels other than $v = 0$, are now described by

$$B \cdot \frac{\tau_2}{\tau_2 - \tau_1} \cdot [\exp(-t/\tau_2) - \exp(-t/\tau_1)] \tag{6.2}$$

The recovery of the thermally equilibrated electronic ground state, using the effective parameters τ_1 and τ_1, as evidenced by the refilling of the bleached IR absorptions, is described by:

$$C \cdot \left[\frac{\tau_1}{\tau_2 - \tau_1}\exp(-t/\tau_1) - \frac{\tau_1}{\tau_2 - \tau_1}\exp(-t/\tau_2)\right] \tag{6.3}$$

Amplitude C divided by the amplitude of the bleach at $t = 0$, in principle equals the internal conversion quantum yield (disregarding solvent and multi-photon

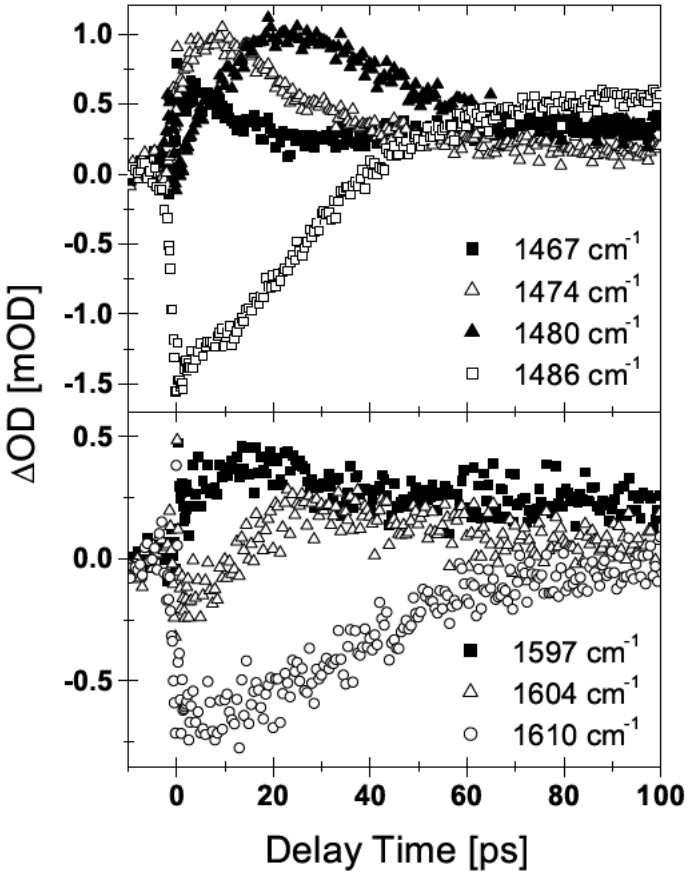

Figure 6.6: Kinetics at and below the 1486 cm^{-1} (upper panel) and 1610 cm^{-1} (lower panel) IR absorption fundamental frequencies of the closed form of BIPS.

contributions). The rise of the main product absorption bands can be described by:

$$D \cdot (1 - \exp(-t/\tau_3)) \tag{6.4}$$

This equation is valid if formation of intermediates from the $SP(S_1)$ state, governed by $(1/\tau_0 + 1/\tau_1)^{-1}$, is very fast compared to the time constant τ_3 that governs formation of merocyanine product from these intermediates. The amplitude D gives the final signal strength of the product band.

(ii) Kinetic behavior at vibrational frequencies of the (closed) spiropyran form of BIPS. First, the recovery of the bleaches is addressed in more detail. Fig. 6.6 shows kinetic traces measured at the IR absorption maxima at 1486 and 1610 cm^{-1}, and, in both cases, at slightly lower frequencies. The observed kinetics is consistent with rapid internal conversion followed by vibrational cooling.

ν	constant	B	τ_1	τ_2	-C	D	τ_3
cm^{-1}	mOD	mOD	ps	ps	mOD	mOD	ps
1461	0.41					0.26	85
1467	0.18	0.62	1	8		0.38	150
1474	0.15	1.16	3	21			
1480	- 0.09	2.41	19	19		0.31	28
1486			17	17	-1.51	0.64	28
1492	0.02					0.56	28
1498	0.13					0.46	28
1591	0.47					0.13	13
1597	0.22	0.40	14	14			
1604		1.01	24	24	- 0.29		
1610	0.05		25	25	- 0.71		
1461	0.41					0.26	85

Table 6.1: Fit results for the data displayed in Figures 6.6 and 6.7

Note that during the first 20 ps the recovery of the bleaches occurs clearly at a slower rate than in the following 80 ps. This can easily be understood since the relaxation from the excited state created by the UV pulse passes through other intermediate vibronic states with $v > 0$ before returning to the vibrational and electronic ground state ($v = 0$). Stimulated emission from $v = 1 \rightarrow v = 0$ presents an additional reason for an initially slower recovery of the bleaches at the fundamental frequencies. Due to anharmonicity, lower frequencies correspond to IR transitions between increasingly higher consecutive levels v of the vibrational ladder. Signals at frequencies below the fundamental frequencies are the difference between (increased) absorption from $v \rightarrow v + 1$ and stimulated emission from $v + 1 \rightarrow v$. Net increased absorption can be taken as an indication that the wavefunction amplitude for the level v is larger than for the level with $v + 1$. After internal conversion from the S_1 electronic state to the S_0 electronic state, the initial distribution is expected to be dominated by states with relatively high vibrational quantum numbers v. Note that the 316 nm light contains sufficient energy for about 20 quanta of the 1486 or the 1610 cm^{-1} mode (disregarding anharmonicity). The rapid rise of the signal at 1467 cm^{-1} immediately after the spike (see Fig. 6.6 and Table 6.1) therefore indicates that the internal conversion probably occurs on a subpicosecond time-scale. In accordance with a stepwise downward relaxation on the vibrational ladder [39], the increased absorption rises slower the nearer the frequency is to that of the $v = 0 \rightarrow v = 1$ transition, as

is clearly illustrated in Fig. 6.6. Finally the red-shifted increased absorption of the higher-lying vibrational quantum levels v disappears, while simultaneously the bleach of the ground state vibration is filled up. Fit results for the displayed transients based on the equations applying to the kinetic scheme, are summarized in Table 6.1 . It appears that fits with expressions 6.3 and 6.4 have a strong tendency to make τ_1 and τ_2 nearly equal if they do not differ very much (naturally the numbers cannot be exactly equal since this would make the factor $1/(\tau_2 - \tau_1)$ infinite). Only for the data at 1467 and 1474 cm^{-1} this does not occur. A single exponential fit for the 1486 cm^{-1} data resulted in a value of 37 ps for the bleach recovery, comparable to the sum of τ_1 and τ_2 (both 17 ps) obtained from fitting with Eq. 6.4. The values for τ_1 and τ_2 obtained at 1610 cm^{-1} are slightly longer than at 1486 cm^{-1}, i.e. both 25 ps instead of 17 ps. In principle, there is no reason why the recovery should not be very different for different vibrational modes. First of all, the internal conversion may favor specific vibrational modes for the conversion of electronic to vibrational energy. Second, the quantum number v of the levels populated by the internal conversion can vary considerably (differences in anharmonicity, fundamental frequency, and population of combinatorial bands). Third and last, the relaxation rates along different vibrational ladders may strongly depend on the capacity of the solvent to accept vibrational energy quanta of different frequencies, and on the efficiency of intramolecular vibrational redistribution (IVR) to other modes with lower fundamental frequencies.

While at 1610 cm^{-1} the signal is only related to the bleached spiropyran IR absorption, at 1486 cm^{-1} the bleach appears to overlap with the IR band at 1489 cm^{-1} of a merocyanine product (open form), and therefore eventually the bleach turns into an increased absorption. The kinetics at both of these bands indicate that the dominating fraction that underwent internal conversion contributes very little to the signals after 100 ps. Since, as illustrated by the data in Figs. 6.4 and 6.6, the bleach of the 1610 cm^{-1} IR absorption band has already recovered by 90% after 100 ps, the quantum yield for the internal conversion has to be $\geq$0.9. Consequently, the quantum yield for the photochemical conversion can maximally be 0.1. This value compares well to a photocoloration quantum yield of 0.055 at -120°C in a 1-propanol/2-propanol mixture reported for BIPS irradiated at 313 nm [206, 220].

(iii) Kinetics at vibrational frequencies of the merocyanine product. As mentioned before the peaks in the spectrum after 100 ps at 1461, 1489, and 1591 cm^{-1} are identified as product bands. Since the open merocyanine form rather quickly converts back to the spiropyran form (within seconds, because no coloration of the streaming solution was noticed), steady-state IR spectra of the merocyanine compound are not available. Further support for the assignment can however be derived from published time-resolved resonance Raman data [221], generated 200 ns after UV irradiation, in a variety of solvents. Unfortunately tetrachloroethene is not one of the solvents used in those studies. Probably

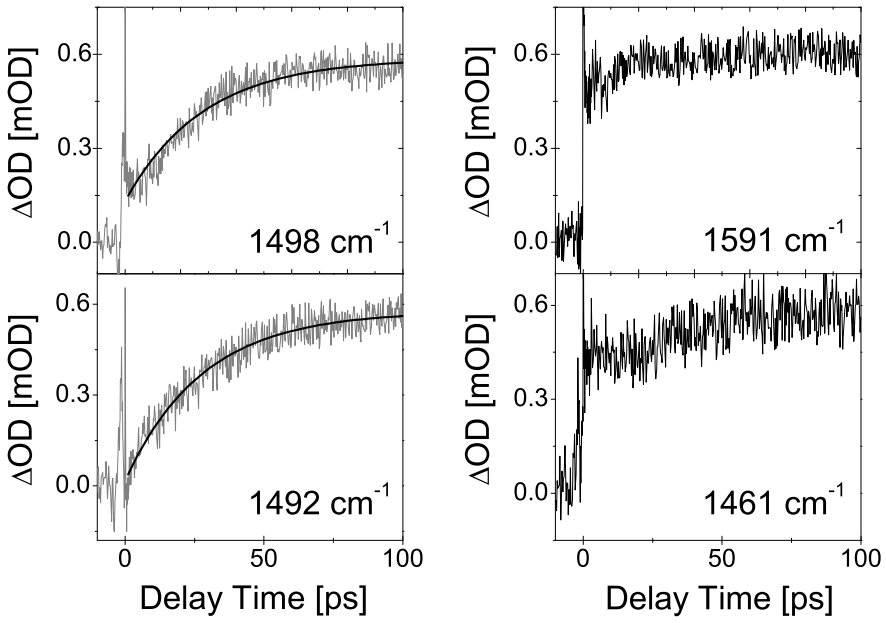

Figure 6.7: Kinetics at frequencies identified as product related. Left panel: product formation kinetics of the 1489 cm^{-1} IR absorption band, together with fits indicating a rise time of 28 ps. Rigth panel: transient signal behavior at the 1461 and 1591 cm^{-1} bands.

the data in benzene should be closest in comparison, since tetrachloroethane and benzene both do not form hydrogen bonds, are without a permanent dipole moment but slightly polarizable, and have the same dielectric constant (ε_r = 2.28). Naturally, vibrational modes that are Raman active need not to be active in IR absorption, and vice versa. Many modes are nevertheless active in both and should then appear at the same frequencies, albeit with probably very different intensity patterns peaks. The 1461, 1493 and 1591 cm^{-1} bands obtained from the IR data correspond reasonably well with the lines at 1447, 1489 and 1577 cm^{-1}, observed in the resonance Raman spectrum of merocyanine species [221]. The difference in these numbers could very well be accounted for by the resolution and signal/noise in both measurements. Note in Ref. [221] that the resonance Raman signals do not drop to zero between the vibrational peaks, perhaps due to non-resonant Raman contributions.

Fig. 6.7 shows the time dependent behaviour during the first 100 ps at frequencies identified as product related. The signals at both 1461 and 1591 cm^{-1} jump within a few hundred femtoseconds to about 0.4-0.5 mOD, to be followed by a modest increase to about 0.6 mOD in the next 100 ps. Only on the high

frequency side of the fairly broad product band at 1489 cm^{-1} clear product formation transients, well exceeding the noise level (about ±0.05 mOD) are observed. Hence, the rise time extracted from the data at 1492 and 1498 cm^{-1} in Fig. 6.7 is chosen in order to characterize the formation rate of merocyanine product(s). A look at the IR absorption spectrum of the closed form in Fig. 6.4 illustrates that both at 1461 and 1591 cm^{-1} one should expect complication of the dynamical behavior due to transient signals related to vibrational cooling of the large fraction of spiropyran molecules that underwent the internal conversion $S_1 \longrightarrow S_0$. In addition, at 1461 cm^{-1} recovery of bleached spiropyran vibrational absorptions will also contribute to the signals. On the other hand the traces in Fig. 6.7 at 1492 and 1498 cm^{-1} are fairly free of such contributions, since the first vibrational mode which could noticeable contribute through hot band absorption has its fundamental frequency more than 100 cm^{-1} higher at 1610 cm^{-1}. Only a minor bleach recovery contribution from the tail of the bleached IR absorption at 1486 cm^{-1} can complicate these signals. One can therefore conclude that only at 1492 and 1498 cm^{-1} interpretation of the data results in a reliable product formation time constant.

A product formation time constant of 28 ps is extracted from these data (see Table 6.1). This is drastically slower than the 0.9 ps time constant previously concluded from UV-pump/white-light probe measurements on BIPS in n-pentane [211]. These vastly different numbers can be reconciled with each other assuming that the 0.9 ps rise time of the broad absorption band peaking at 540 nm after UV irradiation of BIPS does not characterize the merocyanine product formation rate, but instead is an indication of how fast the $S_1 \longrightarrow S_0$ internal conversion rate is for the spiropyran form. The additional absorption, which makes the spectrum after 1 ps nearly featureless between 380 and 680 nm, was assigned by Ernsting and Arthen-Engeland [211] to absorption from the S_1 excited state of the spiropyran form to higher electronic states of the closed form and absorption from vibrationally hot merocyanine products. In view of the rapid and efficient internal conversion indicated by the data in Fig. 6.6, this featureless spectrum is assigned here to absorption from a mixture of vibrationally hot levels of the spiropyran S_0 state to vibrational levels of the spiropyran S_1 state. The sharpening of the 540 nm band between 1.1 and 7.5 ps, accompanied by about 50% increase in increased absorption, as reported by Ernsting and Arthen-Engeland, would then be the result of a gradual replacement of absorption from vibrationally hot spiropyran, which disappears due to vibrational cooling, by merocyanine absorption which is formed with a 28 ps time constant according to the data. Unfortunately the published UV pump/white-light probe transients for BIPS do not extend beyond 8 ps, and as mentioned previously, no single colour UV pump-probe measurements have been reported yet that could confirm the nearly complete ground state recovery of the closed spiropyran form.

Further support for this interpretation can be derived from combining quantum yield information for photocoloration of BIPS and 6-nitro-BIPS, with the

UV pump/white-light probe data for these two compounds. At -120°C in a 1−propanol /2−propanol mixture a photo-coloration quantum yield of 0.055 has been reported for BIPS, while for 6-nitro-BIPS this yield is 0.3, both with irradiation at 313 nm [206, 220]. The generally much higher photocoloration quantum yield for 6-nitro-BIPS compared to BIPS is well established and has been brought in connection with involvement of triplet states [218,219] in the photochemical reaction route for 6-nitro-BIPS. In addition, results of measurements performed on 6-nitro-BIPS (see Section 6.4) in tetrachloroethene indicate a much higher quantum yield for photochemistry and a lower yield for internal conversion. Although based on the above numbers the photocoloration quantum yield for 6-nitro-BIPS is expected to be about 5 times higher than for BIPS, the UV-white light pump-probe data show spectra with comparable peak intensities during the first 7.5 ps, and even after 70 ps the 6-nitro-BIPS signal is only about twice that of BIPS after 7.5 ps. Notice that, for 6-nitro-BIPS, a 20 ps merocyanine formation time constant has been reported. Clearly the difference in visible absorption at the product wavelength is less than the quantum yield data suggest, but this could be accounted for by additional absorption for BIPS from vibrationally hot molecules formed by internal conversion. As mentioned above, the energy of the 316 nm radiation is equivalent to about 20 quanta of the fundamental frequency of the 1486 or 1610 cm^{-1} modes. Absorption at 680 nm could, for instance, correspond to transitions for these from $v \geq 10 \rightarrow v' = 0$, and at 380 nm to transitions $v \cong 3 \rightarrow v' = 0$ (the accent indicates vibrational levels of the electronic excited state).

6.4 Ring opening reaction of 6-nitro-BIPS

The spiropyran-merocyanine photochemical ring opening-closure (Fig. 6.2) 6-nitro-BIPS was investigated in two solvents: tetrachloroethene (C_2Cl_4) and per-deuterated acetonitrile (ACN-d_3). As in the case of BIPS, this simple reaction presents a rather complex puzzle. It is not clear whether singlet and triplet states both are involved [218,223,227,228], and, again, to what extent the eight different cis-trans isomers [211, 220, 221, 226, 229, 230] appear in the merocyanine product. On top of that the merocyanine product can aggregate [231]. A wide range of experiments has been performed on 6-nitro-BIPS, including low temperature absorption [220], triplet sensitization [223], femto- [211, 232] and nanosecond [218] time-resolved UV-vis pump-probe spectroscopy, and time-resolved resonance Raman spectroscopy [226, 229]. Data acquired over a wider frequency range are presented and comparisons are made to results from investigations on 6-nitro-BIPS with other techniques [211, 218, 220, 221, 226, 229, 230].

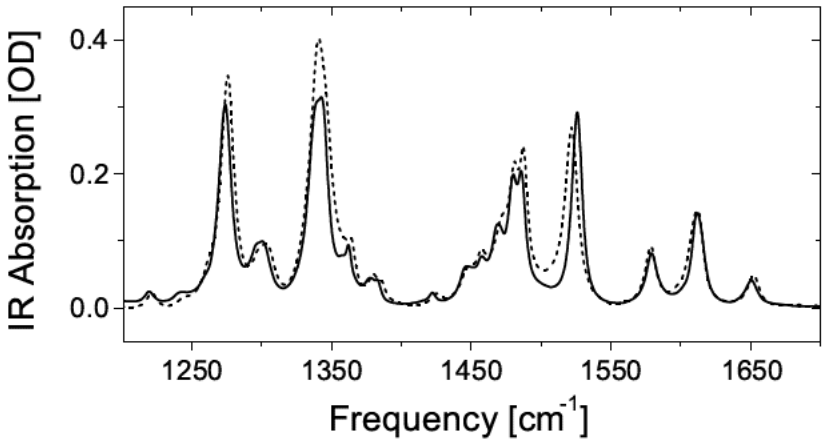

Figure 6.8: Steady state IR absorption spectra for 6-nitro-BIPS in ACN-d_3 (dashed line, 51 mM) and in C_2Cl_4 (solid line, 42 mM).

6.4.1 Experimental results

Tetrachloroethene (C_2Cl_4) and 6-nitro-BIPS were purchased from Sigma-Aldrich. Perdeuterated acetonitrile (ACN-d_3; deuteration grade 99.8%) was purchased from Deutero GmbH. The compounds were used without further purification. These solvents have limited IR absorption in the investigated frequency range. Steady-state FT-IR spectra of 6-nitro-BIPS in C_2Cl_4 and ACN-d_3 were recorded with 1 cm^{-1} resolution, using a Biorad FT-IR spectrometer. Time-resolved measurements were performed on 20 mM solutions of 6-nitro-BIPS in C_2Cl_4 and ACN-d_3. The photochromic reaction was initiated by 70 fs pulses at 330 nm (2 mJ/pulse), and the evolution of the vibrational absorption spectrum was probed with 100 fs IR pulses (20 nJ/pulse), with the center frequency varying from 1260 to 1600 cm^{-1}. In each measurement the detector covers 100 to 200 cm^{-1}, with a spectral resolution of 4 to 7 cm^{-1}.

Fig. 6.8 shows the steady-state IR absorption spectra of 6-nitro-BIPS in ACN-d_3 and C_2Cl_4 at room temperature, corrected for solvent contributions, in the range probed in the time-resolved measurements. Electronic absorption spectra (not shown) indicate that the compound is almost exclusively in the closed spiropyran form in both solutions. One can estimate that at most 1% is in a merocyanine form in ACN-d_3, and 0.01% in C_2Cl_4. The IR spectra in Fig. 6.8 clearly illustrate that the peak intensities of IR absorption bands can vary quite considerably in different solvents. For instance, the ratio of the peak intensities at 1342 cm^{-1} divided by that at 1524 cm^{-1} differs by 40% for these two solvents. Solvent dependence of IR absorption intensities and frequencies is a known effect

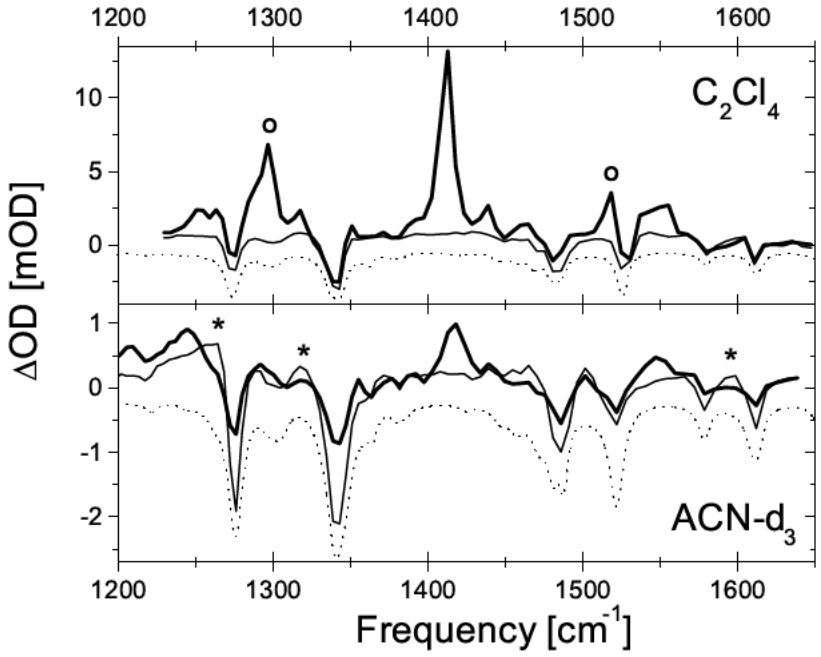

Figure 6.9: Transient IR-spectra between 1200 and 1650 cm^{-1}, for 6-nitro-BIPS in C_2Cl_4 (upper panel) and in ACN-$_3$ (lower panel), 2 ps after UV-excitation (thin solid lines), and at 150 ps and 60 ps, for C_2Cl_4 and ACN-d_3, respectively (thick solid lines). For comparison, the inverted steady-state IR spectra of 6-nitro-BIPS in the respective solvents are also depicted (dotted lines), roughly scaled to the bleaches at early times, with an offset of -0.25 mOD for ACN-d_3, and -0.5 mOD for C_2Cl_4.

[18]. Fig. 6.9 shows overall transient differential spectra created from the data for 6-nitro-BIPS in C_2Cl_4 (upper panel) and ACN-d_3 (lower panel), 2 ps after UV excitation, and at long delay. For comparison with the bleaches at early delays the steady-state IR absorption spectrum is also plotted. The initial spectra resemble the steady-state IR spectra well, indicating removal of ground state (closed) spiropyran species by the femtosecond UV excitation pulse. Note further that in C_2Cl_4 not a single sharp increased absorption feature is found at early times. In ACN-d_3 the initial spectrum shows a few positive features (marked *), that are assigned to vibrational hot bands of the spiropyran species in the electronic ground state formed after internal conversion. The kinetics in ACN-d_3 at 1264 cm^{-1} depicted in Fig. 4C, illustrate the vibrational cooling dynamics for hot spiropyran (see Section 6.3).

Spectra at long delay times show for both solvents (residual) bleaches as well as a number of peaks related to photoproducts. It must be pointed out that in

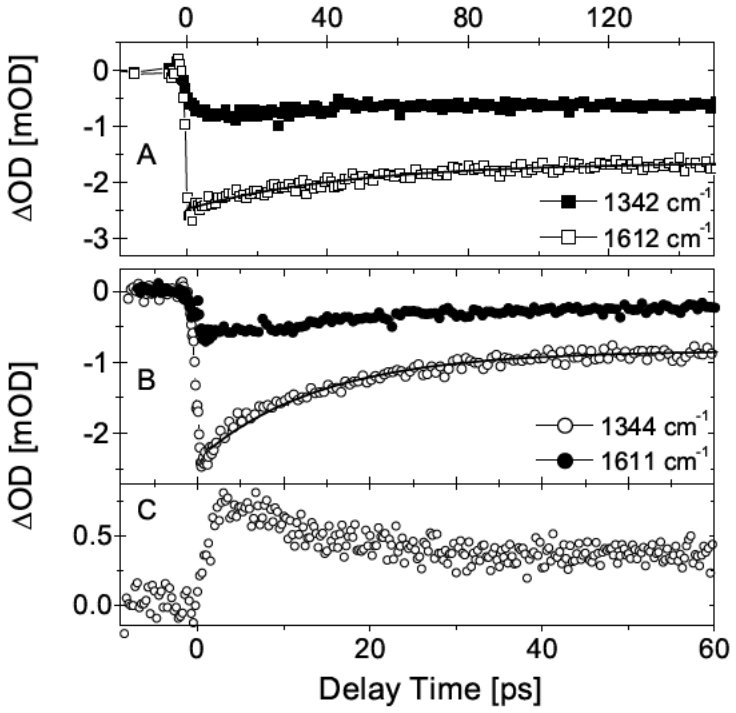

Figure 6.10: A-B) Bleach recovery at two vibrational frequencies of 6-nitro-BIPS (in the spiropyran form) in C_2Cl_4 (A) and in ACN-d_3 (B). The numbers correspond to the central frequency associated with the diode pixels. The solid lines are fits corresponding to decay times of 47 ps in C_2Cl_4, and 14 ps in in ACN-d_3. C) Kinetics related to the spiropyran vibrational hot band at 1264 cm^{-1} in ACN-d_3. The time scale at the bottom applies to both panel B) and C).

C_2Cl_4 the bleaches have recovered by ~34% in C_2Cl_4 after 150 ps, and ~63% in ACN-d_3 after 60 ps. Note also the strong lines at 1297 and 1519 cm^{-1} (marked o) in C_2Cl_4 , which appear nearly absent in ACN-d_3, and have to be associated with the formation of an additional merocyanine isomer in C_2Cl_4.

6.4.2 Discussion

(i) Bleach recovery and internal conversion. The kinetic behaviour related to the spiropyran form of 6-nitroBIPS is illustrated in Fig. 6.10 at two bleached vibrational absorption bands: 1342 and 1612 cm^{-1}. These data show that both in C_2Cl_4 (Fig. 6.10A) and in ACN-d_3 (Fig. 6.10B) the bleaches partially recover. This recovery has to be due to regeneration of the spiropyran ground state, and

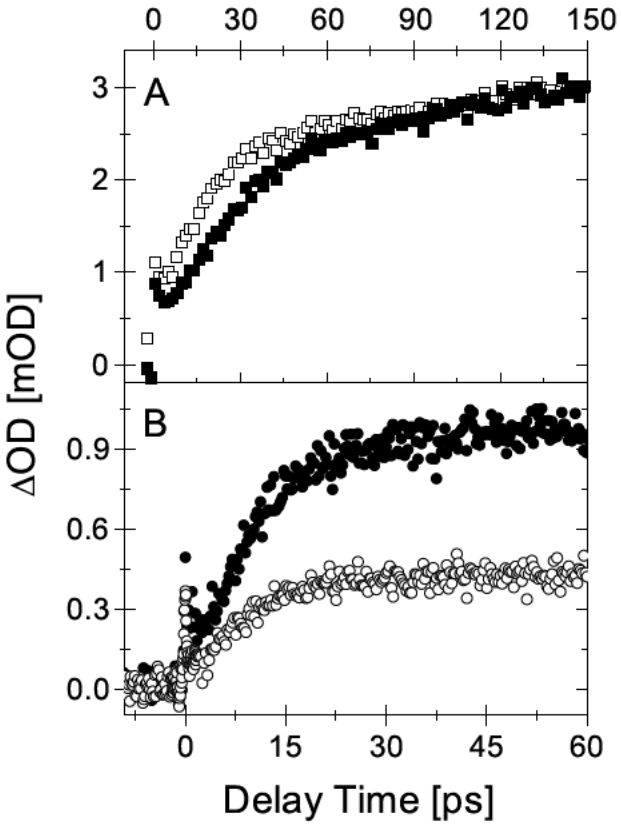

Figure 6.11: (A) Merocyanine product formation kinetics for 6-nitroBIPS in C_2Cl_4 at 1551 (open squares) and 1556 cm^{-1} (solid squares). (B) Product formation kinetics for 6-nitroBIPS in ACN-d_3 at 1418 (solid circles) and 1551 cm-1 (open circles).

therefore indicates the occurrence of internal conversion. The data demonstrate that the quantum yield for internal conversion is solvent dependent: about 34% in C_2Cl_4, and 63% in ACN-d_3 (error margin: $\pm 5\%$). Previous investigations had not identified this apparently rather influential decay channel. It may well be that the efficiency of internal conversion is a key factor in determining the overall photochemistry quantum yield. Given the observed bleach recovery the maximum quantum yield for photochemistry of 6-nitroBIPS is 0.66 in C_2Cl_4, and 0.37 in ACN-d_3. (Absolute [206, 233] and relative [227, 228] photochemistry quantum yields have been reported for 6-nitroBIPS in various solvents.) The refill rate of the bleach, after internal conversion and subsequent vibrational cooling, is also different for these two solvents: 47 (± 10) ps in C_2Cl_4, and 14 (± 2) ps in ACN-d_3.

(ii) Existence of different merocyanine isomers. Based on the spectra at

long delays shown in Fig. 6.9, combined with observed kinetics at different frequencies, one can identify with certainty product bands in ACN-d_3 around 1245, 1299, 1355, 1417 and 1551 cm^{-1}. In C_2Cl_4 bands are identified at the similar frequencies 1251, 1297, 1351, 1413 cm^{-1} and in the range 1537-1556 cm^{-1}. In addition, in C_2Cl_4 IR bands are observed at 1263, 1318, 1439, 1463, and 1519 cm^{-1}. Note that, in general, the signals in C_2Cl_4 are much stronger than in ACN-d_3. Therefore some of the weaker bands in C_2Cl_4 could be below the detection threshold in ACN-d_3. The bands at 1297, 1413, and 1519 cm^{-1} are much more intense in C_2Cl_4 than in ACN-d_3 (about an order of magnitude or more). As the difference in internal conversion efficiency can only justify a factor two in photochemistry quantum yield, one can conclude that these three peaks constitute reliable evidence for the existence of an additional different merocyanine isomer in C_2Cl_4, that is not present in ACN-d_3. Because all product bands in ACN-d_3 are also observed in C_2Cl_4, the isomer that is formed in ACN-d_3 is likely to be present in C_2Cl_4 as well. These conclusions are further supported by the product formation kinetics discussed below. Takahashi and co-workers have concluded the existence of five isomeric species [226] from time-resolved Raman spectra of 6-nitroBIPS, taken from 200 ns to 2 ms after UV excitation in three different solvents. These assignments were mainly based on intensity variations of different Raman lines, and analogy to a similar study on the parent compound BIPS [221]. Two species were brought in connection with only a single Raman line. As demonstrated for spiropyran in Fig. 6.8, IR absorption intensities of the same species can already vary considerably from solvent to solvent. Clearly, moderate intensity variations alone are a poor basis for the identification of different isomeric species. In a later investigation on 6-nitroBIPS in cyclohexane, they followed the time evolution of the Raman spectrum between 20 ns and 100 ms after UV excitation [229]. This time only three transient species were invoked in the interpretation. The species identified at earliest times was ascribed to a merocyanine triplet state. A convincing correlation between the decay of the 1409 cm^{-1} Raman intensity (0.33 ms time constant), and the increase of the 1525 cm^{-1} Raman intensity, led to assignment of the second species as ground state merocyanine. On the ms timescale a third species is identified as a dimeric species. As none of these re-assignments require the existence of different isomers, the previous claim of five existing isomers should at least be reduced to maximally three. Several other inconsistencies can be noted in those Raman assignments. For example, the 20 ns data in Ref. [229] clearly illustrate that assigning both the 1550 and 1523 cm^{-1} lines to the same “initial cisoid 1523 cm^{-1} species" in Ref. [226] was incorrect. About half of the observed resonance Raman peaks correspond to lines observed in IR absorption: for 6-nitroBIPS in ACN (after 2 ms, [226]) these are at 1358 and 1411 cm^{-1}. Data in C_2Cl_4 are probably best compared to the 20 ns Raman data in cyclohexane [229], that show related peaks at 1297, 1350, 1409, and 1552 cm^{-1}. Recall that Raman and IR absorption yield complementary information. Recently, density-functional-theory calculations on the spiropyran form

of 6-nitroBIPS and the four most stable merocyanine isomers were presented, and compared to IR absorption spectra in an argon matrix at 8 K [230]. Reasonable agreement was obtained between experiment and calculations, although insufficient to unequivocally identify the isomers. More specifically, the intense experimental line at 1529 cm^{-1} corresponds to a calculated line at 1551 cm^{-1}. This experimental 1529 cm^{-1} line could be associated with the extra isomer in the C_2Cl_4 data, whereas the calculated 1551 cm^{-1} line agrees with the observation of both isomers. Altogether the existing experimental results provide insufficient evidence for claiming formation of five isomers. It seems therefore prudent to conclude that there are strong indications for existence of at least a second isomeric species in C_2Cl_4, not formed in ACN-d_3.

(iii) Product formation kinetics. Kinetics at selected wavelengths is depicted in Fig. 6.11. The lower panel shows the product formation kinetics in ACN-d_3 at 1418 and 1551 cm^{-1}. Single exponential fits of these two traces indicate a single exponential formation time of 9.5 ± 1.5 ps. No further change in product absorption was observed between 30 and 100 ps. However, there seems to be some variation in rise time over the bands; e.g., at 1413 cm^{-1} we obtain 7.1 ps. This behavior is observed even more clearly in C_2Cl_4, where the overall product formation in C_2Cl_4 is considerably slower. The upper panel shows the product related signals at 1551 and 1556 cm^{-1}. Clearly the signal rises much faster at 1551 cm^{-1} during the first 50 ps. Single exponential fits at different product bands produce rise times in the range of 35 to 60 ps for 6-nitroBIPS in C_2Cl_4. As indicated by the data in Fig. 6.11 (B) the kinetics require at least a biexponential fitting approach. For the strongest band (around 1413 cm^{-1}) this procedure resulted in a faster component increasing from about 5 ps at 1397 cm^{-1} to 28 ps at 1413 and 1418 cm^{-1}, and a second component typically >100 ps. Because the data are only up to 150 ps, the time constant of the slow component cannot be extracted reliably. The most likely source for the observed frequency dependence of the faster component is vibrational cooling dynamics of the merocyanine products.

Absorption change studies on 6-nitroBIPS in hexane and acetonitrile by Lenoble and Becker [218], with 1 ns time resolution, indicated that in acetronitrile the rise of the 570 nm product related band was complete within 1 ns. The infrared measurements lower the upper limit for the product formation time in (perdeuterated) acetonitrile to about 9.5 ps. The fast component in C_2Cl_4 (∼5-28 ps), and the time constant in ACN-d_3 (∼7-10 ps), are in line with a 20 ps time constant found by Ernsting and Arthen-Engeland [211] in a femtosecond UV/white-light investigation of 6-nitroBIPS in n-pentane. Based on solvent polarity one may suspect that the kinetic behaviour in hexane, n-pentane, and tetrachloroethene should be rather similar. This seems true for these measurements compared to those of Ernsting and Arthen-Engeland [211]. However, in hexane the fastest rise time identified by Lenoble and Becker was 4 ns at 430

nm [218]. Whether the slow >100 ps component in C_2Cl_4 can be reconciled with their nanosecond result in hexane remains an open question. The biexponentiality of the product formation in C_2Cl_4, versus single exponential kinetics in ACN-d_3, clearly corroborates the conclusion drawn above on formation of a second isomeric species in C_2Cl_4. This biexponentiality also implies that these species cannot be formed in direct competition from a mutual precursor state, since this would lead to the same formation constant for both. Note that published conclusions on different isomers was based on data obtained 20 ns or more after UV irradiation of a sample. These data therefore constitute the first time-resolved evidence that a second isomer already appears within hundred picoseconds.

6.5 Summary and Conclusions

In conclusion, the investigation of photochromic compounds with ultraviolet pump/mid-infrared probe spectroscopy has given new insights into one of the most studied photochromic reactions: the spiropyran-merocyanine chemical ring opening/closure isomerization. The ring opening reaction of spiropyran compounds is initiated by femtosecond UV pump pulses, and the dynamics of the formation of merocyanine product species are followed by probing with femtosecond mid-IR pulses the time-evolution of the vibrational absorption spectrum. Two systems have been addressed: the spiropyran BIPS and a spiropyran derivative with a NO_2 substituent on the benzopyran ring, 6-nitro-BIPS.

In the case of BIPS, the experimental data suggest that the merocyanine product is probably formed from intermediates other than the initially created excited state of the spiropyran, which are populated on a subpicosecond timescale in competition with a very efficient and rapid internal conversion process. From these intermediates a single exponential formation of a merocyanine form with a 28 ps time constant is concluded, which is in sharp contrast to previous conclusions of a 0.9 ps formation time constant, derived from femtosecond UV pump/ white-light probe measurements. This illustrates that care has to be taken with conclusions based on optical pump/probe spectroscopy only. IR probing has been a useful alternative means of obtaining information on the photoinduced reaction. The recovery of the spiropyran IR absorption bleaches shows clearly that the main decay channel for the spiropyran S_1 excited state is internal conversion to the spiropyran S_0 state with a yield of 90% or more. The quantum yield for the photochemical reaction is therefore ≤ 0.1. Previous investigations never mentioned this a rather influential decay channel, which may well be the key factor in determining the overall photochemistry quantum yield for this class of molecules.

In 6-nitro-BIPS, competition between internal conversion and photochemistry is also found to depend on the solvent. The IC quantum yield is determined to be 0.63 in perdeuterated acetonitrile, and 0.34 in tetrachloroethene. Based

on spectral features and biexponential kinetics, the formation of an additional merocyanine isomer in tetrachloroethene is concluded, suggesting that interactions between excited-state species and the solvent are factors determining the route of the photoreaction. The kinetics of product formation, as determined in the ultraviolet pump/mid-infrared probe experiments show as well an interesting solvent dependence.

Chapter 7

Summary and Conclusions

In this thesis femtosecond mid-infrared spectroscopy has been applied to the investigation of some of the most thoroughly studied photoinduced reactions: the excited state hydrogen/proton transfer, both in an *intramolecular* and in an *intermolecular* case, and the isomerization of photochromic compounds.

Electronic spectroscopy is the most commonly used method for ultrafast studies of molecular reaction dynamics in the condensed phase, whereby the electronic states of the reacting molecular systems are monitored. These techniques typically probe electronic transitions occurring between delocalized orbitals and - thus - do not provide site-specific information. Besides, the broad absorption lines resulting from the fast dephasing times of electronic transitions in solutions may hinder a reliable interpretation of the experimental results, especially when the complexity of the reaction increases, due e.g. to the presence of different isomers or to the involvement of numerous electronic states. Femtosecond infrared spectroscopy has been used in this work as a powerful and complementary alternative to probe ultrafast reaction dynamics, exploiting the high degree of correlation between the infrared spectra and the molecular structure and the advantages stemming from the narrow bandwidths of IR-active vibrational modes.

The major part of the work described in this thesis has been devoted to one of the main issues of the ultrafast spectroscopy on hydrogen-bonded systems: the study of photoinduced hydrogen/proton transfer processes in electronically excited states. This elementary reaction is an interesting model case for studying basic microscopic reaction mechanism and plays as well an important role in the molecular function of a variety of systems.

The excited-state *intramolecular* hydrogen transfer (ESIHT) has been studied in the HBT molecule, where the ESIHT reaction takes the typical form of a enol-keto tautomerization reaction. After UV excitation, the formation of the keto species of HBT was temporally resolved by probing the build-up on a 30-50 fs time scale of the C=O carbonyl stretching mode marking the keto state, which is formed by hydrogen transfer. Together with the formation of the C=O stretching band, the bleaching of several bands possessing C-O character gives the direct evidence of the photoinduced formation of the keto geometry of HBT. A detailed study of the transient vibrational spectrum of the keto* species in the entire fingerprint region was carried out. The analysis of the shapes of the observed bands, including the C=O mode, reveals that such modes are formed in their $v = 0$ ground state, thus showing that these vibrations do not serve as channels accepting the excess energy released in the ESIHT reaction. This implies that the elongation of the C=O stretching mode is not involved in the hydrogen transfer reaction. The excess energy is initially contained mainly in a set of low-frequency, Raman active modes that are elongated upon electronic excitation. The excitation of these low-frequency Raman active vibrations induces through anharmonic couplings an initial red-shift of the IR active bands in the fingerprint region. Subsequent redistribution of the vibrational energy gives rise, on a picosecond time scale, to a characteristic blue-shift of the measured bands. Oscillatory features in the dynamics of the C=O band have been interpreted as a consequence of coherent wavepacket motions along two anharmonically coupled low frequency modes.
A study of the (bimolecular) acid-base neutralization reaction in liquid water, involving an *intermolecular* proton transfer, is the second model case studied. The reaction is initiated by by electronic excitation of a photoacid, resulting in an increase of its acidity constant by seven orders of magnitude. The reaction dynamics can be followed through inspection of specific IR-active vibrational marker modes of the photoacid and of its conjugate anion, and of the protonated base that is generated in the reaction. The data reveal clearly two aspects. Under conditions of high base concentrations one can monitor the proton transfer along a pre-existing hydrogen bond in “tightly" bound acid-base complexes, where an extremely rapid, non diffusion-limited proton transfer occurs, on a time scale which cannot be resolved with an experimental time-resolution of 150 fs. In contrast, at low base concentrations the initially uncomplexed acid forms, after

diffusive motion, “loosely" bound complexes and the reaction occurs on a much slower time scale. In order to reconcile these results, a refinement of the classical Eigen-Weller picture of acid-base reactions is needed. This has been traditionally understood to comprise (i) diffusive motion of acid and base, (ii) “on-contact" reaction dynamics where a proton is transferred from the acid to the base, and (iii) diffusive separation of proton transferred ion pairs. The refined reaction scheme gives a more detailed description of the “on-contact" reaction step in terms of a three stage model, whereby the formation by diffusion of a “loosely" bound acid base encounter pair is followed by rearrangement to a “tightly" bound reaction pair, before the final prompt proton transfer reaction can occur. The observation of the ultrafast bimolecular proton transfer (more than one order of magnitude faster than previously believed) in a system where under ambient conditions the reactants (or a significant fraction of them) do not have to diffusively encounter each other is in itself fundamentally important.
The study of a different class of photoinduced reactions constitutes the last part of this work: the ring opening reaction of photochromic spiropyrans. Photochromic compounds change color after the absorption of light of specific wavelengths, as a consequence of the photoinduced reversible transformation between two isomeric forms, which differ from one another in various properties, including the absorption spectra. Such a property is of potential interest for a broad range of applications, from optical data storage and displays to optically controlled molecular switching. The spiropyran-merocyanine chemical ring opening/closure reaction, one of the most studied photochromic reactions, was studied in two molecular systems, BIPS and 6n-BIPS. By monitoring the mid-IR spectra of the reacting species, the relevant time scales for the formation of the reaction products have been determined and the role of different merocyanine isomers in the reaction has been discussed. In particular, these investigations have provided valuable insight into the reaction pathways and efficiencies, showing that an important decay channel for the spiropyran excited state is the internal conversion to the spiropyran ground state, with a quantum yield of 90% or more in the case of BIPS, of 63% and 34% (depending on the solvent) for 6n-BIPS. Internal conversion is thus a rather influential decay channel, which may well be the key factor in determining the overall photochemistry quantum yield for this class of molecules. This aspect must be better understood if one thinks in terms of

potential applications to actual devices, where, of course, usable photochromic systems should be characterized in the first instance by a high reaction yield.

Altogether, these experimental studies show the potential of ultrafast infrared spectroscopy as a tool for investigating molecular vibrational and reaction dynamics. The results on the bimolecular acid-base neutralization reaction suggest a general use of this method in studies of reaction dynamics governed by diffusion or transport phenomena, as well as in studies where the reactants are already at contact. As natural follow-up of the work on the intra- and intermolecular hydrogen/proton transfer in HBT and HPTS, one can foresee the investigation by means of ultraviolet pump/mid-infrared probe spectroscopy of more complicated molecular systems such as green fluorescent proteins (GFP), important biological markers where a proton transfer process is supposed to be the first step of the photoinduced isomerization [234]. Finally, the studies of the ring-opening reaction of spiropyrans motivate future experimental and theoretical efforts to elucidate the role of internal conversion in the photochemistry of photochromic compounds.

References

[1] *Femtochemistry*, F. C. de Schryver, S. de Feyter, and G. Schweitzer, eds., (Wiley-VCH, Weinheim, 2001).

[2] G. R. Fleming, *Chemical applications of ultrafast spectroscopy* (Oxford University Press, New York, 1986).

[3] A. H. Zewail, Science **242,** 1645 (1988).

[4] A. H. Zewail, J. Phys. Chem. A **104,** 5660 (2000).

[5] C. Rischel, A. Rousse, I. Uschmann, P. A. Albouy, J. P. Geindre, P. Audebert, J. C. Gauthier, E. Fröster, J. L. Martin, and A. Antonetti, Nature **390,** 490 (1997).

[6] C. Rose-Petruck, R. Jimenez, T. Guo, A. Cavalleri, C. W. Siders, F. Raksi, J. A. Squier, B. C. Walker, K. R. Wilson, and C. P. J. Barty, Nature **398,** 310 (1999).

[7] C. W. Siders, A. Cavalleri, K. Sokolowski-Tinten, C. Tóth, T. Guo, M. Kammler, M. H. von Hoegen, K. R. Wilson, D. von der Linde, and C. P. J. Barty, Science **286,** 1340 (1999).

[8] A. Rousse *et al.*, Nature **410,** 65 (2001).

[9] F. Raksi, K. R. Wilson, J. Zhimig, A. Ikhlef, C. Y. Cote, and J. C. Kieffer, J. Chem. Phys. **104,** 6066 (1996).

[10] M. Bauer, C. Lei, K. Read, T. R. Tobey, J. Gland, M. M. Murnane, and H. C. Kapteyn, Phys. Rev. Lett. **87,** 25501 (2001).

[11] J. C. Williamson, C. Jianming, I. Hyotcherl, H. Frey, and A. H. Zewail, Nature **386,** 159 (1997).

[12] H. Ihee, V. A. Lobastov, U. M. Gomez, B. M. Goodson, R. Srinivasan, C.-Y. Ruan, and A. H. Zewail, Science **291,** 458 (2001).

[13] D. Hadži and S. Bratos, in *The Hydrogen Bond: Recent Developments in Theory and Experiments*, P. Schuster, G. Zundel, and C. Sandorfy, eds., (North-Holland, Amsterdam, 1976), Vol. II, p. 565, chapter 12.

[14] C. Chudoba, E. T. J. Nibbering, and T. Elsaesser, Phys. Rev. Lett. **81,** 3010 (1998).

[15] E. T. J. Nibbering, C. Chudoba, and T. Elsaesser, Isr. J. Chem. **39,** 333 (1999).

[16] C. Chudoba, E. T. J. Nibbering, , and T. Elsaesser, J. Phys. Chem. A **103,** 5625 (1999).

[17] E. T. J. Nibbering and T. Elsaesser, Appl. Phys. B **B71,** 439 (2000).

[18] E. T. J. Nibbering, F. Tschirschwitz, C. Chudoba, and T. Elsaesser, J. Phys. Chem. A **104,** 4236 (2000).

[19] E. T. J. Nibbering and J. Dreyer, in *Femtochemistry*, F. C. de Schryver, S. de Feyter, and G. Schweitzer, eds., (Wiley-VCH, Weinheim, Germany, 2001), p. 345.

[20] C. Chudoba, A. Kummrow, J. Dreyer, J. Stenger, E. T. J. Nibbering, T. Elsaesser, and K. A. Zachariasse, Chem. Phys. Lett. **309,** 357 (1999).

[21] J. Dreyer and A. Kummrow, J. Am. Chem. Soc. **122,** 2577 (2000).

[22] A. Kummrow, J. Dreyer, C. Chudoba, J. Stenger, E. T. J. Nibbering, and T. Elsaesser, J. Chin. Chem. Soc. **47,** 721 (2000).

[23] H. Okamoto, J. Phys. Chem. A **104,** 4182 (2000).

[24] W. M. Kwok, C. Ma, P. Matousek, A. W. Parker, D. Phillips, W. T. Toner, and M. Towrie, Chem. Phys. Lett. **322,** 395 (2000).

[25] W. M. Kwok, C. Ma, D. Phillips, P. Matousek, A. W. Parker, and M. Towrie, J. Phys. Chem. A **104,** 4188 (2000).

[26] W. M. Kwok, C. Ma, P. Matousek, A. W. Parker, D. Phillips, W. T. Toner, M. Towrie, and S. Umapathy, J. Phys. Chem. A **105,** 984 (2001).

[27] J. Stenger, D. Madsen, J. Dreyer, E. T. J. Nibbering, P. Hamm, and T. Elsaesser, J. Phys. Chem. A **105,** 2929 (2001).

[28] D. Madsen, J. Stenger, J. Dreyer, E. T. J. Nibbering, P. Hamm, and T. Elsaesser, Chem. Phys. Lett. **341,** 56 (2001).

[29] K. Heyne, N. Huse, E. T. J. Nibbering, and T. Elsaesser, Chem. Phys. Lett. **369,** 591 (2003).

[30] P. Hamm and R. Hochstrasser, in *Ultrafast Infrared and Raman Spectroscopy*, M. Fayer, ed., (Marcel Dekker, New York, 2001), p. 273.

[31] P. Hamm, M. Lim, W. F. DeGrado, and R. M. Hochstrasser, J. Chem. Phys. **112,** 1907 (2000).

[32] S. Woutersen and P. Hamm, J. Chem. Phys. **114,** 2727 (2001).

[33] S. Woutersen, Y. Mu, G. Stock, and P. Hamm, Proc. Natl. Acad. Sci. USA **98,** 11254 (2001).

[34] M. T. Zanni, N.-H. Ge, Y. S. Kim, and R. M. Hochstrasser, Proc. Natl. Acad. Sci. USA **98,** 11265 (2001).

[35] S. Woutersen, Y. Mu, G. Stock, and P. Hamm, Chem. Phys. **266,** 137 (2001).

[36] N. Demirdöven, M. Khalil, O. Golonzka, and A. Tokmakoff, J. Phys. Chem. A **105,** 8025 (2001).

[37] K. Wynne and R. M. Hochstrasser, Chem. Phys. **211,** 193 (1995).

[38] P. Hamm, Chem. Phys. **200,** 415 (1995).

[39] P. Hamm, S. M. Ohline, and W. Zinth, J. Chem. Phys. **106,** 519 (1997).

[40] G. Herzberg, *Molecular Spectra and Molecular Structure. II. Infrared and Raman Spectra of Poliatomic Molecules* (Van Nostrand Reinhold, New York, 1945).

[41] H. H. Nielsen, Rev. Mod. Phys. **23,** 90 (1951).

[42] G. R. Fleming, in *Chemical applications of ultrafast spectroscopy* (Oxford University Press, New York, 1986), chapter 6.

[43] Y. R. Shen, *The principles of nonlinear optics* (Wiley, New York, 1984).

[44] S. Mukamel, *Principles of Nonlinear Optical Spectroscopy* (Oxford University Press, New York, 1995).

[45] S. Maiti, G. C. Walker, B. R. Cowen, R. Pippenger, C. C. Moser, P. L. Dutton, and R. M. Hochstrasser, Proc. Natl. Acad. Sci. USA **91,** 10360 (1994).

[46] P. C. Becker, H. L. Fragnito, J. Y. Bigot, C. H. B. Cruz, R. L. Fork, and C. V. Shank, Phys. Rev. Lett. **31,** 505 (1989).

[47] G. R. Fleming and M. Cho, Annu. Rev. Phys. Chem. **47,** 109 (1996).

[48] W. P. de Boeij, M. S. Pshenichnikov, and D. A. Wiersma, Annu. Rev. Phys. Chem. **49,** 99 (1998).

[49] G. J. Evans and M. W. Evans, Spectrochim. Acta **38 A,** 421 (1982).

[50] Y. Maréchal, in *Vibrational Spectroscopy and Structure*, J. Durig, ed., (Elsevier, Amsterdam, 1987), p. 311.

[51] N. D. Campo, M. Besnard, and J. Yarwood, Chem. Phys. **142,** 91 (1990).

[52] M. Mueller, K. Wynne, and J. D. W. V. Voors, Chem. Phys. **128,** 549 (1988).

[53] A. Laubereau and W. Kaiser, Rev. Mod. Phys. **50,** 607 (1976).

[54] D. van den Bout, L. J. Muller, and M. Berg, Phys. Rev. Lett. **67,** 3700 (1991).

[55] M. Joffre, D. Hulin, A. Migus, A. Antonetti, C. B. Guillaume, N. Peyghambarian, M. Lindberg, and S. W. Koch, Opt. Lett. **13,** 276 (1988).

[56] G. Herzberg, *Molecular vibrational-rotational spectra* (Academia, Prague, 1982).

[57] P. E. Maslen, N. C. Handy, R. D. Amos, and D. Jayatilaka, J. Chem. Phys. **97,** 4233 (1992).

[58] A. Miani, E. Canè, P. Palmieri, A. Trombetti, and N. Handy, J. Chem. Phys. **112,** 248 (2000).

[59] E. B. Wilson, J. C. Decius, and P. C. Cross, *Molecular vibrations* (Dover, New York, 1955).

[60] E. E. Nikitin, C. Noda, and R. N. Zare, J. Chem. Phys. **98,** 46 (1993).

[61] E. P. Ippen and C. V. Shank, Appl. Phys. Lett. **26,** 92 (1975).

[62] B. I. Green and R. C. Farrow, Chem. Phys. Lett. **98,** 273 (1983).

[63] M. Lim, T. A. Jackson, and P. A. Anfinrud, Science **269,** 962 (1995).

[64] P. Debye, *Polar molecules* (Dover, New York, 1929).

[65] T. Beddard, M. Ebrahimzadeh, T. D. Reid, and W. Sibbet, Opt. Lett. **25,** 1052 (2000).

[66] K. C. Burr, C. L. Tang, M. A. Arbore, and M. M. Fejer, Opt. Lett. **22,** 1458 (1997).

[67] F. Seifert, V. Petrov, and M. Woerner, Opt. Lett. **19,** 2009 (1994).

[68] R. A. Kaindl, M. Wurm, K. Reimann, P. Hamm, A. M. Weiner, and M. Woerner, J. Opt. Soc. Am. B **17,** 2086 (2000).

[69] P. Hamm, R. A. Kaindl, and J. Stenger, Opt. Lett. **25,** 1798 (2000).

[70] F. Eickemeyer, R. A. Kaindl, M. Woerner, T. Elsaesser, and A. M. Weiner, Opt. Lett. **25,** 1472 (2000).

[71] T. Witte, D. Zeidler, D. Proch, K. L. Kompa, and M. Motzkus, Opt. Lett. **27,** 131 (2002).

[72] G. M. H. Knippels, R. F. X. A. M. Mols, A. F. G. van der Meer, D. Oepts, and P. W. Amersfoort, Phys. Rev. Lett. **75,** 1775 (1995).

[73] G. M. H. Knippels, M. J. van de Pol, H. P. M. Pellemans, P. C. M. Planken, and A. F. G. van der Meer, Opt. Lett. **23,** 1754 (1998).

[74] D. Strickland and G. Mourou, Opt. Comm. **56,** 219 (1985).

[75] A. Stingl, M. Lenzner, C. Spielmann, F. Krausz, and R. Szipcs, Opt. Lett. **20,** 602 (1995).

[76] F. Krausz, M. E. Fermann, T. Brabec, P. F. Curley, M. Hofer, M. H. Ober, C. Spielmann, E. Winter, and A. J. Schmidt, IEEE J. Quantum Electron. **28,** 2097 (1992).

[77] C. Rullière, *Femtosecond Laser Pulses* (Springer, Berlin, Heidelberg, New York, 1998).

[78] D. E. Spence, P. N. Kean, , and W. Sibbet, Opt. Lett. **16,** 42 (1991).

[79] B. E. Lemoff and C. P. J. Barty, Opt. Lett. **18,** 1651 (1993).

[80] A. M. Weiner, IEEE, J. Quantum Electron. **19,** 1276 (1983).

[81] P. Hamm, M. Lim, and R. M. Hochstrasser, J. Chem. Phys. **197,** 10523 (1997).

[82] A. Kummrow, M. Wittmann, F. Tschirschwitz, G. Korn, and E. T. J. Nibbering, Appl. Phys. B **71,** 885 (2000).

[83] T. Wilhelm, J. Piel, and E. Riedle, Opt. Lett. **22,** 1494 (1997).

[84] N. Demirdöven, M. Khalil, O. Golonzka, and A. Tokmakoff, Opt. Lett. **27,** 433 (2002).

[85] A. Seilmeier, M. Woerner, H. J. Huebner, and W. J. Kaiser, Appl. Phys. Lett. **53,** 2468 (1988).

[86] R. Pomès and B. Roux, J. Phys. Chem. **100,** 2519 (1996).

[87] M. E. Tuckerman, D. Marx, M. L. Klein, and M. Parrinello, Science **275,** 179 (1997).

[88] P. L. Geissler, C. Dellago, D. Chandler, J. Hutter, and M. Parrinello, Science **291,** 2121 (2001).

[89] R. A. Mathies, S. W. Lin, J. B. Ames, and W. T. Pollard, Annu. Rev. Biophys. Biophys. Chem. **20,** 491 (1991).

[90] D. Borgis and J. T. Hynes, J. Chem. Phys. **94,** 3619 (1991).

[91] D. Borgis and J. T. Hynes, Chem. Phys. **170,** 315 (1993).

[92] T. Elsaesser, in *Ultrafast Hydrogen Bonding Dynamics and Proton Transfer Processes in the Condensed Phase*, T. Elsaesser and H. J. Bakker, eds., (Kluwer Academic Publishers, Dordrecht, Netherlands, 2002), chapter 6.

[93] A. Weller, Z. Elektrochem. **60,** 1144 (1956).

[94] A. Weller, Prog. React. Kinet. **1,** 187 (1961).

[95] D. L. Williams and A. Heller, J. Phys. Chem. **74,** 4473 (1970).

[96] J. E. A. Otterstedt, J. Chem. Phys. **58,** 5716 (1972).

[97] A. Sobolewski and W. Domcke, in *Ultrafast Hydrogen Bonding Dynamics and Proton Transfer Processes in the Condensed Phase*, T. Elsaesser and H. J. Bakker, eds., (Kluwer Academic Publishers, Dordrecht, Netherlands, 2002), chapter 5.

[98] P. Chou, D. McMorrow, T. J. Aartsma, and M. Kasha, J. Phys. Chem. **88,** 4596 (1984).

[99] A. Syntik and D. G. M. Kasha, Proc. Natl. Acad. Sci. USA **91,** 11968 (1994).

[100] H. J. Heller and H. R. Blattmann, Pure Appl. Chem. **36,** 141 (1974).

[101] J. Keck, H. E. A. Kramer, H. Port, T. Hirsch, P. Fischer, and G. Rytz, J. Phys. Chem. **100,** 14468 (1996).

[102] W. Al-Soufi, K. H. Grellmann, and B. Nickel, J. Phys. Chem. **95,** 10503 (1991).

[103] H. Eisenberger, B. Nickel, A. A. Ruth, W. Al-Soufi, and K. H. Grellmann, J. Phys. Chem. **95,** 10509 (1991).

[104] K. K. Smith and K. J. Kaufmann, J. Phys. Chem. **82,** 2286 (1978).

[105] P. F. Barbara, P. M. Rentzepis, and L. E. Brus, J. Am. Chem. Soc. **102,** 2786 (1980).

[106] P. F. Barbara, L. E. Brus, and P. M. Rentzepis, J. Am. Chem. Soc. **102,** 5631 (1980).

[107] S. R. Flom and P. F. Barbara, Chem. Phys. Lett. **94,** 488 (1983).

[108] T. Elsaesser, W. Kaiser, and W. Lüttke, J. Phys. Chem. **90,** 2901 (1986).

[109] T. Elsaesser and W. Kaiser, Chem. Phys. Lett. **128,** 231 (1986).

[110] F. Laermer, T. Elsaesser, and W. Kaiser, Chem. Phys. Lett. **148,** 119 (1988).

[111] M. Wiechmann, H. Port, F. Laermer, W. Frey, and T. Elsaesser, Chem. Phys. Lett. **165,** 28 (1990).

[112] B. J. Schwartz, L. A. Peteanu, and C. B. Harris, J. Phys. Chem. **96,** 3591 (1992).

[113] J. L. Herek, S. Petersen, L. Banares, and A. H. Zewail, J. Chem. Phys. **97,** 9046 (1992).

[114] T. Arthen-Engeland, T. Bultmann, N. P. Ernsting, M. A. Rodriguez, and W. Thiel, Chem. Phys. **163,** 43 (1992).

[115] W. Frey, F. Laermer, and T. Elsaesser, J. Phys. Chem. **95,** 10391 (1991).

[116] T. Fiebig, M. Chachisvilis, M. Manger, A. H. Zewail, A. Douhal, I. Garcia-Ochoa, and A. de La Hoz Ayuso, J. Phys. Chem. A **103,** 7419 (1999).

[117] S. Ameer-Beg, S. M. Ormson, R. G. Brown, P. Matousek, M. Towrie, E. T. J. Nibbering, P. Foggi, and F. V. R. Neuwahl, J. Phys. Chem. A **105,** 3709 (2001).

[118] T. Elsaesser, in *Femtosecond Chemistry*, J. Manz and L. Woeste, eds., (Wiley-VCH, Weinheim, Germany, 1995), Vol. 2, p. 563.

[119] C. Chudoba, S. Lutgen, T. Jentzsch, R. E, M. Woerner, and T. Elsaesser, Chem. Phys. Lett. **240,** 35 (1995).

[120] S. Lochbrunner, A. J. Wurzer, and E. Riedle, J. Phys. Chem. **112,** 10699 (2000).

[121] A. J. Wurzer, S. Lochbrunner, and E. Riedle, Appl. Phys. B **B 71,** 405 (2000).

[122] C. Chudoba, E. Riedle, M. Pfeiffer, and T. Elsaesser, Chem. Phys. Lett. **263,** 622 (1996).

[123] M. Pfeiffer, K. Lenz, A. Lau, T. Elsaesser, and T. Steinke, J. Raman Spectrosc. **28,** 61 (1997).

[124] E. Riedle, S. Lochbrunner, A. Wurzer, V. de Waele, and R. de Vivie-Riedle, in *Ultrafast Phenomena XII*, T. Elsaesser, ed., (Springer, Berlin, Germany, 2001), p. 645.

[125] G. Varsanyi, *Vibrational spectra of benzene derivatives* (Academic Press, New York, London, 1969).

[126] M. J. Frisch *et al.*, *Gaussian 98, Revision A.2* (Gaussian, Inc., Pittsburgh PA., 1998).

[127] K. Hafner, H. E. A. Kramer, H. Musso, G. Ploss, and G. Schulz, Chem. Ber. **97,** 2066 (1964).

[128] J. Stenger, D. Madsen, J. Dreyer, E. T. J. Nibbering, P. Hamm, and T. Elsaesser, J. Phys. Chem. A **105,** 2929 (2001).

[129] D. Madsen, J. Stenger, J. Dreyer, E. T. J. Nibbering, P. Hamm, and T. Elsaesser, Chem. Phys. Lett. **341,** 56 (2001).

[130] M. Pfeiffer, K. Lenz, A. Lau, and T. Elsaesser, J. Raman Spectrosc. **26,** 607 (1995).

[131] M. J. Rosker, F. W. Wise, and C. L. Tang, Phys. Rev. Lett. **57,** 321 (1986).

[132] S. Ruhman, A. G. Joly, and K. A. Nelson, J. Chem. Phys. **86,** 6563 (1987).

[133] Y.-X. Yan and K. A. Nelson, J. Chem. Phys. **87,** 6257 (1987).

[134] H. L. Fragnito, J. Y. Bigot, P. C. Becker, and C. V. Shank, Chem. Phys. Lett. **160,** 101 (1989).

[135] W. T. Pollard and R. A. Mathies, Annu. Rev. Phys. Chem. **43,** 497 (1989).

[136] M. H. Vos, F. Rappaport, J. C. Lambry, J. Breton, and J. L. Martin, Nature **363,** 320 (1993).

[137] T. S. Yang, M. S. Chang, R. Chang, M. Hayashi, S. H. Lin, P. Vohringer, W. Dietz, and N. F. Scherer, J. Chem. Phys. **110,** 12070 (1999).

[138] R. M. Bowman, M. Dantus, and A. H. Zewail, Chem. Phys. Lett. **156,** 131 (1989).

[139] R. M. Bowman, M. Dantus, and A. H. Zewail, Chem. Phys. Lett. **96,** 2416 (1992).

[140] Q. Wang, R. W. Schoenlein, L. A. Peteanu, R. A. Mathies, and C. V. Shank, Science **266,** 422 (1994).

[141] T. Kühne and P. Vöhringer, J. Phys. Chem. A **102,** 4177 (1998).

[142] K. Iwata and H. Hamaguchi, J. Phys. Chem. A **101,** 632 (1997).

[143] P. T. Chou, S. L. Studer, and M. L. Martinez, Chem. Phys. Lett. **178,** 393 (1991).

[144] M. A. Rios and M. C. Rios, J. Phys. Chem. A **102,** 1560 (1998).

[145] T. Elsaesser and W. Kaiser, Annu. Rev. Phys. Chem. **42,** 83 (1991).

[146] J. C. Owrutsky, D. Raftery, and R. M. Hochstrasser, Annu. Rev. Phys. Chem. **45,** 519 (1994).

[147] A. Seilmeier and W. Kaiser, in *Ultrashort laser pulses. Generation and applications., Top. Appl. Phys., 60, 2nd edition ed.*, W. Kaiser, ed., (Springer, Berlin, 1993), p. 279.

[148] I. N. Brnsted, Rev. Trav. Chim. **42,** 718 (1923).

[149] I. N. Brnsted, Chem. Rev. **5,** 231 (1928).

[150] C. J. D. von Grotthuss, Ann. Chim. LVIII **1,** 515 (1806).

[151] D. Marx, M. E. Tuckerman, J. Hutter, and M. Parrinello, Nature **397,** 601 (1999).

[152] R. P. Bell, *The proton in chemistry*, 2 ed. (Chapman and Hall, London, 1973).

[153] D. N. Silverman, Biochim. Biophys. Acta - Bioenergetics **1458,** 88 (1999).

[154] W. Kühlbrandt, Nature **406,** 569 (2000), and references therein.

[155] T. Förster, Naturwissenschaften **36,** 186 (1949).

[156] T. Förster, Elektrochem. **54,** 42 (1950).

[157] T. Förster, Pure Appl. Chem. **4,** 43 (1970).

[158] L. M. Tolbert and J. E. Haubrich, J. Am. Chem. Soc. **12,** 863 (1990).

[159] Y. Wei, W. Wang, J. M. Yeh, B. Wang, D. C. Yang, and J. K. Murray, Adv. Mater. **6,** 372 (1994).

[160] E. S. Mansueto and C. A. Wight, J. Am. Chem. Soc. **111,** 1900 (1989).

[161] D. Huppert and E. M. Kosower, Annu. Rev. Phys. Chem. **37,** 1127 (1986).

[162] B. Cohen, D. Huppert, K. M. Solntsev, Y. Tsfadia, E. Nachliel, and M. Gutman, J. Am. Chem. Soc. **124,** 7539 (2002).

[163] P. W. Atkins, *Physical Chemistry* (Oxford University Press, Oxford Melbourne Tokyo, 1990).

[164] W. Bartok, P. J. Lucchesi, and N. S. Snider, J. Am. Chem. Soc. **84,** 1842 (1962).

[165] E. L. Wehry and L. B. Rogers, J. Am. Chem. Soc. **87,** 4234 (1952).

[166] J. F. Ireland and P. A. H. Wyatt, Adv. Phys. Org. Chem. **12,** 131 (1976).

[167] J. T. Hynes, T. H. Tran-Thi, and G. Granucci, J. Photochem. Photobiol. A **154,** 3 (2002).

[168] T. H. Tran-Thi, C. Prayer, P. H. Millié, P. Uznanski, and J. T. Hynes, J. Phys. Chem. A **106,** 2244 (2002).

[169] R. Knochenmuss, I. Fischer, D. Luhus, and Q. Lin, Isr. J. Chem. **39,** 221 (1999).

[170] B. Z. Magnes, N. V. Strashnikova, and E. Pines, Isr. J. Chem. **39,** 361 (1999).

[171] J. R. Platt, J. Chem. Phys. **17,** 484 (1949).

[172] E. Pines and D. Pines, in *Ultrafast Hydrogen Bonding Dynamics and Proton Transfer Processes in the Condensed Phase*, T. Elsaesser and H. J. Bakker, eds., (Kluwer Academic Publishers, Dordrecht, Netherlands, 2002), chapter 7.

[173] T. H. Tran-Thi, T. Gustavsson, C. Prayer, S. Pommeret, and J. T. Hynes, Chem. Phys. Lett. **329,** 421 (2000).

[174] A. Douhal, S. K. Kim, and A. H. Zewail, Nature **378,** 260 (1995).

[175] D. Huppert, A. Jayaramen, R. G. Maines, D. W. Steyert, and P. M. Rentzepis, J. Chem. Phys. **81,** 5596 (1984).

[176] G. W. Robinson, J. Phys. Chem. **95,** 10386 (1991).

[177] J. Lee, G. W. Robinson, and M. P. Basses, J. Am. Chem. Soc. **108,** 7477 (1986).

[178] E. Pines and G. R. Fleming, J. Phys. Chem. **95,** 10448 (1991).

[179] N. Agmon, E. Pines, and D. Huppert, J. Chem. Phys. **7,** 5631 (1988).

[180] D. Huppert, E. Pines, and N. Agmon, J. Opt. Soc. Am. B **7,** 1545 (1990).

[181] L. Genosar, B. Cohen, and D. Huppert, J. Phys. Chem. A **104,** 6689 (2000).

[182] K. M. Solntsev, D. Huppert, and N. Agmon, J. Phys. Chem. A **105,** 5868 (2001).

[183] E. Pines, B. Z. Magnes, M. J. Lang, and G. R. Fleming, Chem. Phys. Lett. **281,** 413 (1997).

[184] M. von Smoluchowski, Ann. Phys. **48,** 1103 (1915).

[185] A. Szabo, J. Phys. Chem. **93,** 6929 (1989).

[186] R. Knochenmuss, K. M. Solntsev, and L. M. Tolbert, J. Phys. Chem. A **105,** 6393 (2001).

[187] E. Pines, D. Huppert, and N. Agmon, J. Chem. Phys. **88,** 9 (1988).

[188] G. Zundel, Adv. Chem. Phys. **111,** 1 (2000).

[189] H. P. Haar, U. K. A. Klein, F. W. Hafner, and M. Hauser, Chem. Phys. Lett. **49,** 563 (1977).

[190] E. Pines and B. Z. Magnes, personal communication.

[191] O. S. Wolfbeis, Fresenius J. Anal. Chem. **320,** 271 (1986).

[192] B. Muller and P. C. Hauser, Analyst **121,** 339 (1996).

[193] O. S. Wolfbeis and H. E. Posch, Anal. Chim. Acta **185,** 321 (1986).

[194] K. Kano and J. H. Fendler, Biochim. Biophys. Acta **509,** 289 (1978).

[195] N. Barrash-Shiftan, B. B. Brauer, and E. Pines, J. Phys. Org. Chem. **11,** 743 (1998).

[196] C. F. Shannon and D. E. Eads, J. Chem. Phys. **103,** 13 (1995).

[197] S. A. Rice, *Comprehensive Chemical Kinetics Vol. 25: Diffusion-Limited Reactions* (Elsevier, Amsterdam, 1985).

[198] M. Eigen, W. Kruse, and L. D. Maeyer, Prog. React. Kinet. **2,** 285 (1964).

[199] M. Eigen, Angew. Chem. Int. Ed. **3,** 1 (1964).

[200] J. L. Skinner and H. P. Trommsdorff, J. Chem. Phys. **89,** 897 (1988).

[201] A. J. Leggett, S. Chakravarty, A. T. Dorsey, M. P. A. Fischer, A. Garg, and W. Zwerger, Rev. Mod. Phys. **59,** 1 (1987).

[202] P. Hänggi, P. Talkner, and M. Borkovec, Rev. Mod. Phys. **62,** 251 (1990).

[203] A. Oppenländer, C. Rambaud, H. P. Trommsdorff, and J. C. Vial, Phys. Rev. Lett. **63,** 1432 (1989).

[204] K. Ando and J. T. Hynes, Adv. Chem. Phys. **110,** 381 (1999).

[205] R. Jimenez, G. R. Fleming, P. V. Kumar, and M. Maroncelli, Nature **369,** 471 (1994).

[206] R. C. Bertelson, in *Photochromism*, G. H. Brown, ed., (Wiley, New York, 1971).

[207] R. Guglielmetti, in *Photochromism: Molecules and Systems; Studies in Organic Chemistry*, H. Duerr and H. Bouas-Laurent, eds., (Elsevier, Amsterdam, 1990), chapter 8 and 23, and references therein.

[208] N. Tamai and H. Miyasaka, Chem. Rev. **100,** 1875 (2000).

[209] *Molecular Switches*, B. L. Feringa, ed., (Wiley-VCH, Weinheim, Germany, 2001).

[210] N. P. Ernsting, Chem. Phys. Lett. **159,** 526 (1989).

[211] N. P. Ernsting and T. Arthen-Engeland, J. Phys. Chem. **95,** 5502 (1991).

[212] N. P. Ernsting, B. Dick, and T. Arthen-Engeland, Pure & Appl. Chem. **62,** 1483 (1990).

[213] J. Z. Zhang, B. J. Schwartz, J. C. King, and C. B. Harris, J. Am. Chem. Soc. **114,** 10921 (1992).

[214] S. A. Krysanov and M. V. Alfimov, Chem. Phys. Lett. **91,** 77 (1982).

[215] Y. Kalisky, T. E. Orlowski, and D. J. Williams, J. Phys. Chem. **87,** 5333 (1983).

[216] S. Aramaki and G. H. Atkinson, J. Am. Chem. Soc. **114,** 438 (1992).

[217] N. W. Tyer and R. S. Becker, J. Am. Chem. Soc. **92,** 1289 (1970).

[218] C. Lenoble and R. S. Becker, J. Phys. Chem. **90,** 62 (1986).

[219] T. Bercovici and E. Fischer, J. Am. Chem. Soc. **86,** 5687 (1964).

[220] T. Bercovici, R. Heiligman-Rim, and E. Fischer, Mol. Photochem. **1,** 23 (1969).

[221] H. Takahasi, K. Yoda, H. Isaka, T. Ohzeki, and Y. Sakaino, Chem. Phys. Lett. **140,** 90 (1987).

[222] S. M. Aldoshin, L. O. Atovmyan, and O. A. Kozina, Bull. Acad. Sc. USSR, Ser. Chem. **36,** 169 (1987).

[223] D. A. Reeves and F. Wilkinson, J. Chem. Soc. Faraday Trans. 2 **69,** 1381 (1973).

[224] A. K. Chibisov and H. Görner, J. Photochem. Photobiol. **105,** 261 (1997).

[225] C. Lenoble and R. S. Becker, J. Phys. Chem. **90,** 62 (1986).

[226] H. Takahashi, H. Murakawa, Y. Sakaino, T. Ohzeki, J. Abe, and O. Yamada, J. Photochem. Photobiol. A: Chemistry **45,** 233 (1988).

[227] A. K. Chibisov and H. Görner, J. Phys. Chem. A **101,** 4305 (1997).

[228] H. Görner, Chem. Phys. Lett. **282,** 381 (1998).

[229] T. Yuzawa, A. Shimojima, and H. Takahashi, J. Mol. Struct. **352/253,** 497 (1995).

[230] Y. Futami, M. L. S. Chin, S. Kudoh, M. Takayanagi, and M. Nakata, Chem. Phys. Lett. **370,** 460 (2003).

[231] H. Eckhardt, A. Bose, and V. A. Krongauz, Polymer **28,** 1959 (1987).

[232] M. V. Alfimov, A. V. Balakin, S. P. Gromov, Y. V. Zaushitsyn, A. Y. Resnyanskii, and A. P. Shkurinov, Russ. J. Phys. Chem. **73,** 1685 (1999).

[233] A. Kholmanskii and K. Dyumaev, Russ. Chem. Rev. **56,** 136 (1987).

[234] M. Zimmer, Chem. Rev. **102,** 759 (2002).

Acknowledgements

The years at the Max-Born-Institute have been an intense and manifold experience, that I cherish and of which I am proud. I feel indebted to many people who contributed to it, both from a scientific and a human point of view.

I would like to thank in the first place Prof. Dr. T. Elsaesser for having given me this precious opportunity, for many decisive scientific contributions, continued support, careful supervision and scientific inspiration.

I owe special thanks to Dr. Erik T. J. Nibbering for having invited me to join his group, for countless discussions and constant encouragement, valuable teaching and the insights into chemistry, protestantism and the Dutch Weltanschauung.

I thank warmly Dr. A. Kummrow for his precious introduction to the femtosecond lab and for his responsible and careful help.

Many thanks to Dr. H. Fidder for the fruitful cooperation in the molecular switches project, his (thought-)provoking comments and an exciting stay in a frozen Uppsala, and to Dr. J. Dreyer for the important theoretical contributions and his support in many occasions.

I wish to thank profoundly Nils Huse for priceless help in critical moments as well as K. Heyne and O. Mohammed. I thank the three of them for friendship, advice, help, discussions, food, music, language lessons, German and Arab enlightenment, comradeship ...

I had the fortune to be involved in a variety of fruitful projects and I wish to thank my coworkers for the pleasant team-work, in particular R. Grunwald, A. K. Holm, Dr. V. Kozic, Dr. M. Krikunova, V. Lehtovuori, Dr H. Lokstein, B. Z. Magnes, Prof. Dr. E. Pines, Dr. B. Voigt, Dr. W. Wernke, T. Zemojtel.

Many thanks go to the staff of the institute for their technical support and for much more than that: Frau R. Goleschny, Frau M. Lehmann, Herrn H.-G. Ludewig, Frau B. Neutenkötter, Herr P. Scholze, Frau B. Steinert, Frau K. Triebler and Herrn H. Walz.

Last but not least, I would like to thank F. Eickemeyer and G. Cassabois, who triggered me to the MBI adventure and offered me the friendliest welcome, as well as J. Bredenbeck, J. Edler, T. Günther, Prof. Dr. P. Hamm, Dr. F. Intonti, Dr. C. Lienau, V. Malyarchuk, K. Müller, Dr. J. Stenger, Dr. S. Wachsmann-Hogiu, Dr. M. Wörner for advice, suggestions, help and friendship.

Zusammenfassung

In dieser Arbeit wird Femtosekunden-Spektroskopie im mittleren Infrarot angewandt auf einige der am gründlichsten studierten fotoinduzierten Reaktionen: der Wasserstoff-/Protonentransfer im elektronischen angeregten Zustand, für einen intramolekularen und einen intermolekularen Fall, sowie die Isomerisation fotochromer Verbindungen.

Elektronische Spektroskopie ist die am häufigsten verwendete Methode zur Untersuchung ultraschneller Reaktionsdynamik in der kondensierten Phase, wobei Übergänge zwischen elektronischen Zuständen der reagierenden molekularen Systeme beobachtet werden. Häufig werden elektronische Übergänge abgetastet, deren Wellenfunktionen delokalisiert sind, so daß kaum ortsspezifische Information erhalten wird. Außerdem ist aufgrund der breiten Absorptionslinien, die aus den schnellen Dephasierungszeiten elektronischer Übergänge resultieren, eine verlässliche Interpretation der experimentellen Daten schwierig; dies umso mehr, je komplexer der Reaktion ist, z.B. durch die Anwesenheit verschiedener Isomere oder durch das Zusammenwirken vieler elektronischer Zustände. Femtosekunden-Infrarotspektroskopie wird in dieser Arbeit als leistungsfähige Alternative eingesetzt, um ultraschnelle Reaktionsdynamik zu beobachten, und so den hohen Grad an Korrelation zwischen Infrarotspektren und molekularer Struktur sowie die Vorteile schmaler Bandbreiten IR-aktiver Schwingungsmoden auszunutzen.

Der größte Teil dieser Arbeit ist einem der Hauptthemen ultraschneller Spektroskopie an wasserstoffverbrückten Systemen gewidmet: dem Prozess des Wasserstoff/Protonentransfers in angeregten Zuständen. Diese elementare Reaktion ist ein interessanter Modellfall zur Untersuchung grundlegender mikroskopischer Reaktionsmechanismen und spielt eine wichtige Rolle bei molekularen Funktionen in einer Vielzahl von Systemen.

Der intermolekulare Wasserstofftransfer im angeregten Zustand (engl. ESIHT) wurde im HBT-Molekül untersucht, in dem der ESIHT in Form einer Enol-Keto-Umlagerung abläuft. Nach UV-Anregung wird die Bildung der Keto-Form von HBT durch Abtasten der Absorptionsbande der Carbonyl-Streckschwingung zeitlich aufgelöst. Die C=O Absorptionszunahme erfolgt auf einer Zeitskala von 30 bis 50 Femtosekunden und beschreibt die Bildung des Keto-Zustands durch Wasserstofftransfer. Zusammen mit der Ausbildung der C=O Streckschwingung liefert das Ausbleichen mehrerer Banden mit C-O Character einen di-

rekten Nachweis der fotoinduzierten Bildung der Keto-Geometrie von HBT. Eine detaillierte Untersuchung des transienten Schwingungsspektrums der Keto-Form im gesamten Bereich des spektralen Fingerabdrucks wird zudem durchgeführt. Die Analyse der beobachteten Bandenformen inklusive der C=O Streckschwingung enthüllt, dass solche Moden im Grundzustand gebildet werden. Damit zeigt sich, daß diese Schwingungen nicht als Kanäle zur Aufnahme der überschüssigen Energie, die in der ESHIT-Reaktion freigegeben wird, dienen. Daraus folgt, dass die Dehnung der C=O Streckmode an der Wasserstofftransfer-Reaktion nicht beteiligt ist. Die überschüssige Energie ist zuerst hauptsächlich in einigen niederfrequenten Raman-aktiven Moden enthalten, die nach dem elektronischen Übergäng angeregt werden. Die Anregung dieser niederfrequenten Raman-aktiven Schwingungen verursachz durch anharmonische Kopplung eine anfängliche Rotverschiebung der IR-aktiven Banden im Bereich des spektralen Fingerabdrucks. Die anschließende Umverteilung der Schwingungsenergie führt zu einer charakteristischen Blauverschiebung der gemessenen Banden auf einer Pikosekunden Zeitskala. Oszillatorische Signalmodulationen in der Dynamik der C=O Streckschwingung wurden als Konsequenz kohärenter Wellenpacketbewegung entlang anharmonisch gekoppelter niederfrequenter Moden gedeutet.

Eine Untersuchung der (bimolekularen) Säure-Base-Neutralisierungsreaktion in Wasser, die einen intermolekularen Protontransfer beinhaltet, ist der zweite untersuchte Modellfall. Die Reaktion wird initiiert durch Auslösen einer Veränderung der Azidität in einer Fotosäure aufgrund elektronischer Anregung, die zu einer Erhöhung der Aziditätskonstanten um sieben Größenordnungen führt. Die Reaktionsdynamik kann durch Beobachtung der IR-aktiven charakteristischen Schwingungsmoden der Fotosäure, ihres konjugierten Anions und der protonierten Base, die bei der Reaktion entsteht, verfolgt werden. Die Daten zeigen deutlich zwei Aspekte. Bei hoher Basenkonzentration kann man den Protonentransfer entlang einer bereits existierenden Wasserstoffbrücke in “enggebundenen" Säure-Base-Komplexen beobachten. In diesem Fall läuft ein extrem schneller Protonentransfer ab, der nicht diffusionskontrolliert ist und auf einer Zeitskala stattfindet, die mit einer experimentellen Zeitauflösung von 150 fs nicht mehr aufgelöst werden kann. Im Gegensatz dazu bildet die anfänglich unkomplexierte Säure bei niedriger Basenkonzentration nach diffusiver Bewegung “schwachgebundene" Komplexe, so daß die Reaktion auf viel längerer Zeitskala stattfindet. Um diese Ergebnisse in Einklang zu bringen, wird das klassische Eigen-Weller-Modell der Säure-Base-Reaktionen verfeinert. Das Modell beinhaltet traditionell (i) diffusive Bewegung der Säure und Base, (ii) “on-contact"-Reaktionsdynamik, wobei ein Proton von der Säure zur Base transferiert wird und (iii) diffusive Trennung des Ionenpaares. Das verfeinerte Reaktionsschema liefert eine detailliertere Beschreibung des “on-contact"-Reaktionsschrittes in Form eines Drei-Stufen-Modells: im ersten Teilschritt wird ein “schwachgebundenes" Säure-Base-Paar durch Diffusion gebildet. Es folgt eine Umordnung zu einem “enggebundenen" Reaktionspaar, bevor der Protonentransfer in einem dritten Teilschritt statt-

finden kann. Die Beobachtung des ultraschnellen bimolekularen Protonentransfers (eine Größenordnung schneller als zuvor angenommen) in einem System, in dem unter Umgebungsbedingungen die Reaktanden (oder ein signifikanter Anteil dieser) sich nicht durch Diffusion begegnen müssen, ist in sich selbst fundamental wichtig.

Die Untersuchung einer anderen Klasse fotoinduzierter Reaktionen stellt den letzten Teil dieser Arbeit dar: die Ringöffnungsreaktion fotochromer Spiropyrane. Fotochrome Verbindungen ändern ihre Farbe nach Absorption von Licht spezifischer Wellenlänge als Konsequenz der fotoinduzierten reversiblen Transformation zwischen zwei isomeren Formen, die sich in zahlreichen Eigenschaften unterscheiden, die Absorptionsspektren eingeschlossen. Solch eine Eigenschaft ist von potentiellem Interesse für einen breiten Bereich von Anwendungen von optischer Datenspeicherung und Displays bis hin zu optisch kontrollierten molekularen Schaltern. Zwei Molekülsysteme wurden untersucht: BIPS und 6n-BIPS. Durch Beobachtung der Spektren der reagierenden Moleküle im mittleren Infrarotbereich wurden die relevanten Zeitskalen der Entstehung der Reaktionsprodukte eindeutig bestimmt und die Rolle der unterschiedlichen Merocyanin- Isomere in der Reaktion aufgeklärt. Diese Untersuchungen haben wertvolle Einsichten in die Reaktionswege geliefert, die zeigen, dass ein wichtiger Zerfallskanal des angeregten Zustandes von Spiropyran die interne Konversion zum Grundzustand ist mit einer Quanteneffizienz von 90% oder mehr bei BIPS, 63% und 34% (abhängig vom Lösungsmittel) bei 6n-BIPS ist. Interne Konversion ist deshalb ein wichtiger Zerfallskanal, der durchaus der Schlüsselfaktor zur Bestimmung der gesamten fotochemischen Quanteneffizienz für diese Molekülklasse sein könnte. Hinsichtlich potentieller Anwendungen fotochromer Systeme, die sich natürlich in erster Linie durch eine hohe Reaktionsausbeute auszeichnen sollten, muss dieser Aspekt unbedingt berücksichtigt werden.

Zusammenfassend zeigen diese experimentellen Untersuchungen das Potential ultraschneller Infrarotspektroskopie als ein Werkzeug zur Erforschung molekularer Schwingungs- und Reaktionsdynamik. Die Ergebnisse zu bimolekularen Säure-Base Neutralisierungsreaktionen legen eine allgemeine Anwendung dieser Methode zur Untersuchung von Reaktionen, die durch Diffusions- oder Transportphänomene dominiert werden, als auch von Reaktionen, in denen die Reaktanden schon in Kontakt miteinander sind, nahe. Als natürliche Folgearbeit zu der bisherigen über intra- und intermolekularen Wasserstoff/Protonentransfer, kann man den Einsatz von UV-Pump-IR-Abtastspektroskopie zur Erforschung komplizierterer molekularer Systeme wie z.B. des grün fluoreszierenden Proteins (GFP), ein wichtiger biologischer Marker, in dem ein Protonentransferprozess als erster Schritt photoinduzierter Isomerisation vermutet wird, vorhersehen. Schließlich motivieren die Untersuchungen zu Ringö ffnungsreaktionen von Spiropyranen zukünftige Experimente und theoretische Anstrengungen, um die Rolle der internen Konversion in der Fotochemie fotochromer Verbindungen besser zu verstehen.